Synthesis, characterization, and laser refrigeration of rare-earth doped fluoride nanostructures

Xuezhe Zhou

A dissertation
submitted in partial fulfillment of the
requirements for the degree of

Doctor of Philosophy

University of Washington

2017

Reading Committee:

Dr. Peter J. Pauzauskie, Chair

Dr. James J. De Yoreo

Dr. Xiaodong Xu

Program Authorized to Offer Degree:
Materials Science and Engineering

University of Washington

Abstract

Synthesis, characterization, and laser refrigeration of rare-earth doped fluoride nanostructures

Xuezhe Zhou

Chair of the Supervisory Committee:
Professor Dr. Peter J. Pauzauskie
Department of Materials Science and Engineering

Rare-earth (RE) doped materials with unique 4f electronic structures show special optical phenomena at the macro- and microscale, which are commonly studied through laser-mediated experiments. Recently, RE doped nanocrystals have been intensively studied for various applications, including bioimaging, biolabeling, photodynamic therapy, catalysis, solar cells, color displays, light emitting diodes, low-threshold lasers, high temperature sensors, and many others. For the last five years in the Pauzauskie lab, I have been focusing on developing new methods for synthesizing and characterizing engineered micro- and nano-scale RE-doped nanocrystals for investigating the interaction of light with condensed matter, especially laser cooling through anti-Stokes fluorescence. The main method utilized for laser cooling in the Pauzauskie lab is optical trapping with laser tweezers. A brief introduction to laser cooling and optical trapping is included in Chapter 1 of this thesis. The remaining chapters describe the development and characterization of different phases of RE doped nanocrystals which can be optically trapped for nanoscale laser cooling and thermometry with laser tweezers.

In Chapter 2, different methods of synthesizing fluoride nanocrystals are intro-

duced and compared based on the requirements for the nanocrystals. A low-cost, scalable, and environmentally friendly hydrothermal method has been specifically introduced for fabricating both $LiYF_4$ (YLF) and $NaYF_4$ nanostructures. Due to the hermetic conditions inherent to hydrothermal synthesis, the growth mechanism of RE doped fluoride nanocrystals is unclear. Chapter 3 presents a systematic study on the synthetic mechanism of hydrothermal synthesis of sodium yttrium fluoride nanocrystals. Various cutting edge techniques, including 'in-situ' TEM, EDS, XANES, EXAFS, and APT, are used to investigate the fundamental properties and growth mechanisms of RE doped fluoride nanocrystals in both Chapter 2 and 3.

Chapter 4 describes the first experimental demonstration of laser cooling of Yb^{3+} doped YLF nanocrystals in aqueous media, which is explained by anti-Stokes fluorescence. The Yb^{3+} ions inside the crystal absorb laser photons and emit a mean higher energy fluorescence to extract heat from the crystal lattice. This unprecedented laser cooling in a condensed phase is achieved through home-built laser tweezers with a temperature extraction technique based on cold Brownian motion analysis. Furthermore, crystals of $NaYF_4$, predicted to be a good host structure for laser cooling, are also experimentally proven for laser cooling in aqueous medium for the first time. The ability to optically generate local refrigeration fields around individual nanocrystals promises to enable precise optical temperature control within integrated electronic/photonic/microfluidic circuits, as well as thermal modulation of basic biomolecular processes.

In Chapter 5, nanoscale thermometry of RE doped fluoride nanocrystals using spectroscopy methods has been applied on both single nanocrystals and ensembles of nanocrystals. The radiative relaxation rate of a single nanocrystal is studied with varying the local density of states of emitting dipoles through tuning the distance between the optically trapped nanocrystal and a nearby dielectric substrate. Lifetime thermometry is developed through a low-cost and compact avalanche photodiode with live data extraction and processing in LabVIEW, which can accurately and quickly probe the local temperature. In addition, optical trapping of individual nanocrystals with laser tweezers can provide precise temperature sensing at different locations in the nanoscale.

Chapter 6 presents a summary of the thesis, along with a short discussion of future research directions for laser cooling of nanocrystals.

TABLE OF CONTENTS

Page

LIST OF FIGURES

Figure Number Page

GLOSSARY

UCNP: upconversion nanoparticle

PL: photoluminescence

AFM: atomic force microscope

APT: atom-probe tomography

BF: bright field

CBM: cold Brownian motion

DDA: discrete dipole approximation

DI: deionized

EDX: energy-dispersive x-ray spectroscopy

EXAFS: extended X-ray absorption fine structure

FDTD: finite-difference time-domain

FTIR: Fourier transform infrared

HAADF: high-angle annular dark field

MDR: morphology-dependent resonance

MEEP: MIT electromagnetic equation propagation

NA: numerical aperture

NC: nanocrystal

NIR: near infrared

NW: nanowire

PL: photoluminescence

PSD: power spectral density

PT: photothermal

QPD: quadrant photodiode

SAED: select-area electron diffraction

SEM: scanning electron microscope

XAS: X-ray absorption spectroscopy

XANES: X-ray absorption near edge structure

YLF: yttrium lithium fluoride

Some passages have been quoted verbatim from the following sources:

1. Zhou, X., Roder, P.B., Smith, B.E., Pauzauskie, P.J., Laser Refrigeration of Ytterbium Doped Sodium Yttrium Fluoride Nanowires. (2016), *Adv. Mater.*, 28 (39), 8658–8662.

2. Roder, P.B.*, Smith, B.E.*, Zhou, X.*, Crane, M.J., Pauzauskie, P.J., Laser refrigeration of optically-trapped hydrothermal nanocrystals in physiological media. (2015), *Proc. Natl. Acad. Sci.*, 112 (49), 15024–15029. *. Authors contribute equally.

ACKNOWLEDGMENTS

During the past five years, I have been learning and conducting research at the University of Washington, where I am proud of being one of the Huskies. All the work and achievement that I have accomplished are under the support by my advisor, my labmates, my friends, and my family. I would like to thank everyone for their support.

First of all, I would like to express my special appreciation to my advisor, Professor Peter J. Pauzauskie, who is a tremendous mentor for me. His insights, immense knowledge, passion in science, and patience have been guiding, instructing, and encouraging me on the journey of scientific research over the last five years. He is not only a mentor to me, but also a sincere friend who cares about my life outside of the research and lab. His persistent in science, enthusiasm in teaching remains my best role model for a scientist and teacher, which inspires me to pursue my future career in academic field.

I would also like to thank Professor James De Yoreo, who is an incredible collaborator with the Pauzauskie lab. I am appreciative to his guidance and feedback during our routine meeting. His wisdom and knowledge in crystal growth has contributed immeasurably to the results and understand of the research presented in this thesis. Likewise, I would also like to thank my thesis committee: Professor Xiaodong Xu and Professor Lih Y.Lin for their insightful comments, encouragement, and hard questions, which incentivized me to widen my research from various perspectives.

The Pauzauskie Lab has attracted many creative and bright people with different cultural and academic backgrounds. Thanks to this, I can always gain knowledge,

search for help, and get inspirations from my fellows. Here, I would like to thank Dr. Paden Roder, Dr. Bennett Smith, Matthew Lim, Matthew Crane, Sandeep Manandhar, Anupum Pant, Xiaojing Xia, Abbie Ganas, Stuart Frazier, Automm Lombardo for their help and suggestions. I would also like to thank all the undergraduates and master students that who were once under my mentoring. They contributed a lot to the lab as well.

I want to deeply thank my family and friends. My parents are my teachers for life. I learn from them to embrace the world, to enjoy the life, to behave politely, honestly, confidently, and most importantly to be myself. I am very appreciated their understanding that I am not able to celebrate the Lunar New year and other festivals with them in the last several years. My friends, as well, give me their spiritual support throughout my life. Thank them all! Finally I would like to express my appreciation to my best friend, soul-mate, and beloved Xinyi. Her smiling face and encouraging words are the strongest supports for me to overcome any difficulties. I feel so lucky that we are graduating together in the best season of Seattle. Best wishes for our future and incoming adventure!

DEDICATION

to my dear family, wo-ai-ni-men

Chapter 1

INTRODUCTION

1.1 Motivation

For the last five years in Pauzauskie lab, I have been focusing on developing new and novel methods for synthesizing and characterizing engineered micro- and nano-scale crystals for investigating the interaction of light with condensed matter, especially laser cooling through anti-Stoke fluorescence. Since the first demonstration of laser cooling of solid state materials in 1995,[1] scientists and engineers have devoted a great effort to achieve a sub 100 K cryogenic temperature in vacuum.[2] However, to this day, no one has achieved laser cooling in the condensed phase, due to the challenges in materials synthesis and optical instrument design. With our group's specialties in materials synthesis and characterization, optical manipulation, spectroscopy, data processing and analyzing, we have, for the first time, successfully laser refrigerated Yb-doped-fluoride nanostructures in condensed phases.[3] The ability to optically generate local refrigeration fields around individual nanocrystals promises to enable precise optical temperature control within integrated electronic/photonic/microfluidic circuits, and also thermal modulation of basic biomolecular processes.

To achieve laser cooling of a single nanocrystal, there are several challenging difficulties that need to be solved, which are parts of my thesis work: 1) Fabrication and characterization of high quality crystalline materials to achieve high quantum cooling efficiency and low background absorption; 2) Optimization of material's structure and dopant concentration; 3) Isolation of single nanocrystal from substrate to prevent heat generation and conduction; 4) High irradiance of excitation source to compensate the low absorption coefficient of Yb^{3+} ions in nanocrystal; 5) Precise temperature control and measurement of single nanocrystal; 6) Simulation prediction of single nanocrystal under certain excitation source to help understand and improve laser cooling performance.

Overall, having capability to solve each of the problems can help inform ongoing experiments not only in the laser cooling community, but also the materials science community, as well as creating new possibilities for many other future research directions and applications. In this thesis, I will detail the experimental methods and techniques for achieving laser cooling of single nanostructures in the condensed phase.

1.2 Fundamentals of Laser cooling

1.2.1 History of laser cooling of solid state materials

In 1929, Pringsheim suggested that vaporized sodium atoms could cool through anti-Stokes emission at certain optical excitation wavelengths, which is a system that absorbs a certain wavelength photon and then emits a mean shorter wavelength photon.[4] The energy difference between the absorption and emission photon will extract heat from the material, which will cause the net cooling of the system. This process was proved to be consistent with the second law of thermodynamics by Landau in 1946.[5] The entropy of the the radiation supports this process, in which the system absorbs low entropy photons, such as laser beam, and emits fluorescence photons with high entropy. In 1950, Kastler proposed that rare earth (RE) ions in transparent crystals and atoms in the gas phase can be cooled through anti-Stokes fluorescence due to their high quantum efficiencies and narrow spectra lines.[6] During the anti-Stokes fluorescence cooling, only a small amount of energy difference, few orders of kT, is between the absorbed photon and emitted photon. So a narrow spectra line light source is needed to achieve net cooling of the system with anti-Stokes fluores-

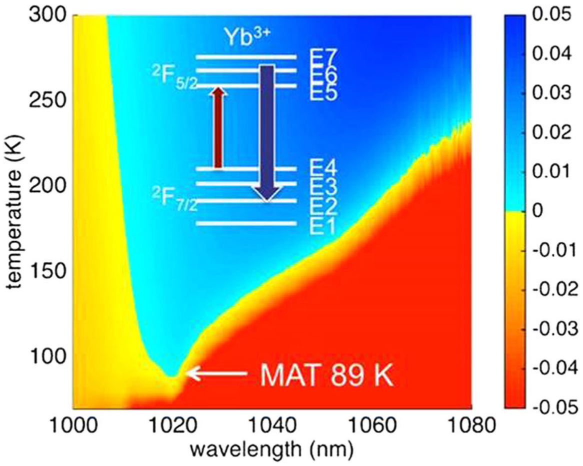

Figure 1.1: Cooling efficiency contour map $\eta_c(\lambda, T)$ evaluated for the latest high purity YLF:10% Yb^{3+} crystal. Blue regions denote cooling, and red regions denote heating. The minimum achievable temperature (MAT) of 89 K is highlighted. (Inset) Illustration of the Yb^{3+} ion energy level diagram (not to scale) with example absorption (red) and anti-Stokes emission (blue) arrows. Figure reproduced with permission from [2]

cence. This process was not able to be tested until the invention of laser in 1960 for the first time.[6] In 1963, Kushida and Geusic first time experimentally cooled a solid with laser light. They used 1064 nm laser to excite a Nd^{3+} doped Y3Al5O12(YAG) crystal and it emitted anti-Stokes fluorescence at 946 nm, which showed less heating due to the laser cooling effect.[7] The net cooling of laser refrigeration through anti-Stokes fluorescence was not achieved until 1995. Epstein and his group members, were able to experimentally demonstrate a 0.3 K net cooling for the first time with a ZBLAN:Yb^{3+} excited by NIR laser, which showed 2% net cooling efficiency under 1030 nm laser beam at room temperature.[1] In 2015, Sheik-Bahaes group showed that Yb^{3+}:YLF bulk crystal can be cooled to 89 K with tuning the excitation of the crystal to Yb^{3+} E4-E5 resonance at 1020 nm, which is shown in Fig.1.1[2]

1.2.2 Laser cooling mechanism

Laser cooling of solid state materials, usually RE ions doped crystals, is accomplished by anti-Stokes fluorescence. RE ions inside the crystal can absorb excitation photons and emit a mean higher energy photon with high entropy, as shown in Fig.1.1, therefore each laser cooling cycle can extract thermal energy and cool the materials.[8] The cooling efficiency for each absorbed photon is

$$\eta_{\mathrm{c}} = \frac{hv_{\mathrm{f}} - hv}{hv} = \frac{\lambda}{\lambda_{\mathrm{f}}} - 1, \tag{1.1}$$

where hv is excitation photon energy, hv_{f} is the mean fluorescence photon energy, λ is the excitation laser wavelength, λ_{f} is the mean fluorescence wavelength. This is ideal case for laser cooling. However, in the real world, only a certain fraction of laser power will be absorbed by the crystal with some amount of parasitic heating due to the existence of impurities inside of the crystal. Considering the background impurity absorption, the absorption efficiency is

$$\eta_{\mathrm{abs}} = \frac{\alpha_{\mathrm{r}}}{\alpha_{\mathrm{r}} + \alpha_{\mathrm{b}}} \tag{1.2}$$

where the α_{r} is the cooling ions resonant absorption and α_{b} is the background impurity absorption.[8] For the absorbed photon energy of cooling ions, there is a fraction of energy that emits radiatively, which is known as quantum efficiency,

$$\eta_{\mathrm{e}} = \frac{W_{\mathrm{rad}}}{W_{\mathrm{rad}} + W_{\mathrm{nr}}} \tag{1.3}$$

Where the W_{rad} is the radiative relaxation of the excited cooling ions and W_{nr} is the nonradiative relaxation of the cooling ions which causes heat generation. For the radiatively emitted photons, there is a chance for them to be trapped and re-absorbed by the crystal, which lower the cooling efficiency. The escaping efficiency η_{esc} can be included in the spontaneous emission as an external quantum efficiency,[8]

$$\eta_{\text{ext}} = \frac{\eta_{\text{esc}} W_{\text{rad}}}{\eta_{\text{esc}} W_{\text{rad}} + W_{\text{nr}}} \tag{1.4}$$

The combination of all the factors described above defines the laser cooing efficiency as:

$$\eta_{\text{c}} = \eta_{\text{ext}} \eta_{\text{abs}} \frac{\lambda}{\lambda_{\text{f}}} - 1 \tag{1.5}$$

The equation above describes overall laser cooling efficiency of converting absorbed photons to escaped fluorescence photons.

1.2.3 Laser cooling materials

RE ions doped fluoride crystals are the best materials for laser cooling, which is mainly due to the unique 4f transitions of RE ions and low-phonon energy of fluoride crystals. As the best laser cooling RE ion, Yb^{3+} ion has a unique electron configuration, especially 4f shell. There is one electron missing from closed 4f shell of Yb^{3+}, which is equivalent as closed 4f shell with one 4f hole. For a single 4f hole, the spin is s = 1/2, angular momentum l = 3. The total spin is S = 1/2 and total orbital angular momentum L = 3. Due to spin-orbit interaction, the ^2F manifold is split into $^2\text{F}_{7/2}$ and $^2\text{F}_{5/2}$ multiplet. The magnitude of the splitting can be calculated as given equation,

$$E_{\text{LS}} = \zeta(l + \frac{1}{2}) \tag{1.6}$$

where ζ is the spin-orbit coupling parameter for Yb^{3+} free ion ζ = 2918 cm^{-1}. Therefor the magnitude of splitting of Yb^{3+} free ion is E_{LS} = 10,200 cm^{-1}, which gives the laser cooling transition of Yb^{3+} around 1μm wavelength.

Since the Yb^{3+} ions are incorporated in crystal, non-spherically symmetric crystal field can partially or completely lift the (2J+1)-fold J_z degeneracy to split each $^{2S+1}L_J$ multiplet. For a high symmetry cubic structure, the $^2F_{7/2}$ and $^2F_{5/2}$ multiplet is split into 3 and 2 levels, respectively. For other low symmetry structures, the $^2F_{7/2}$ and $^2F_{5/2}$ multiplets split into 4 and 3 levels, respectively. Different crystals have different crystal field splittings, which is shown in Fig.1.2a. The crystal field splitting of $^2F_{7/2}$ level can be calculated to obtain the laser cooling efficiency as a function of temperature, as shown in Fig.1.2b. With temperature decreasing to cryogenic temperature range, there is a significant increase of the laser cooling efficiency for small crystal field splitting of $^2F_{7/2}$ level, which is due to the thermal population increase of the pumped transition.

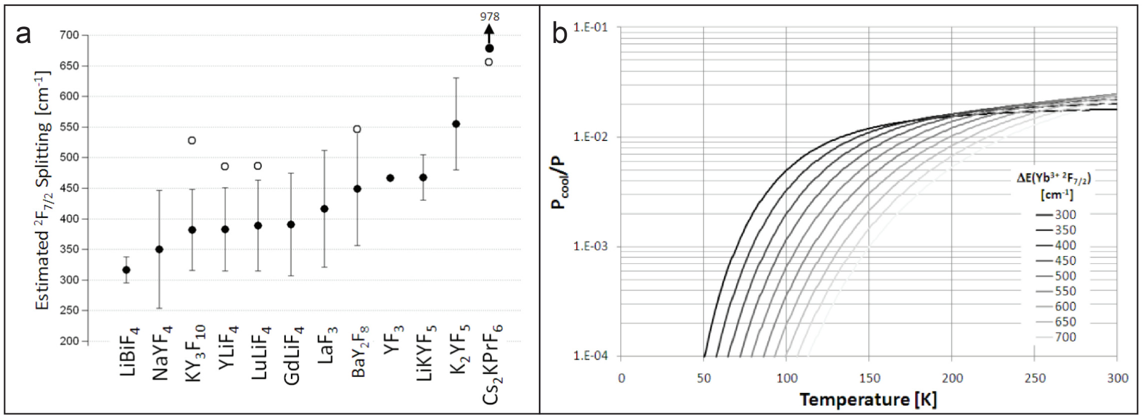

Figure 1.2: (a)Average total crystal-field splitting of the $^2F_{7/2}$ multiplet of Yb^{3+} in fluoride crystals. (b)Calculated cooling efficiency as a function of temperature for different total crystal-field splittings of the $^2F_{7/2}$ ground-state multiplet of Yb^{3+}. Figure reproduced with permission from [9]

So far, laser cooling experiments have been achieved with KY_3F_{10} and $LiYF_4$ crystals, which have the smallest calculated crystal field splitting of $^2F_{7/2}$.[9] Due to the synthesis challenges, bulk $LiBiF_4$ and $NaYF_4$ crystals have not been achieved with the traditional Czochralski synthesis method. In this thesis, a low-cost, scalable hydrothermal synthesis will be introduced for synthesizing $NaYF_4$ nanocrystals. In addition, I have demonstrated that a continuous-wave, single-beam NIR laser-trap can be used to cool -NaYF4: 10%Yb^{3+} NWs in heavy water by 9 ^{o}C below ambient conditions through anti-Stokes emission from the active Yb^{3+} dopant ions within the host crystals lattice.[10]

1.3 *Fundamentals of optical trapping*

1.3.1 History of optical trapping

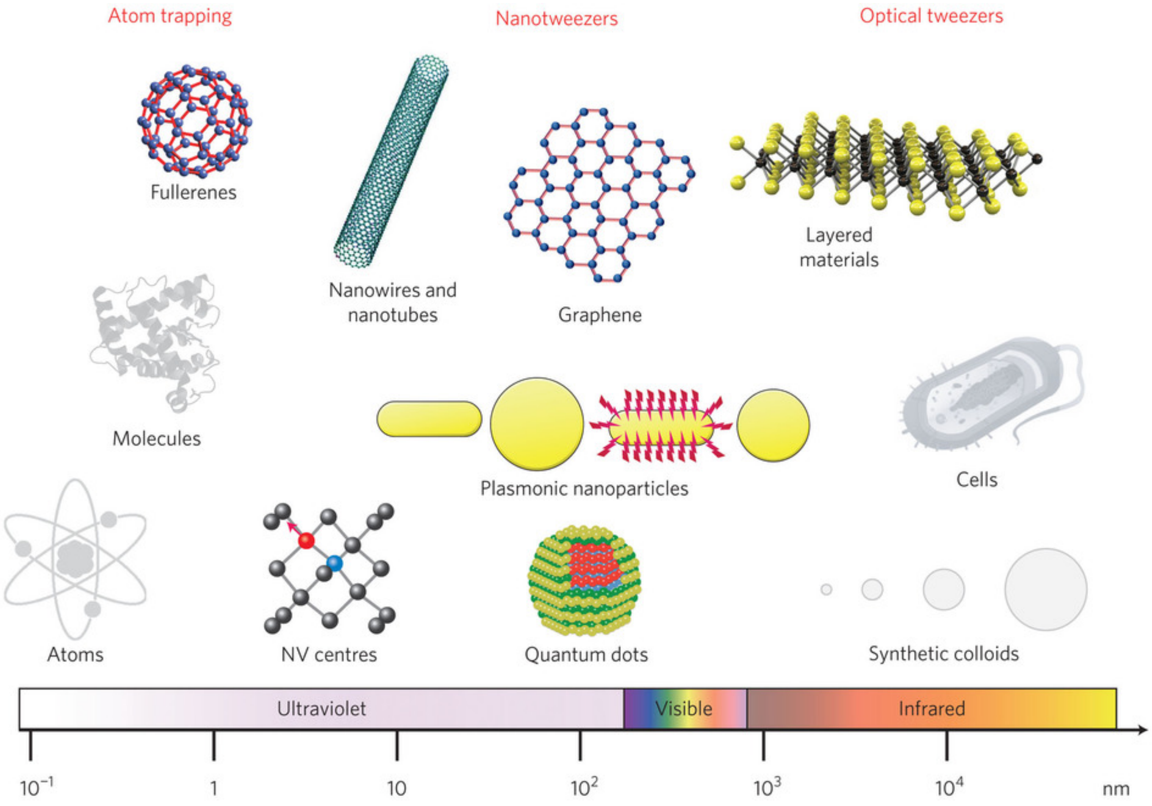

Figure 1.3: Objects of different sizes can be trapped within three main regimes (from left to right): atom trapping (a few angstroms to a few nanometers), nanotweezers (a few nanometers to a few hundred nanometers) and optical tweezers (from a fraction of a micrometre up). The horizontal scale bar shows the average object size and the corresponding light wavelength. NV, nitrogen vacancy. Figure reproduced with permission from [11]

The radiation pressure was first time predicted by James Clerk Maxwell in 1873, which he stated that 'in a medium in which waves are propagated there is a pressure in the direction normal to the waves, and numerically equal to the energy in unit of volume'.[12] After 70 years passed, a 22 years old undergraduate student Arthur Ashkin from Columbia University became interested in the radiation pressure when he was working with a high power magnetron for the US Army during World War II [13]. He detected the pulses from magnetron through observing deflections from an old electromagnetic telephone earpiece, which he interpreted the phenomena as radiation pressure on the metallic receiver. However, he didn't keep pursuing his interest in radiation pressure until late 1960s. At the Bell lab, he used a focused laser to trap polystyrene microbeads, for the first time; this experiment leads to three different areas based on the size range of the trapping materials, including laser trapping of atoms, laser trapping nanomaterials, and laser trapping microscale materials, which is shown in Fig.1.3

Laser trapping atoms directly leads to the Nobel prize in Physics in 1997, which was won by Ashkin's coworker Steven Chu for laser cooling of atoms. The laser cooling of atoms, also called Doppler cooling, created ultracold atoms for quantum physics experiments, which are usually performed near absolute zero temperature. The laser cooling has been applied to improve atomic clocks accuracy, observation of new state of matter, especially the Bose-Einstein Condensate. Laser trapping of nanoscale and microscale materials is mostly conducted with optical tweezers. For laser trapping of microscale materials, optical tweezers have been succesfully applied in biological studies, such as cell sortation, cell mobility study, cell assembly, force spectroscopy of biological motors, biopolymers, etc. Recently, laser trapping of nanoscale materials has draw lots of attentions due to the various objects for trapping, such as quantum dots, carbon nanotubes, 2D nanosheets, nanodiamond, plasmonic nanocrystals, nanowires, semiconductor nnanocrsytals, and others. The femtonewton resolution of force measurement integrated with different spectroscopic techniques with precisely controlled manipulation of optically levitated nanoparticles has promoted a wide range of nanomaterials studies in physics, chemistry, materials sciences, and others.

1.3.2 Optical trapping mechanism

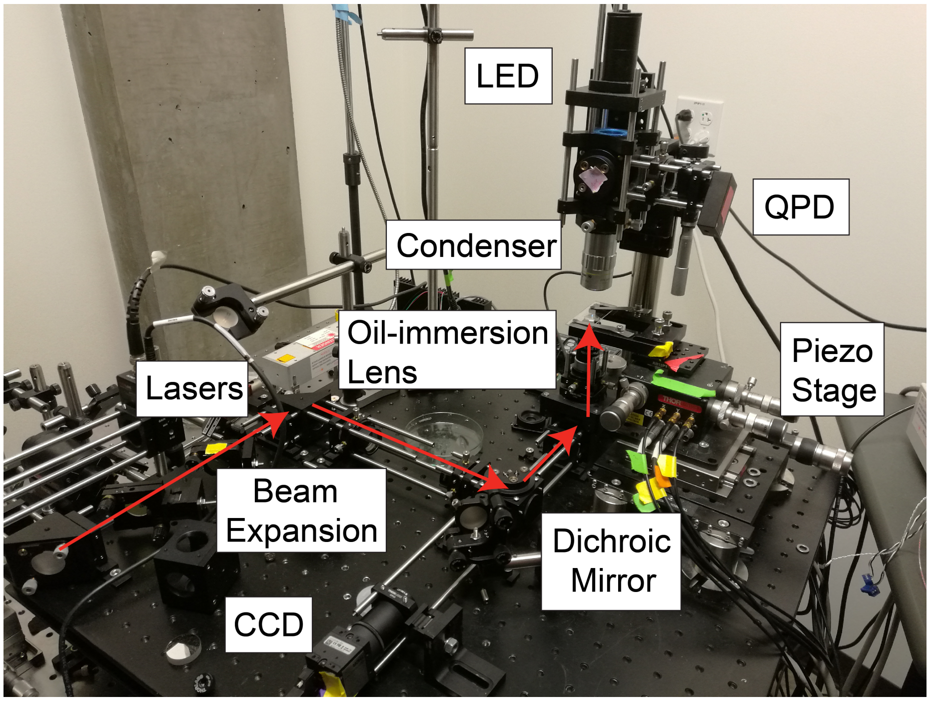

Figure 1.4: Pauzauskie group home-built optical trapping setup.

The home-built optical trapping setup is shown in Fig.1.4, which can be used to explain for a general optical trapping setup. A laser beam, as shown red arrow in Fig.1.4, is expanded and collimated to the size of objective back aperture, which is usually a high numerical aperture (NA) objective lens, including oil and water immersion lenses. Then the laser beam is focused down to a diffraction limit spot size,

$$d = \frac{\lambda}{2n sin\theta} = \frac{\lambda}{2NA} \tag{1.7}$$

where λ is the laser wavelength. The diffraction spot is also the beam waist of the focused laser beam, which has a strong electric field gradient. The nanoparticles can be attracted to the center of the beam waist due to momentum transfer from incident photons to the trapped particles, which particle can gain momentum from the absorbed or scattered incident photons. This scattering force results in trapping the particle in the center of the beam waist.

For trapping nano- and micro-scale particles, a live observation of the trapped particle is beneficial, which can help identify the morphology and number of trapped particles as well as prevent collision from other nearby particles. Depending on the laser tweezers setup, either dark field or bright field imaging system can be installed. For the illumination source in our group, we put a white light LED above the trapping stage, which is focused by an air objective lens (also called condenser). Then white light can pass through the condenser lens and focus at the trapping region. Then the light is collected by the trapping lens and imaged on the CCD camera. A dichroic mirror is placed between the trapping objective lens and CCD, which can reflect trapping laser beam and pass imaging light source at the same time. Based on different research goals, various modifications can be added to the laser tweezers, such as cryo/vacuum trapping, Raman spectroscopy, photoluminescence spectroscopy, lifetime, trapping force measurement, Brownian motion measurement, coaligning different laser sources, confocal imaging, galvo-mirror or spatical light modulator for multiple spots trapping, etc. Our group mostly focuses on Brownian motion and spectroscopy measurement of individual trapped nanoparticles.

Chapter 2

SYNTHESIS AND CHARACTERIZATION OF UPCONVERSION FLUORIDE NANOCRYSTALS

2.1 Introduction

Rare earth doped fluoride nanocrystals have been developed for various applications in the field of bioimaging, biolabeling, photodynamic therapy, catalysis, solar cell, color display, light emitting diodes, low-threshold lasers, high temperature sensors, and many others. The unique 4f-electron transitions of RE ions enable their optical properties, which are significantly affected by the size, shape, and structure of the fluoride host materials. There are many methods used to synthesize fluoride nanocrystals and each has its own advantages and disadvantages. Different methods can be applied based on the essential needs for the nanocrystals, including size, size distribution, morphology, phase, dispersibility in polar/nonpolar solvent, absence of oxygen, hydroxide, or carbon traces, and so on. Several synthesis methods have been introduced as followed. Thermal decomposition synthesis of nanocrystals with thermolysis of fluoride precursors, usually metal trifluoroacetates, requires an oxygen-free environment and high temperature. This method can obtain ultra fine and narrow size distribution nanocrystals. Co-precipitation methods for synthesizing nanocrystals from aqueous solutions are inexpensive, easy to scale up, and environment friendly with using water as exchange reaction medium. However, the hydroxide can precipitate with fluoride nanocrystals, which may affect optical their optical properties. Reversed micelle and microemulsion precipitation method can achieve a wide size range of nanocrystals with low oxygen and hydroxide contamination, which requires an additional high temperature calcination process. Sol-gel methods usually involve preparing a precursor solution to form sol, which is then converted to gel. With sub-sequential aging, and thermal treatment, the fluoride nanocrystals can be obtained. However, this method can not maintain monodispersity of nanocrystals and may also result in carbon contamination. Hydrothermal synthesis uses the high solubility of inorganic compounds in water to crystallize fluoride nanocrystals with elevated temperature and pressure in a sealed autoclave. Hydrothermal synthesis of fluoride nanocrystals have unique advantages compared with other synthetic routes, including tunable size, morphology, structure, and phases of the nanocrystals through hydrothermal conditions. The synthesis usually occurs at relatively low temperatures (usually less than 250 ^{o}C) and provides high purity nanocrystals due to recrystallization processes. The synthesis requires simple equipment and is easy to scale up for industrial application due to low-costs. Our previous study has reported hydrothermal synthesis of $LiYF_4$ nanocrystals. Recently, we have also fabricated $NaYF_4$ nanocrystals with hydrothermal synthesis. The following sections focus on synthesis and characterization of $LiYF_4$ and $NaYF_4$ nanocrystals. Various techniques, including SEM, TEM, EDS, XANES, EXAFS, APT, and others have been used to investigate fundamental properties of these structures.

2.2 $LiYF_4$ synthesis and characterization

The synthesis of $LiYF_4$ nanocrystals was performed with following minor modifications to Ref [14]Yttrium oxide (Y_2O_3), ytterbium oxide (Yb_2O_3) and erbium oxide (Er_2O_3) of 99.99% and all other reagents were purchased from Sigma-Aldrich. Yttrium nitrate ($Y(NO_3)_3$), ytterbium nitrate ($Yb(NO_3)_3$) and erbium nitrate ($Er(NO_3)_3$) were obtained by dissolving the rare earth oxide in nitric acid at approximately 60 ^{o}C with stirring for several hours until excess nitric acid was removed.

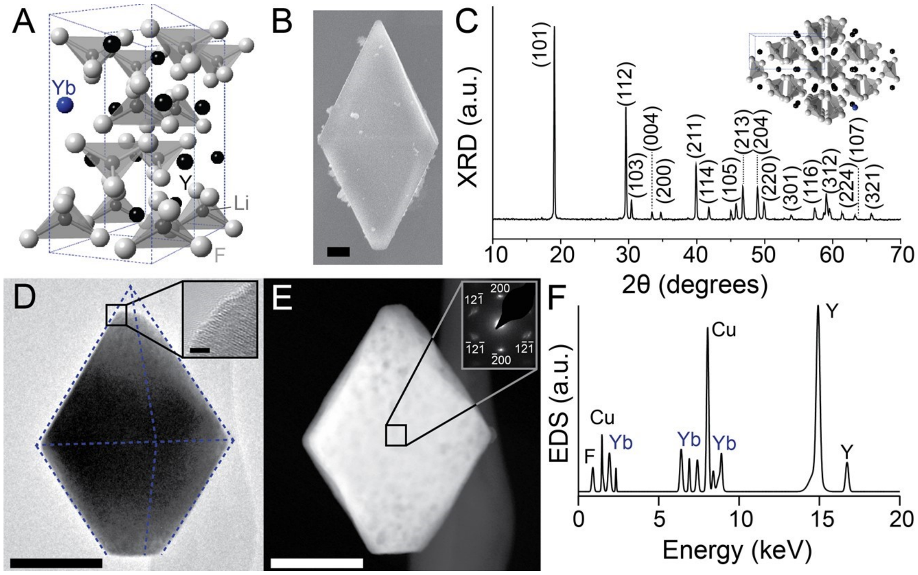

Figure 2.1: Synthesis and characterization of YLF crystals. (A) Schematic of Scheelite crystal structure of YLF with I41/a space group symmetry. (B) Scanning electron microscope image of a faceted (Yb^{3+})0.1(Y^{3+})0.9LiYF$_4$ particle exhibiting truncated tetragonal bipyramidal morphology. Scale bar = 1 μm. (C) Powder x-ray diffraction pattern of YLF crystals following hydrothermal synthesis indicating a pure Scheelite crystal phase. Inset: schematic of truncated tetragonal bipyramidal morphology relative to YLFs unit cell. (D) Bright field TEM image of an individual Yb^{3+}:YLF grain; scale bar = 200 nm. Inset: high-resolution TEM image taken from the indicated region; scale bar = 2 nm. (E) High-angle annular-dark-field (HAADF) image of the YLF grain in panel B showing regions of high contrast suggesting the presence of polycrystalline domains. Inset: select area electron diffraction from the indicated region. (F) X-ray fluorescence compositional-analysis-spectrum of an individual YLF crystal taken within the TEM confirming the elemental crystalline composition including Y, Yb, and F species.[3]

Then they were dissolved in deionized water to achieve certain concentration of rare earth nitrates. Lithium fluoride (LiF), nitric acid (HNO$_3$), ammonium bifluoride (NH$_4$HF$_2$) and ethylenediaminetetraacetic acid (EDTA) are analytical grade and used directly in the synthesis without any purification. Millipore-deionized (DI) water was used for every experiment.

The following preparation uses the synthesis of 2%Er^{3+}10%Yb^{3+}:$LiYF_4$ as an example. 7.04 ml of 0.5 M $Y(NO_3)_3$, 0.8 ml of 0.5 M $Yb(NO_3)_3$ and 0.16 ml of 0.5 M $Er(NO_3)_3$ were mixed with 1.17 g EDTA in 5 ml Millipore DI water at 80 ^{o}C while stirring for 1 hour, denoted as solution A. Subsequently, 0.21 g of LiF and 0.68 g of NH_4HF_2 were dissolved in 7 ml Millipore DI water at 70 ^{o}C while stirring for 1 hour to form solution B. Solutions A and B were mixed together while stirring for 20 minutes to form a homogeneous white suspension which is then transferred to a 23 ml Teflon-lined autoclave and heated to 220 ^{o}C for 72 hours. After the autoclave cools to room temperature, the 2%Er^{3+}10%Yb^{3+}:$LiYF_4$ particles can be recovered by centrifuging and washing with ethanol and Millipore DI water three times. The final white powder is obtained by calcining at 300 ^{o}C for 2 hours. 10%Yb^{3+}:$LiYF_4$ particles were achieved using the same method.

Bright field and STEM HAADF images were taken on a FEI Tecnai G2 F20 at an accelerating voltage of 200 keV. Select area electron diffraction images were taken with a camera length of 490 mm. EDS spectra were obtained with a 60 second acquisition time. The spectra were then processed by subtracting the background and smoothing the peaks. Secondary electron images were taken on an FEI Sirion at an accelerating voltage of 5 keV. XRD Characterization. Powder XRD patterns were obtained on a Bruker F8 Focus Powder XRD with Cu K (40 kV, 40 mA) irradiation (= 0.154 nm). The 2θ angle of the XRD spectra is from 10 to 70 and the scanning rate is 0.01s1. The one minor unlabeled peak in the XRD spectra at $2\theta = 44.9^o$ is attributed to a small amount of unreacted LiF precursor ((200) peak). Pioneering efforts to cool Yb^{3+}:YLF materials in vacuo have relied on the growth of high-purity YLF single-crystals using an air- and moisture- free Czochralski process. In the experiments reported here, a low-cost modified hydrothermal synthesis of Yb^{3+}:YLF is used to prepare crystals shown in Fig 2.1. Scanning electron microscopy reveals that YLF crystals exhibit a truncated tetragonal bipyramidal (TTB) morphology (Fig 2.1B). X-ray diffraction shows that the YLF crystal has a Scheelite structure (Fig 2.1C). Bright field / HAADF TEM imaging (Fig 2.1D/E) shows uneven contrast and electron diffraction shows expanded bright diffraction spots, which suggests that the TTB materials were polycrystalline and likely form through an oriented attachment process of nanocrystalline grains (Fig 2.1E, inset).[15]

According to the XRD data presented in Fig 2.1C of the main document and detailed in Materials and Methods, the lattice parameters of 10%Yb^{3+}:YLF are a = 5.1641 Å and c = 10.7177 Å and the volume of the corresponding unit cell is $V_0 = a^2 \cdot c = 2.85 \cdot 10^{-28}$ m^3. For 1 m^3 YLF, the number of unit cells is $n = 1\ m^3/V_0 = 3.5 \cdot 1027\ m^{-3}$. For each unit cell, there are 4 rare earth atoms. The total number of rare earth atoms in 1 m^3 is $n_t = 4n = 1.4 \cdot 10^{28}\ m^{-3}$. For 10%$Yb^{3+}$:YLF, the number of Yb atoms in 1 m^3 is $n_{Yb} = 0.1 \cdot n_t = 1.4 \cdot 10^{27}\ m^{-3}$. The linear density of Yb atoms is $\rho = (n_{Yb}) \cdot (1/3) = 1.11 \cdot 10^8\ m^{-1}$ and the average ion spacing is approximately $l = 1/\rho = 8.9$ Å.

2.3 NaYF$_4$ synthesis and characterization

2.3.1 NaYF$_4$ synthesis

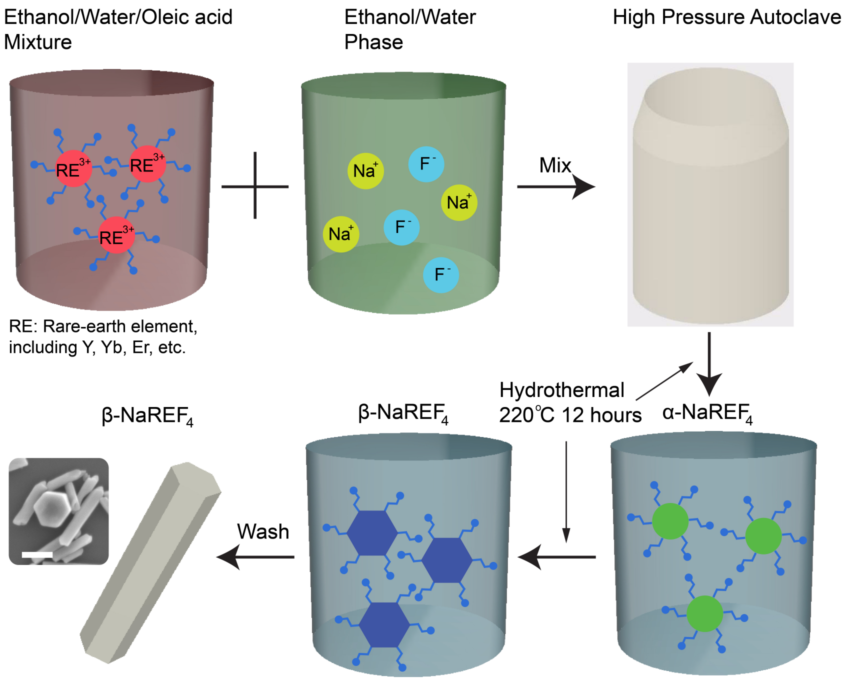

Figure 2.2: Schematic of hydrothermal synthesis of NaYF$_4$ nanocrystals

The synthesis of NaYF$_4$ was performed with following minor modifications to Ref[16]. The procedures are shown in Fig.2.2. RECl$_3$, Sodium hydroxide (NaOH), sodium fluoride (NaF), oleic acid are analytical grade and used directly in synthesis without any further purification. Millipore-DI water was used for every experiment. The preparation process as followed assumes the synthesis of 10%Yb^{3+}/1%Er^{3+}:NaYF4 as an example. 0.89 ml of 1 mol/L Y(Cl$_3$)$_3$, 0.1 ml of 1 mol/L Yb(Cl$_3$)$_3$ and 0.01 ml of 1 mol/L Er(Cl$_3$)$_3$ were mixed with 2 ml DI water and 8 ml ethanol. Then, 3 ml oleic acid and 0.23 g NaOH were mixed and stirred producing solution A.

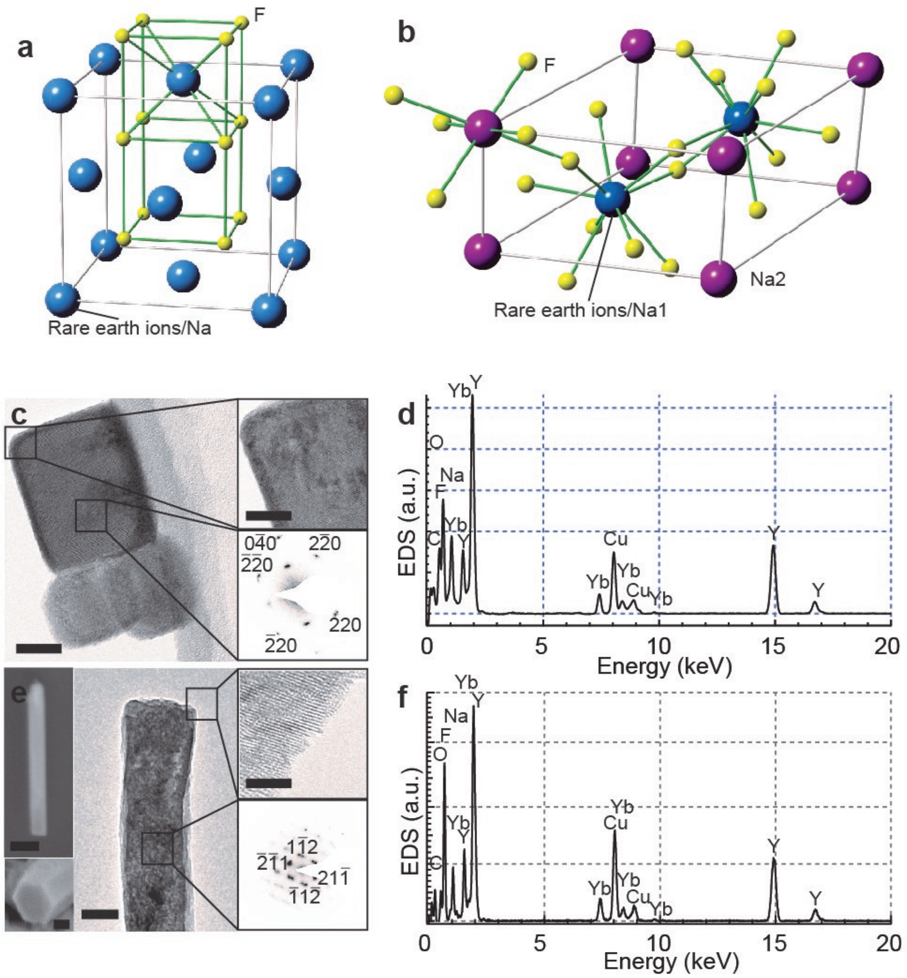

Figure 2.3: Synthesis and characterization of $NaYF_4$ crystals. (a) Schematic of cubic crystal structure of α-$NaYF_4$ with Fm-3m space group symmetry. (b) Schematic of hexagonal crystal structure of β-$NaYF_4$ with P63/m space group symmetry. (c) Bright field TEM image of α-$NaYF_4$:10%Yb grains; scale bar = 18 nm. Top inset: high-resolution TEM image taken from the indicated region; scale bar = 15 nm. Bottom inset: select area electron diffraction from the indicated region. (d) X-ray fluorescence compositional-analysis-spectrum of an individual α-$NaYF_4$:10%Yb crystal taken within the TEM confirming the elemental crystalline composition including Y, Yb, and F species. (e) Top left: SEM image of β-$NaYF_4$:10%Yb particle exhibiting rod shape; scale bar = 240 nm. Bottom left: SEM image of a faceted β-$NaYF_4$%Yb particle exhibiting hexagonal face; scale bar = 100 nm. Middle: Bright field TEM image of β-$NaYF_4$%Yb grains; scale bar = 20 nm.Top inset: high-resolution TEM image taken from the indicated region; scale bar = 4 nm. Bottom inset: select area electron diffraction from the indicated region. (f) X-ray fluorescence compositional-analysis-spectrum of an individual β-$NaYF_4$%Yb crystal taken within the TEM confirming the elemental crystalline composition including Y, Yb, and F species.[10]

For solution B, 168 mg NaF was mixed with 3 ml DI water and 3ml ethanol with stirring. After 30 minutes of stirring for both solution A and B, solution B was added drop by drop to solution A under vigorous stirring. With an additional 30 minutes of aging, the mixture was transferred into a 25 ml Teflon lined autoclave for 5 hours at approximately 200 ^{o}C to undergo hydrothermal treatment. After the autoclave was cooled down to room temperature, the particles were washed and centrifuged with water and ethanol three times. The final white powder was obtained by after drying the product around 60 ^{o}C for 12 hours. With varying the reaction temperature from 100^{o}C to 220^{o}C and dopant concentration, different phases, size, morphology, and dopant concentration of $NaYF_4$ nanocrystal can be achieved. The cubic $NaYF_4$ has a Fm-3m space group symmetry as shown in Fig.2.3a. The size and morphology of the cubic $NaYF_4$ nanocrystals are shown in Fig.2.3c. The α-$NaYF_4$:10%Yb nanocrystal's elementary composition was confirmed by TEM EDS as shown in Fig.2.3d. Bright-field, HR-TEM SAED shows the expanded nonuniform diffraction spot instead of uniform circular spot, which suggests that the α-$NaYF_4$:10%Yb NWs are cubic polycrystalline nanocrystals. The β-$NaYF_4$:10%Yb NWs exhibit a hexagonal crystal structure shown in Fig.2.3c with P63/m space group symmetry. Scanning electron microscopy (SEM) (Fig.2.3d) indicates that the NWs have a hexagonal cross-section. Energy dispersive x-ray spectroscopy (EDX) compositional analysis on an individual β-$NaYF_4$:10%Yb NW (Fig.2.3f) quantified the elemental composition of the material containing Na, Y, F, and Yb. Bright-field, HR-TEM imaging and SAED shows with arcs instead of spots, which suggests that the β-$NaYF_4$:10%Yb NWs are polycrystalline and the non-uniform contrast of the nanowire in Fig. 2.3d may be due to an oriented attachment growth mechanism of the nanowires, or electron beam damage generated from TEM imaging.

2.3.2 NaYF$_4$ morphology control

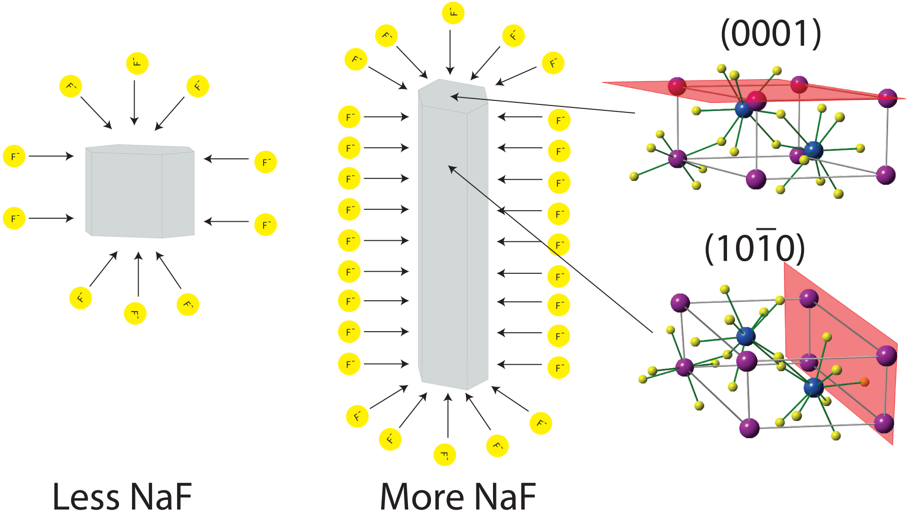

Figure 2.4: Aspect ratio modification mechanism

Compared to α-NaYF$_4$, β-NaYF$_4$ phase has higher upconversion efficiency and is more thermodynamic stable. Due to surface energy differences, the small NaYF$_4$ nanocrystals prefer to have the isotropic phase, cubic phase, than the anisotropic phase, hexagonal phase, in which smaller crystal size cause higher surface energy. In this case, size driven phase transition from cubic phase to hexagonal phase occurs with longer reaction time and higher reaction temperature.[17] The transition from cubic phase to hexagonal phase is a thermodynamically driven, which is a disorder to order process. The β-NaYF$_4$ phase growth can be controlled by the kinetics of the system.

With increasing the NaF:RE^{3+} ratio, the β-NaYF$_4$ nanocrystals tend to form, which means the diameter of the cross section decreases. For large NaF:RE^{3+} ratios, the excessive F$^-$ compared with the Y^{3+} will cap the surface of the crystal due to the coordinating effect between F$^-$ and Y^{3+}, which is shown in Fig.2.4 The Y^{3+} planar density is different along different crystal planes. Larger Y^{3+} planar densities will cause more F$^-$ capping on the surface, which decreases the number of the dangling bonds of certain directions of crystal planes. According to the Gibbs-Thompson theory, the relative chemical potential of a crystal is proportional to the surface/atom ratio. Larger surface/atom ratios, more dangling bonds per atom over entire crystal, will lead to larger chemical potential. For the β-NaYF$_4$ nanocrystals, the RE^{3+} density on (10-10) crystal plane is higher than (0001) crystal plane. Therefore, the F$^-$ capping effect will be greater on the (10-10) crystal plane, meaning less dangling bonds on that plane. So, the chemical potential of (0001) crystal plane is higher than (10-10) crystal plane, leading to a smaller surface area at equilibrium on the (0001) plane.

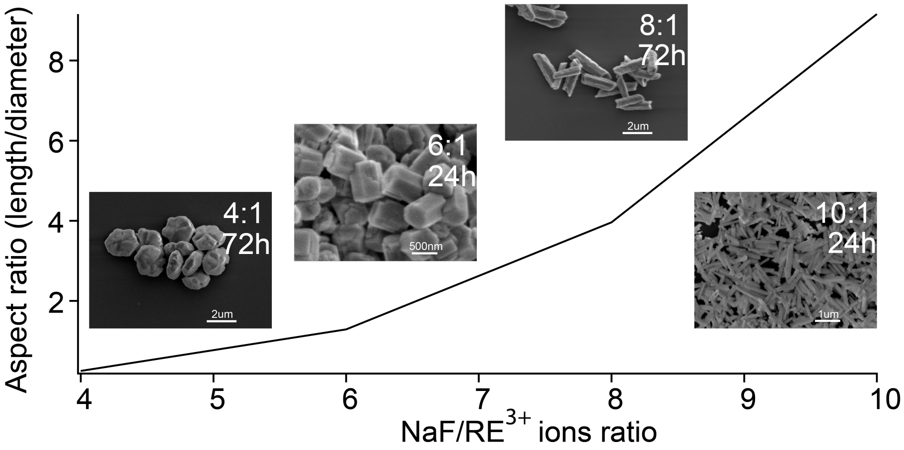

Figure 2.5: Aspect ratio (length/diameter) with different RE ions : NaF ratio. The SEM pictures are (left to right) 1:4 with 72h reaction time, scale bar = 2 μm; 1:6 with 24h reaction time, scale bar 500 nm; 1:8 with 72h reaction time, scale bar 2 μm; 1:10 with 24h reaction time, scale bar = 1 μm.

The different crystal morphologies of the β-NaYF$_4$ nanocrystals are as shown in

Fig.2.5. Additionally, the coordination number of Y^{3+} is 12 in the β-$NaYF_4$ nanocrystals structure. In other words, there are 12 F^- around one Y^{3+} cationic site. At higher NaF/RE^{3+} ratios, the β-$NaYF_4$ nanocrystals tend to have higher length/diameter ratio. The oleic/NaOH ratio also affects the shape of β-$NaYF_4$ nanocrystals. The organic molecules tend to selectively adsorb on the (0001) surface, which results in lower surface energy of that crystal plane. Then, the crystal tends to grow along (10-10) direction, which results in disk shape β-$NaYF_4$ nanocrystals formation. Zhang.et al had also done the study of increasing the chain length of the ligands to control the morphology of the β-$NaYF_4$ nanocrystals.[18] With increasing chain length, boiling/melting points of the ligands increased and were less mobile, leading to a decreased possibility of the ligands removal. With preferential absorption on (0001) crystal plane, the β-$NaYF_4$ nanocrystals would have a lower length/radius ratio with increased chain length of the ligands.

2.3.3 Local structure characterization X-ray absorption spectroscopy study

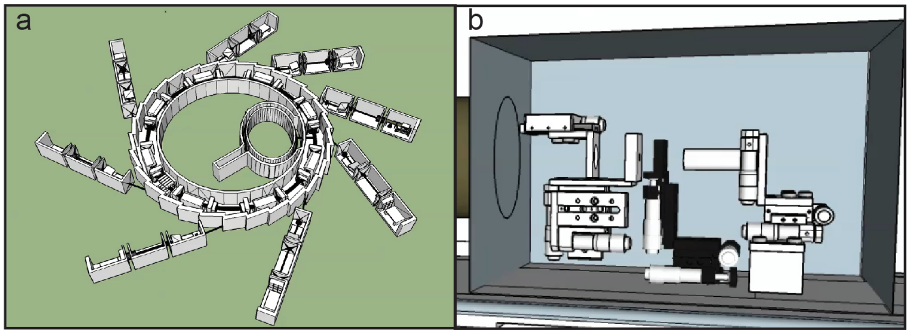

Figure 2.6: Schematic of synchrotron level STXM setup. (a) Schematic of synchrotron accelerator. (b)Schematic STXM setup

The unique 4f transitions of RE^{3+} ions enable specific spectral properties within the RE-doped-fluoride nanocrystals. Some of these are narrow emission line width, strong upconversion, tunable emission wavelengths, etc. The material properties, including crystallinity, impurities, lattice phonon energy, dopant ion oxidation state, can also impact the optical properties. For the laser cooling of solid state materials, background absorption, especially Fe ions impurity absorption, is a crucial factor that disturbs the overall cooling efficiency. With the lower ppm concentrations of Fe ions, the background absorption of laser light can generate comparative heat compared with the cooling efficiency. To detect such low ppm concentrations of Fe ions, various of methods, including ICP, XPS, XAFS, can be applied. Synchrotron level X-ray absorption spectroscopy is used for the detection, which is shown in Fig.2.6. NEXAFS spectroscopy was achieved from STXM at LBNL ALS beamline 5.3.2.2. Samples for STXM analysis were prepared by drop casting a solution of $NaYF_4$ onto a lacy-carbon TEM grid and placing the grid in the STXM beamline under a helium environment. Soft x-rays (250-800 eV) were focused onto the sample and rastered with a spot size of 31 nm using 25 nm Fresnel zone plates.

Both the cubic and hexagonal phases of $NaYF_4$ have been examined with XANES on fluorine K edge and iron L2, L3 edges. The fluorine k edge for both phases match very well. There is no absorption peak in the iron L2 and L3 edges regions which is located in the dashed circles as shown in Fig.2.7. The absence of Fe absorption was related to less than ppm Fe impurity ions within the crystal, which proves the one of the advantages of using hydrothermal synthesis to make fluoride nanocrystals for laser cooling of solid state materials.

In addition to the impurity absorption heat generation, the concentration quenching also plays an important role. For a perfect crystal structure, with no internal or surface defects, the higher dopant concentration leads to the higher laser cooling efficiency. However, no perfect crystal exists, meaning all the crystals have defects, such as point defects, grain boundaries, impurities and etc.

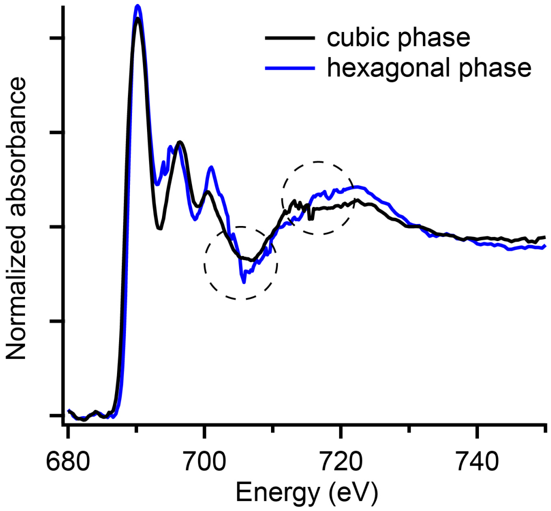

Figure 2.7: XANES spectra of both cubic and hexagonal $NaYF_4$

The Yb^{3+} ions absorb the excited phonon energy and then transfer the energy to nearby RE acceptor ions for upconversion, or release a higher photon energy for laser cooling. Since the electron has a long lived lifetime at the excited state of Yb^{3+}, it can transfer between different Yb^{3+} ions. The higher concentration of Yb^{3+} ions, results in less distance between them and therefore higher possibilities of transferring the energy between different ions. Potential energy transfer to internal or external defects can cause nonradiative relaxation, which generates heat. This process is known as concentration quenching. To prevent this from occuring, an optimum concentration of dopant was used for laser cooling or upconversion. However, the RE dopants can either be uniformly distributed or clustered in the crystal. The latter way may also result in concentration quenching. To measure the dopant distribution in the fluoride nanocrystals, EXAFS was used for dopant ion distribution study. EXAFS

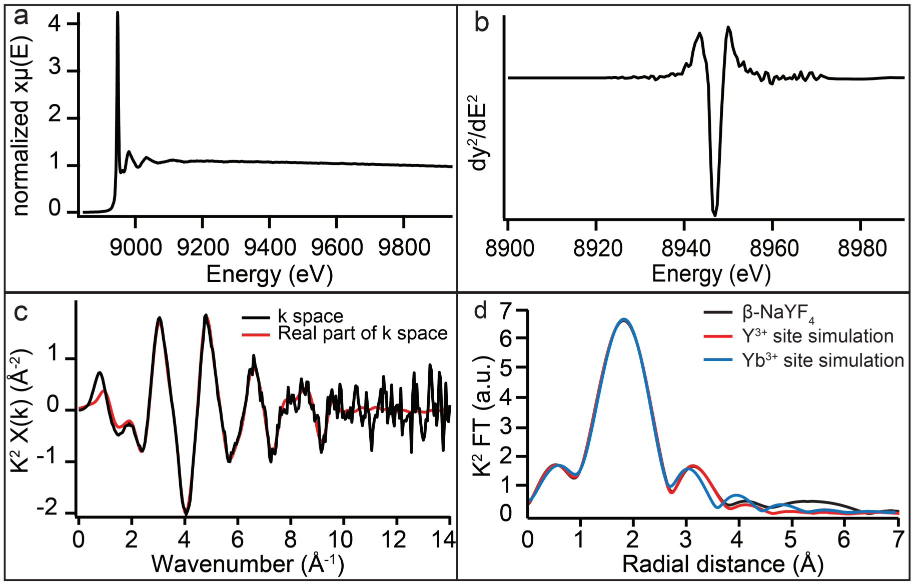

Figure 2.8: EXAFS analysis of β-NaYF$_4$:10%Yb nanocrystals. (a) EXAFS of Yb^{3+} L3 edge of β-NaYF$_4$:10%Yb nanocrystals. (b) The second derivative of X-ray near edge of Yb^{3+} L3 edge of β-NaYF$_4$:10%Yb nanocrystals. (c) k^2 weighted Yb^{3+} L3 edge of β-NaYF$_4$:10%Yb nanocrystals. (d) The k^2 weighted Fourier transforms of Yb^{3+} L3 edge of β-NaYF$_4$:10%Yb nanocrystals.

spectroscopy was measured from LBNL ALS beamline 10.3.2.2. Samples for EXAFS analysis were prepared by drop casting a solution of NaYF$_4$ onto an X-ray transparent kapton tape and placing the tape under the EXAFS beamline under a helium environment. Hard x-rays (2100 - 17,000 eV) were focused onto the sample. The Yb^{3+} L3 edge EXAFS spectra is shown in Fig.2.8a. A K2 weighted spectra of EXAFS spectra is plotted in Fig.2.8c. After Fourier transform of plot in Fig.2.8c, the Yb^{3+} ions distribution plot is obtained in Fig.2.8d as the black line. Two different models were built and simulated with FEFF9 for β-NaYF$_4$ structure. One where Yb^{3+} is uniformly distributed in the lattice structure, in which the Yb^{3+} is surrounded with all Y^{3+} at the nearest RE site. This is shown in the red plot. The other model is Yb^{3+} is clustered in the crystal structure, where the nearest RE site around center Yb^{3+} are all Yb^{3+} ions. With comparison in Fig.2.8d, the red plot is much similar to the experimental data compared with the blue plot, meaning the Yb^{3+} ions are uniformly distributed in the $NaYF_4$ nanocrystal.

Beyond the concentration quenching effect, Yb ions oxidation states also affect the laser cooling or upconversion efficiency. The Yb^{3+} donates three electron, including two from the 6s and one from 4f shell. The one missing electron from 4f shell generates energy levels by spin-orbit coupling. With doping Yb^{3+} in the crystal structure, the electron feels the perturbation from the electric field inside the crystal, which results in further crystal field splitting. However, if the Yb ion is Yb^{2+}, the 4f shell of Yb^{2+} is full. This results in no energy level for NIR photon absorption, which can not be used to perform laser cooling or upconversion. To study the existence of Yb^{2+} in the $NaYF_4$ nanocrystal, a second derivative of the Yb L3 near edge absorption spectra is plotted in Fig.2.8b. The difference between Yb^{2+} and Yb^{3+} is the absorption white line energy difference. If there is Yb^{2+}, there will be a second peak in addition to the Yb^{3+}. However, from Fig.2.8b, there is only peak present, confirming the existence of Yb^{2+} in the nanocrystal below ppm level.

Chapter 3

GROWTH MECHANISM STUDY OF HYDROTHERMALLY SYNTHESIZED FLUORIDE NANOSTRUCTURES

3.1 Introduction

Hydrothermal synthesis of fluoride nanocrystals have unique advantages compared with other synthetic routes, which are: 1) Size, morphology, structure, phases of the nanocrystals are controlled by hydrothermal conditions, such as reaction temperature, reaction duration, ratio of reagents, capping agents, and others. 2) The reaction occurs at relatively low temperature (usually less than 250 ^{o}C). 3) The reaction provides high purity nanocrystals due to the recrystallization process. 4) The reaction requires simple equipment and process. 5) The synthesis is low cost and scalable for industrial application. Our previous study has reported hydrothermal synthesis of $LiYF_4$ nanocrystals with EDTA as the chelator. Recently, we have also utilized oleic acid as the chelator preparing $NaYF_4$ nanocrystals with hydrothermal synthesis. In this work, we perform a systematic study on the synthetic mechanism of hydrothermal synthesis of sodium yttrium fluoride nanocrystals. A common synthetic route of $NaYF_4$ nanocrystals is described as followed. A mixture of oleic acid, water, and ethanol is added with NaOH to form OA/OA$^-$, water, and ethanol designated as mixture A. After adding $RECL_3$ to the mixture A, the solution changes from transparent into white soluble flocs due to the complexation of RE^3 and OA/OA$^-$ molecules. After stirring for 30 minutes, a solution of NaF in ethanol and water, mixture B, is added drop by drop into mixture A, which forms further a white cloudy solution due to the formation of nucleates. After aging and stirring for another 30 minutes, the solution is put into a sealed teflon liner and tightened within a stainless steel autoclave followed by heating in an oven. Here, we report the microemulsion droplet nucleation, growth, and mass transfer at the early stages of the synthesis for the first time with in-situ liquid cell TEM. The nanocrystals aggregation, oriented attachment, growth, dissolution and recrystallization have also been observed with in-situ liquid cell TEM. Phase transformation of cubic α-$NaYF_4$ nanocrystals to hollow structure hexagonal β-$NaYF_4$ nanocrystals have been investigated with in-situ heating TEM experiments. The hollow structure can be explained by dissolution and recrystallization instead of Kirkendall effect, which was confirmed with XANES carbon K-edge spectra and fluorine K-edge spectra of the nanocrystals. Our results suggested that the nanocrystal growth mechanism and hollow structures formed during heat treatment could be potentially extended to other fluoride host materials systems. Based on the understanding of formation mechanism, tuning the synthesis procedures can potentially improve the upconversion efficiency for various applications, including bio-imaging, bio-labeling, photothermal therapy, solar cell, color display, and others.

3.2 Characterization methods

The cryo-TEM sample of 0.5 uL $NaYF_4$ precursor mixture was prepared with FEI Vitrobot with one time blotting for 6.5 s at the force of 1. FEI TECNAI F12 TEM with FEI cryo holder was used to characterize the $NaYF_4$ precursor mixture with a voltage of 120 keV. The operation was under the software of Leginon for automatic TEM images taken. The HAADF TEM image of the $NaYF_4$ nanocrystals were taken with Titan TEM at 200 keV in National Center of Electron Microscopy located at LBNL. All the other TEM images were taken with FEI TECNAI F20 with 200 keV voltages. The in-situ liquid cell TEM images were taken with the Hummingbird liquid flow cell TEM holder. The XRD patterns were obtained by Bruker F8 Focus Powder XRD with Cu Kα (40 kV, 40 mA) irradiation ($\lambda = 0.154$ nm). The scanning rate was $0.01^o s^{-1}$. The XANES spectra were collected from Beamline 5.3.2.2 at Advanced Light Source Synchrotron in LBNL. The EXAFS spectra were collected from Beamline 10.3.2 at Advanced Light Source Synchrotron in LBNL.

3.3 Hydrothermal synthesis mechanism

Hydrothermal synthesis of nanocrystals with o/w microemulsion systems have been widely used to control the size and shape of the nanocrystals.[19] For the $NaYF_4$ nanocrystal synthesis described in chapter 2, the NaOH reacts with the oleic acid to form sodium oleate first. With RE ions added in the solution, reverse micelles containing RE^{3+} formed, which means the RE ions are trapped in the center with the hydrophilic head groups and the hydrophobic tails extending out. Then the water and oleic acid mixed with NaF solution slowly dropped into the RE solution, which forms microemulsion. The oleate anions behaved as metal-coordinating group on one side and solvophlic group on the other. RE ions inside the microemulsion can react with fluorine ions and oleate group same time. Compared with emlusion system, the microemulsion system usually has droplet less than 100 nm in diameter, which spontaneously forms a transparent stable structure. The difference between the o/w microemulsion structure and reverse micelle structure is the molar ratio of the water/oil content. The o/w microemulsion usually contains higher amounts of water which results in the ratio greater than 10 15. The reverse micelle structure usually contains tiny amounts of oil which can be neglected in the mixture of water/surfactant/oil mixture.

Different types of oil can be used in the synthesis based on the carbon chain length to perform stronger or weaker capping effects of the water molecules inside. The microemulsion water in oil droplet can be tuned to kinetically stable status with varying the relative ratio of different components, including water, oil, surfactant, and cosurfactant. One common type of cosurfactants is alcohol. Due to its miscibility with both water and oil, the cosurfactant can distribute between the water/oil interface to lower the surface tension. The cosurfactants can co-exist with oil ligands on the surface of the water droplet to lower the surface tension, in which the water droplet in the microemulsion is kinetically more stable. To control the droplet concentration and size distribution, different types and amounts of cosurfactants can be added in the microemulsion. The shorter chain size of the cosurfactants can be easily incorporated in the water/oil surface, which can decrease the size of the droplet. The amounts of cosurfactants in the microemulsion system can also tune the concentration of micromulsion droplet sizes and concentration, which can further tune the crystal nucleates size and number. The hydrothermal synthesis of $NaYF_4$ nanocrystals are involved in oleic acid, water, and ethanol system. Oleic acid is a fatty acid while occuring 18 carbon atoms in one molecule and it also occurs naturally in various animal and vegetable fats and oils, such as olive oil. The ethanol is added as the cosurfactant in the system.

To better understand how the volume ratio of the three different chemical compounds can affect the microemulsion system, a titration experiment was conducted to get a ternary phase plot, as shown in Fig.3.1. A pre-mixture of water and oleic acid was titrated with ethanol until the transparent mixture is formed, which indicated the formation of microemulsion. The different sections in the ternary phase plot represent different status of the mixtures, where A region is the heterogeneous mixture and B is the microemulsion region.

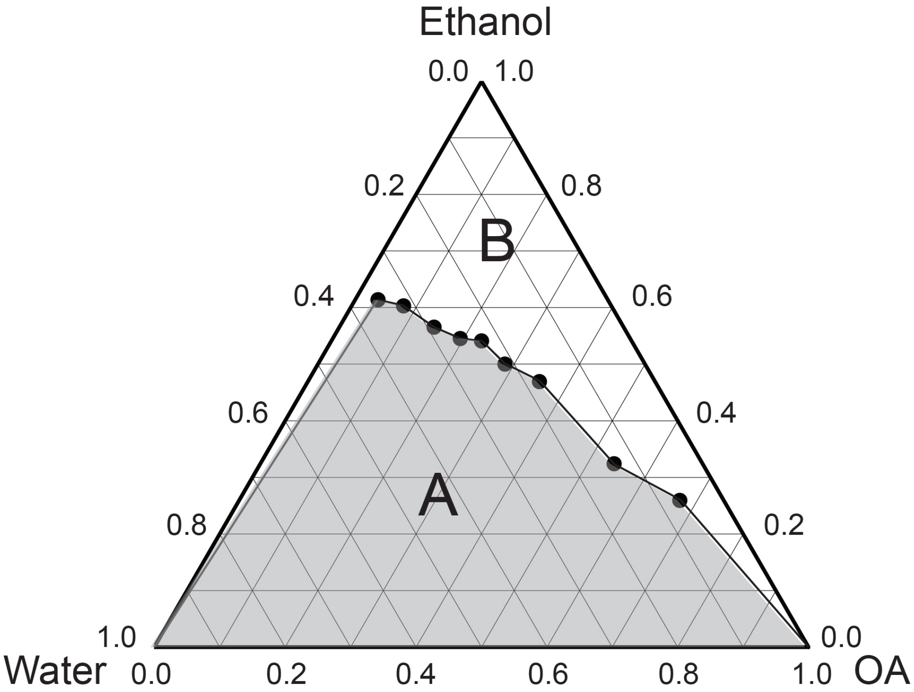

Figure 3.1: Ternary phase plot for ethanol, water, and oleic acid mixture.

As mentioned earlier session, the $NaYF_4$ reaction precursors are mixed before heating in oven. The mixture should form microemulsion structure, which should be in B region of the ternary plot. To prove the microemulsion generation, cryo-TEM was used to characterize the microemulsion droplet. The $NaYF_4$ precursor mixture was prepared with holey carbon TEM grids and checked in the cryo-TEM. The expected spherical droplets were confirmed with TEM images shown in Fig.3.2b. The structure of the water in oil microemulsion droplet is shownin Fig.3.2a. A free water solution containing different ions including RE ions, sodium ion, and fluorine ions is captured with a rigid bounded water layer that confined by both oleate ligand surfactant and ethanol cosurfactant. At room temperature, the microemulsion is kinetically stable. After the microemulsion sealed within a teflon liner and put into an oven, as temperature increases, the microemulsion tends to nucleate and form a metastable cubic $NaYF_4$ phase at lower temperature (usually ¡ 130^{o}C), as shown in Fig.3.2c. As temperature continually rises, the metastable cubic phase will turn into a thermodyncamically more stable hexagonal $NaYF_4$ structure, as shown in Fig.3.2d.

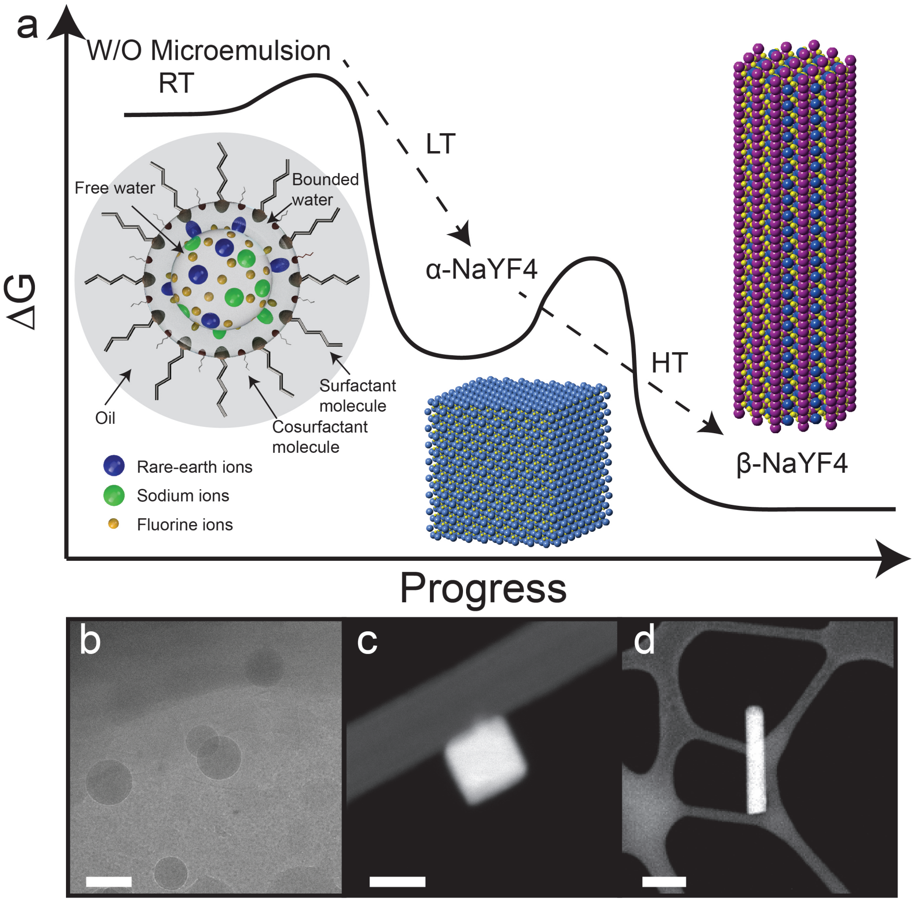

Figure 3.2: Different stages of $NaYF_4$ formation progress. (a) Schematic of $NaYF_4$ formation progress.(b) Cryo-TEM image of $NaYF_4$ microemulsion. scale bar = 200 nm; (c) HAADF TEM image of α-$NaYF_4$. scale bar = 50 nm; (d) HAADF TEM image of β-$NaYF_4$. scale bar = 1 μm.

This phase transformation process has been confirmed with synthetic time dependent ex-situ TEM and XRD data. Same synthetic conditions are kept for the synthesis, except the reaction times are changed. For both half hour and one hour synthesis time, the final products are both pure cubic phase $NaYF_4$. The one hour sample has larger diameter size compared to the half hour sample.

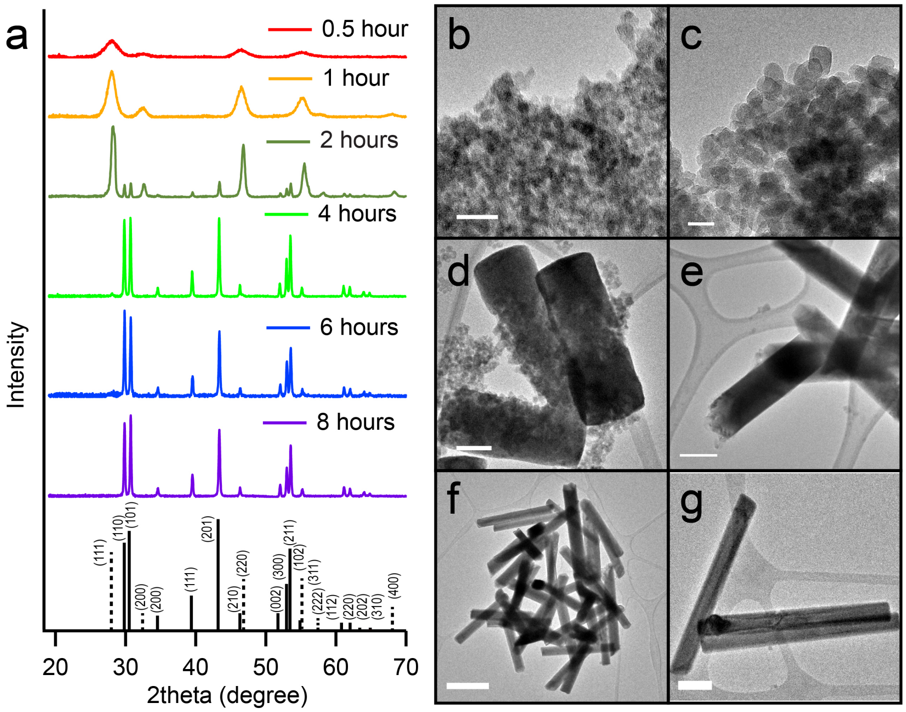

Figure 3.3: Characterization of hydrothermally synthesized $NaYF_4$ at different synthetic times. (a) XRD of hydrothermally synthesized $NaYF_4$ at different synthetic times.(b-g) TEM of hydrothermally synthesized $NaYF_4$ at different synthetic times. (b) 0.5 hour, scale bar = 20 nm; (c) 1 hour, scale bar = 20 nm; (d) 2 hours, scale bar = 200 nm; (e) 4 hours, scale bar = 200 nm; (f) 6 hours, scale bar = 1 um; (g) 8 hours, scale bar = 200 nm.

As time increases, the hexagonal phase $NaYF_4$, represented by the rod shape, starts forming, with a coexisting cubic $NaYF_4$ phase. From Fig.3.3d, it can be seen that the $NaYF_4$ nanorods are partially composed of cubic phase $NaYF_4$ nanocrystals.

With time range from 2 hours to 8 hours, the XRD patterns show that the phase transforms completely from cubic phase to hexagonal phases. The TEM images also show the transformation in terms of morphology changing as time increases. Fig.3.3g shows the final product of hexagonal $NaYF_4$ nanorod with smooth surface, which indicates Ostwald ripening occurs during the synthesis.

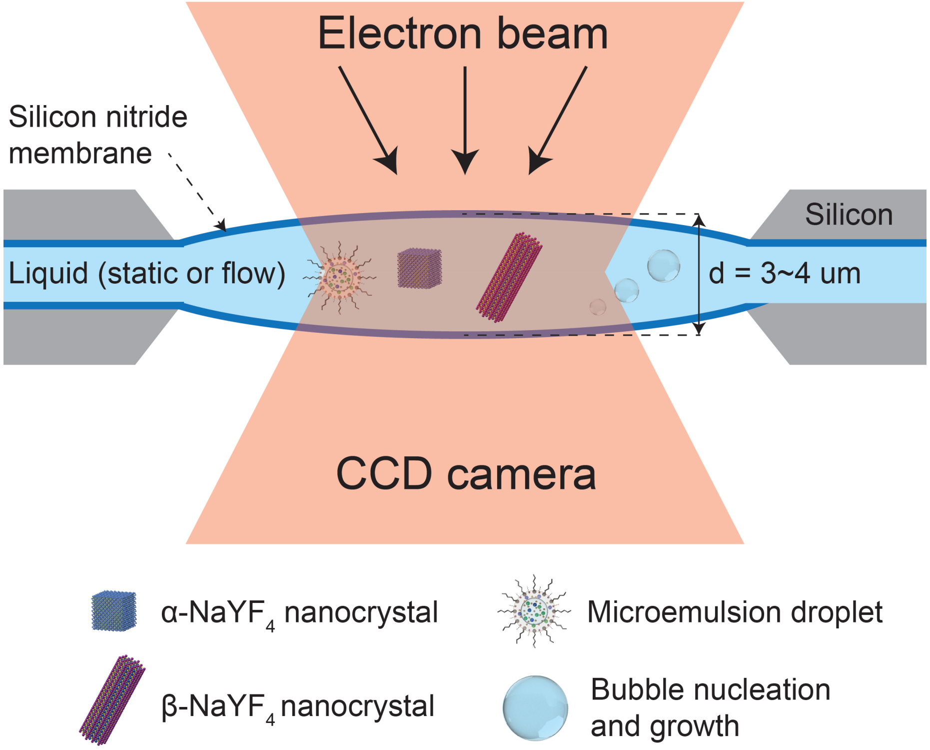

Figure 3.4: Schematic diagram of a liquid cell for the transmission electron microscope and its application for imaging phenomena in materials science, life science, and physics.[20]

Hexagonal $NaYF_4$ nanorods formation can be explained with microemulsion formation, nanocrystal nucleation, cubic nanocrystal formation, cubic nanocrystal aggregation and attachment on hexagonal nanocrystal, Ostwald ripening, and atom diffusion to obtain final product. To further examine the dynamic processes occuring during the synthesis, in-situ liquid cell TEM technique was applied to characterize the formation of $NaYF_4$ nanostructures.[20]The structure of the liquid cell is shown in Fig.3.4, where two electron transparent thin films, usually silicon nitride windows, enclosed a thin layer of liquid with a thickness ranging from 100 nm to 1 mm.

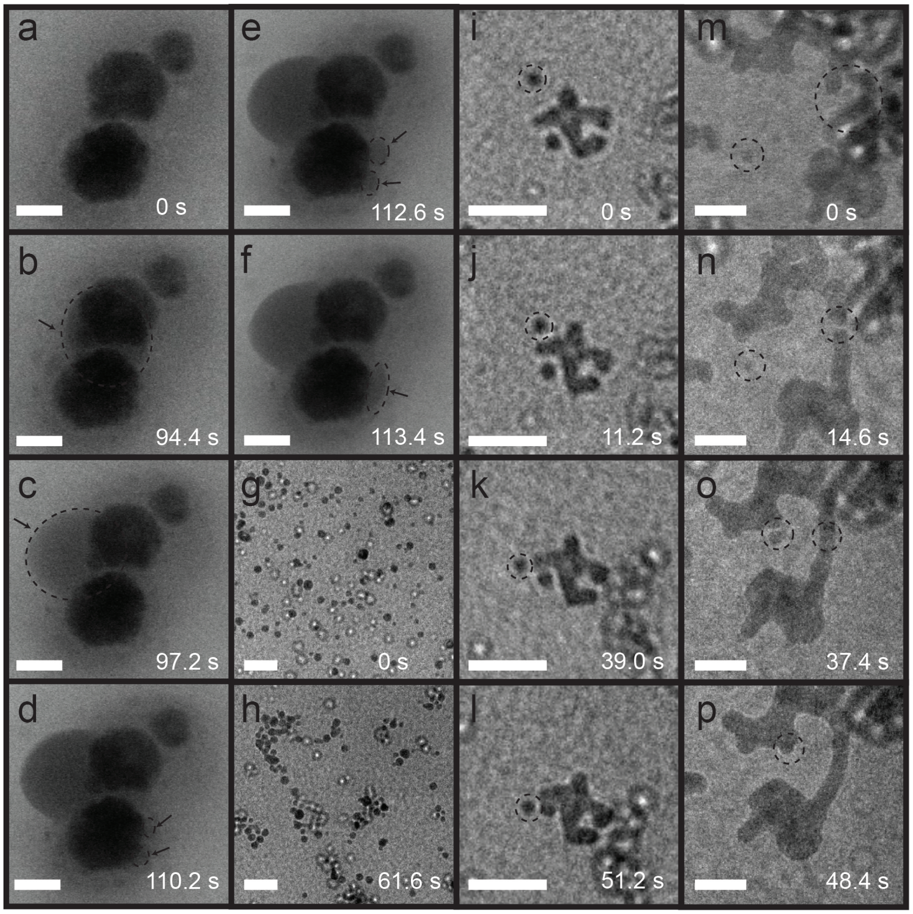

Figure 3.5: Characterization of $\mathrm{NaYF_4}$ formation progress with in-situ liquid cell TEM. (a-f) In-situ TEM images of microemulsion droplet formation, growth, and mass transfer. scale bar = 100 nm (g-h) In-situ TEM images of α-$\mathrm{NaYF_4}$ nanocrystals aggregation in liquid. scale bar = 10 nm; (i-j) In-situ TEM images of α-$\mathrm{NaYF_4}$ nanocrystal oriented attachment. scale bar = 20 nm; (m-p) In-situ TEM images of α-$\mathrm{NaYF_4}$ nanocrystal attachment. scale bar = 10 nm.

The liquid layer which contains the nanomaterials or reactants can be static or flowable with an external syringe pump at low speed. The electron beam with the dose rate of 40 e/Å^{2}s passes through the liquid layer to collect images, videos, or spectroscopic data.

Fig.3.5(a-b) shows the reaction precursors after stirring and aging for 30 minutes with flowing through the liquid cell inside the TEM. The liquid reaction precursors are the same from hydrothermal reaction. The amorphous droplet forms after 94.4 s with flowing reaction precursor in oleic acid/water/ethanol mixture. The droplet can also move to different locations, in which surface tension is lowered for a more stable status.

Fig.3.5(d-f) show a series of amorphous droplets growth and combination processes. There are two little amorphous droplets forming in Fig.3.5(d) and they grow to bigger droplets as shown in Fig.3.5(e). Finally, they combine to one big droplet in Fig.3.5(f), which is direct evidence of mass transfer. The combination process can help droplets exchange or combine ions for further nucleation. The precursor size and ion molar ratios can affect the nucleation size and phase, which influences the reaction progress to obtain different size and morphology of the final product. Due to the existence of oleate ligand hydrophobic group, the nanocrystals are easily attached on the surface of liquid cell silicon nitride window. To further observe the nanocrystals' Brownian motion in liquid phase, the 30 minute $NaYF_4$ precursor sample was diluted with Millipore DI water and put into the liquid cell, as shown in Fig.3.5(g-p).

Interestingly, cubic $NaYF_4$ nanocrystals tend to aggregate to form stable cluster with dose rate of 40 $e/Å^2s$ as shown in Fig.3.5(g-h). During the aggregation, potential oriented attachment is observed as shown in Fig.3.5(i-l). The dashed circle labeled nanocrystal comes close to the bigger nanocrystal at 11.2 s. However, it does not attach to the surface until 51.2 s after several positional adjustments. Some additional attachments are shown in Fig.3.5(m-p). The oriented attachment can be explained for anisotropic growth of hexagonal $NaYF_4$ nanostructures. The small cubic phase $NaYF_4$ nanocrystals display Brownian motion in liquid precursor, including random translations and rotational motion. As temperature increases, the higher frequency and amplitude of the Brownian motion can enhance the collision and fusion between nanocrystals. During the attachment process, the small cubic nanocrystal may keep rotating and moving until the orientation is consistent with the "mother" crystal, which could be either cubic or hexagonal structure. The hexagonal $NaYF_4$ is anisotropic structure. Due to the anisotropy, different crystal planes have different planar densities, which results in differing surface potentials. The planar density of RE^{3+} ions on (10-10) is higher than the (0001) plane, leading to more fluorine ions adsorbtion on the (10-10) surface. The fluorine adsorption can potentially reduce the nanocrystal attachment probability due to the eletrostatic force, which could possibly result in the cubic nanocrystal preferentially attaching on the hexagonal (0001) plane. With increasing synthesis time and temperature, the cubic nanocrystal will be "consumed" attaching on the hexagonal structure. However, the phase transformation process from the cubic phase to hexagonal phase still remains questions. Due to the challenge of heating solution sample in liquid cell, the highest temperature can reach is around 80^{o}C, which is much lower than the $NaYF_4$ phase transformation temperature. To investigate the high temperature effect, in-situ heating TEM experiments were conducted with a two hours hydrothermal synthesized dried $NaYF_4$ sample. The TEM grids were plasma cleaned before drop casting the $NaYF_4$ sample on the grid. Before heating, the cubic $NaYF_4$ nanocrystals are shown in Fig.3.6a. The cubic phase is confirmed with SAED pattern. With applying voltage on the TEM chip, the temperature of the nanocrystal can reach up a maximum temperature of 1000^{o}C. Notably, heating the cubic nanocrystal slightly above 300^{o}C, the nanocrystals are all changed to hollow structures, Fig.3.6b.

During the heating progress, the center of the nanocrystal is observed to have several melting regions simultaneously and then combined to a larger area. This process is different from the Kirkendall effect for two main reasons. First, the video for the heating experiment shows a phase transformation for only few seconds, which is much faster compared to the much longer Kirkendall effect. The second reason is the Kirkendall effect needs non-equilibrium atom distribution along the nanocrystal structure.

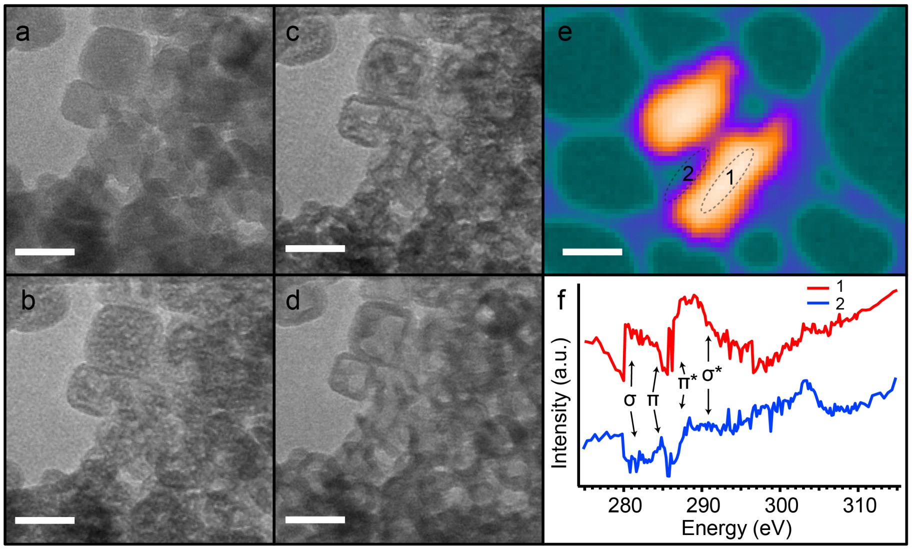

Figure 3.6: Phase transformation of $NaYF_4$ characterization. (a) In-situ heating TEM image before α-$NaYF_4$ nanocrystals phase transformation. (b-d) In-situ heating TEM image during α-$NaYF_4$ nanocrystals phase transformation. (e) STXM image of α-$NaYF_4$ nanocrystals at the carbon K edge. (f) XANES carbon K edge spectra of α-$NaYF_4$ nanocrystals at different regions.

Both the cubic and hexagonal $NaYF_4$ nanocrystals show a uniform fluorine K edge XANES mapping data, which indicates the uniform distribution of RE^{3+}, Na^+, and F^- ions within the nanocrystal without any clustering effect. This process can be explained as the nanocrystal melting and recrystallization process. As the temperature increasing, the initial melting regions in the center of nanocrystals could be caused by strain energy that is generated from crystal lattice mismatch or local impurities, such as oleate carbon ligands. To precisely determine local structure inside of the cubic $NaYF_4$ nanocrystal, near edge X-ray absorption fine structure (NEXAFS) spectroscopy was achieved from STXM at LBNL ALS beamline 5.3.2.2.

Samples for STXM analysis were prepared by drop casting a solution of β-$NaYF_4$ onto a lacy-carbon TEM grid and placing the grid in the STXM beamline under a helium atmosphere. Soft x-rays (250-800 eV) were focused onto the sample and rastered with a spot size of 31 nm using 25 nm Fresnel zone plates. The carbon K-edge XANES mapping of cubic $NaYF_4$ is shown in Fig.3.6c. The spectra of different regions within the cubic nanocrystal show a different carbon K-edge absorption. The center of the nanocrystal has higher carbon absorption compared to the edge of the nanocrystal. The carbon impurities from the center of the nanocrystal could be induced by process of nanocrystal aggregation and attachment. When nanocrystals attach to each other, the surface carbon ligand can potentially be capsulated between different grains. The STXM XANES spectra in Fig.3.6d show carbon bonds including σ, σ^*,π, and π^* which all match with the oleate carbon ligand bonding types. The edge of the nanocrystal has less carbon absorption compared to the center of the nanocrystal, which is due to the nanocrystal washing procedure after synthesis. The ligands on the surface of the nanocrystals can be sonicated off and washed away.

Chapter 4

LASER COOLING OF FLUORIDE NANOCRYSTALS IN AQUEOUS MEDIUM

4.1 Introduction

Since the first demonstration of laser cooling of solid state materials in 1995,[1] scientists and engineers have devoted a great effort to achieve a sub 100 K cryogenic temperature in vacuum.[2] However, to this day, no one has achieve laser cooling in condense phase, due to the challenges in materials synthesis and optical instrument design. With our group's specialties in materials synthesis and characterization, optical manipulation, spectroscopy, data processing and analyzing, we have first time successfully laser refrigerated Yb-doped-fluoride nanocrystal in condensed phases.[3] The potential of using singly- and co-doped YLF/$NaYF_4$ nanocrystals as a platform for precision circuit cooling, physiological refrigeration, biological imaging, and in situ ratiometric thermometry. Potential applications for these materials include precision temperature control in integrated electronic,[21, 22, 23] photonic,[24, 25] and microfluidic circuits;[26] as well as triggering and probing fundamental metabolic processes.[27, 28] In particular, the ability to measure and to modulate temperature could enable the investigation of the kinetics and temperature sensitivity of cellular processes, including ion channel actuation,[29] conformational folding dynamics of RNA,[30] and dynamic stepping motion of molecular myosin (V) motor proteins.[31]

In addition, solid state nanomaterials have been widely studied in various biomedical applications, such as therapeutic/diagnostic cancer therapy,[32, 33, 34, 35] photodynamic therapy,[36, 37, 38] bioimaging/labeling,[39] and tissue engineering.[40] Lots of efforts have been made to achieve nanomaterials used as hyperthermia reagents to increase the temperature of cancerous tissues when irradiated with NIR laser. The higher temperature can help reduce the ability of tumor cells to repair their damaged DNA which is treated by other therapies, such as chemo- or radio- therapy.[41] However, to date, no report has been published on laser refrigeration of tumors with NIR radiation. The documented cryosurgical treatments show that cryotherapy has lots of benefits including reduced morbidity, generation of antitumor immune response, less damage to surrounding structures, patient comfort and potential immunogenic advantages.[42, 43, 44, 45] With such benefits, the laser refrigeration of tumor research has huge potential application in cryotherapy. As a widely studied nanomaterial, -$NaYF_4$ nanocrystals have been proved good biocompatibility.

4.1.1 Materials consideration

The active ions in laser cooling materials require high quantum efficiency at higher energy to absorb photons from the pumping laser and re-emit them as fluorescence. RE ions match the requirements for active ions in laser cooling materials well. RE ions have small radial extent which makes the overlap between the orbitals of nearby atoms negligible.[8, 6] The optically active 4f shell in RE ions is shielded by the 5s and 6s shell, which makes the 4f electrons act like free electrons. The limited interaction with surrounding lattice of RE ions suppresses nonradiative decay leading to narrow optical transitions and high quantum efficiencies, which are the important attributes for laser cooling. Cerium and ytterbium are the two ions that have less number of 4f electronic states among all the RE ions. The electron configuration of Yb^{3+} which is one electron short of filling the 4f shell is similar to Ce^{3+} which has only one electron on 4f shell. They both produce ^2F manifold which is split into two multiplets $^2F_{7/2}$ and $^2F^{5/2}$ by spin-orbit coupling. Compared to Ce^{3+} and Yb^{3+}, the other RE ions have so many 4f electronic states inducing additional nonradiative process which can cause heating. The ideal cooling efficiency can be calculated as $\eta = (E_\mathrm{F} - E_\mathrm{P})/E_\mathrm{P}$, in which E_F is the photon energy of fluorescence light and E_P is the photon energy of pumping laser. The difference between E_F and E_P is only a few kT energy. It can be then be seen how lowering of the photon energy E_P would lead to an increase in the ideal cooling efficiency. Gd^{3+} also has less 4f electronic states, but with large energy difference.[8]

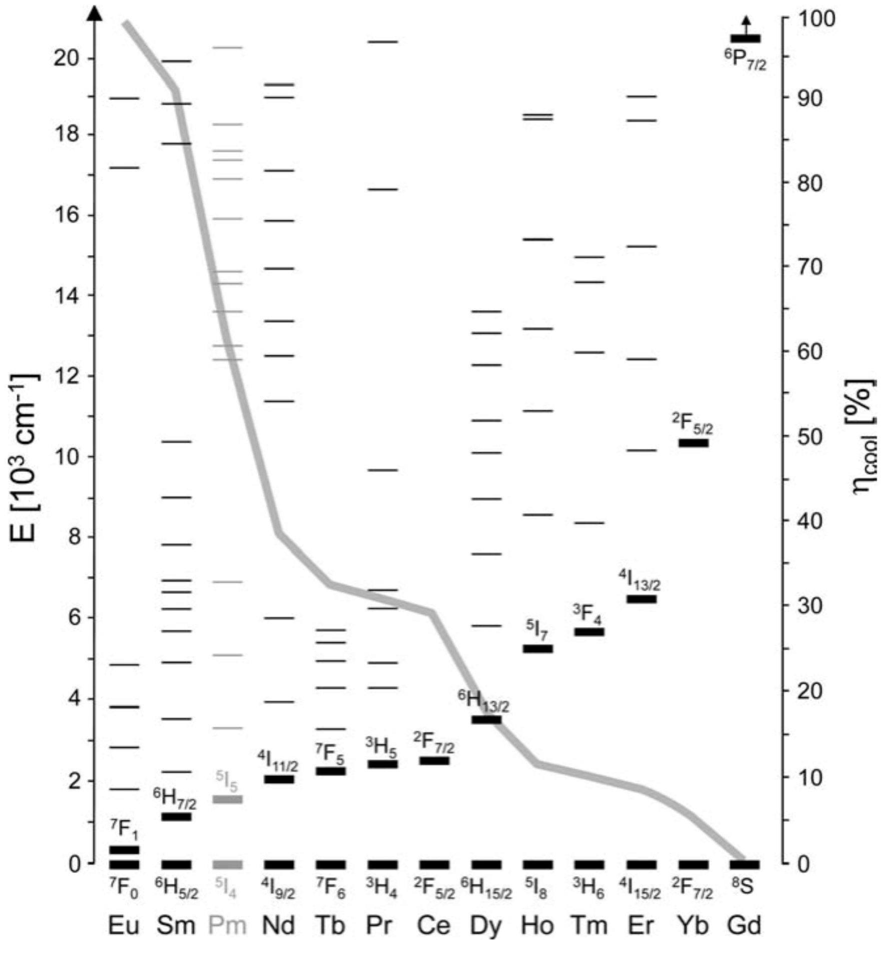

Figure 4.1: Energy levels of the trivalent rare-earth ions for energies up to 20,000 cm^{-1}. Reproduced with permission from [8]

The ideal cooling efficiency can thus be ranked as $Ce^{3+}>Yb^{3+}>Gd^{3+}$. Since the pumping wavelength of Ce^{3+} is more than 4.5 μm, it can be eliminated as a candidate due to unavailability of a compact high energy laser source of appropriate wavelength.[46] For Gd^{3+}, the pumping wavelength is in UV range, which intrinsically has low cooling efficiency. Hence, Yb^{3+} appears to be the only practical and high quantum efficiency active RE ion that can be used for laser cooling of solid state materials.

For the host materials, the primary parameter is the highest-energy optical phonon which determines the rate of multiphonon relaxation.[8] ideal host material would have a significantly lower multiphonon relaxation rate than the radiative relaxation rate at the excited state of active ions, in which the anti-Stokes photoluminescence will have the lowest number of optical phonons generated leading to a higher quantum efficiency. Another important parameter for the host materials is the purity. The impurities and defects such as foreign particles, grain boundaries and vacancies could increase the nonradiative relaxation rate, thereby lowering the quantum efficiency.[47, 48] Besides the background absorption caused by the impurities, the concentration quenching caused by active ions inside the host would also significantly affect the quantum efficiency.[8, 47, 48] Due to an increase in the concentration of active ions in the host material, the average distance between the ions would decrease and lead to interactions between ions. These ion interactions may cause energy transfer between different active ions. This energy transfer process wont cause nonradiative decay. However, this process increases probability of excitation meets impurity sites leading nonradiative decay, which causes heating. In summary, the choice of active ions and host materials including the concentration of active ions all play a crucial role in maximizing the laser cooling efficiency.

4.2 *Optical tweezers for laser cooling*

4.2.1 Optical tweezers setup

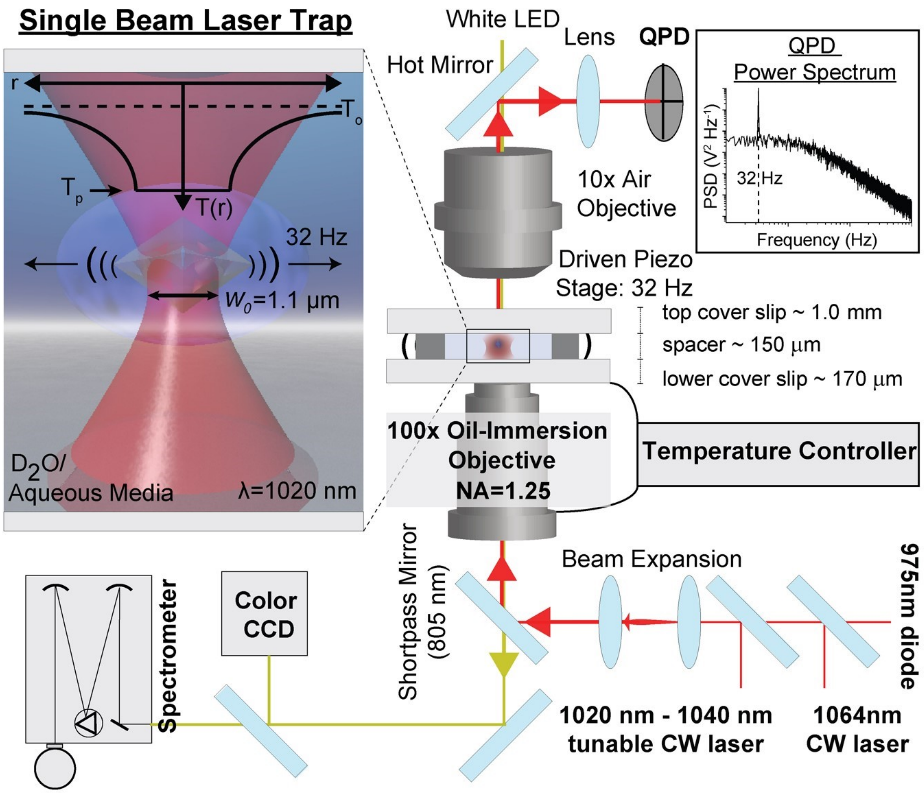

Figure 4.2: Schematic of single beam laser trapping instrument. Optically trapped $LiYF_4$ nanocrystals in D_2O chamber.[3]

Optical tweezers also called laser tweezers use a highly focused laser beam to trap dielectric nano- or micro size particles with attractive forces arising from the difference in refractive index between the aqueous solution and particles. As shown in Fig.4.2, the NIR laser is focused with 100x objective and the nanocrystal is trapped inside the aqueous solution in the glass slide chamber. The forward scattered light is focused and collected by a quadrant photodiode(QPD).[49] A white LED light placed behind the collection condenser illuminates the nanoparticles in Brownian motion which can be observed live through the color CCD camera.

The laser tweezer setup is a modified modular optical tweezer kit (Thorlabs, OTKB), where the original condenser lens has been replaced with a 10x Mitutoyo condenser (Plan Apo infinity-corrected long WD objective, Stock No. 46-144). The 100x objective focusing lens has a numerical aperture of 1.25 and a focal spot of 1.1 μm. The quadrant photodiode and piezostage were interfaced to the computer through a DAQ card (PCIe-6361 X Series, National Instruments) and controlled through modified MATLAB software (Thorlabs). Experimental chambers were prepared as followed. Several microliters of the nanocrystal/aqueous medium dispersion was transferred by a pipette into a chamber consisting of a glass slide and glass coverslip. The edges of the glass slide and the glass coverslip were then sealed with a 150-μm-thick adhesive spacer (SecureSeal Imaging Spacer, Grace Bio-labs). Nanocrystals were trapped at the center (75 μm from the surface) of the temperature controlled perfusion chamber (RC-31, Warner Instruments) and held at $T_0 = 25$ ^{o}C while voltage traces were recorded using the QPD for 3 seconds at a sample rate of 100 kHz. The QPD voltage signal was calibrated by oscillating the piezostage at 32 Hz and an amplitude of 150 nm peak-to-peak during signal acquisition, as outlined in reference[50].

Since the beam is focused by high NA objective, there is a gradient of electric field and the field is strongest at the beam waist. Due to light scattering and Lorentz force, the nanoparticle is trapped in the beam waist, which is the narrowest point of the focused beam. The photothermal cooling experiment is conducted through a customized single beam laser trap system shown in Fig.4.2. The nanoparticles are suspended in aqueous solution through sonication and undergo Brownian motion. The NIR laser beam scatters off the trapped particles and creates dynamics interference pattern on the QPD. Then the photovoltage signal from the detector can be processed with Fourier transform to power spectra density (PSD), which can be further processed to achieve the local surrounding aqueous solution temperature of the trapped particle.[37]

4.2.2 Cold Brownian motion temperature measurement

Power spectra from the QPD voltage traces were processed according to Berg-Sorensen and Flyvbjerg[51] and used to calibrate the QPD traces following the method of ref[50]. An experimental diffusion coefficient was then extracted by fitting the characteristic function for the experimental power spectra derived in Berg-Sorensen and Flyvbjerg.[51] Given that the temperature of the trapped particle is significantly different than the temperature sufficiently far from the laser focus, the particle-trap system is not isothermal and behaves according to nonequilibrium dynamics. Thus, equating the experimental diffusion coefficient to nonisothermal Brownian dynamics necessitates the application of cold Brownian motion (CBM), as derived by Chakraborty et al.[52] The CBM diffusion coefficient is then related to the CBM temperature by:

$$D_{\mathrm{CBM}} = \frac{k_{\mathrm{b}} T_{\mathrm{CBM}}}{\gamma_{\mathrm{CBM(T)}}} \tag{4.1}$$

where $\mathrm{D}_{\mathrm{CBM}}$ is the CBM diffusion coefficient, kb is Boltzmanns constant, $\mathrm{T}_{\mathrm{CBM}}$ is the CBM temperature, and $\gamma_{\mathrm{CBM(T)}}$ is the CBM Stokes drag. To the leading order of the temperature increment or decrement Δ T = (T_{p} - T_0), the temperature-dependence of the viscosity on $\mathrm{T}_{\mathrm{CBM}}$ can be neglected, giving the effective temperature[52]

$$T_{\mathrm{CBM}} = T_0 + \frac{5}{12}\Delta T \tag{4.2}$$

To account for the solvent viscosity temperature dependence, we follow the methods of Reference[53] and use the Vogel-Fulcher-Tammann-Hesse (VF) law with the viscosity functional form $\eta(\mathrm{T})=\eta_\infty\exp[\mathrm{A}/((\mathrm{T}-\mathrm{T}_{\mathrm{VF}}))]$, the CBM Stokes drag is given by

$$\gamma_{\mathrm{CBM(T)}} = 6\pi R\eta_{\mathrm{CBM(T)}} \tag{4.3}$$

where R is the particle radius, and $\eta_{\mathrm{CBM(T)}}$ is the temperature-dependent CBM viscosity that is related to the viscosity of the solvent at room temperature,η_0, by

$$\frac{\eta_0}{\eta_{\mathrm{CBM(T)}}} \approx 1+\frac{103}{486}[ln(\frac{\eta_0}{\eta_\infty})][\frac{\Delta T}{(T_0-T_{\mathrm{VF}})}]-[\frac{56}{243}ln(\frac{\eta_0}{\eta_\infty})-\frac{12563}{118098}ln^2(\frac{\eta_0}{\eta_\infty})][\frac{\Delta T}{(T_0-T_{\mathrm{VF}})}]^2 \tag{4.4}$$

Equations 4.2,4.3,4.4 are then used in Eq.4.1 to obtain DCBM, which is subsequently compared to the experimental diffusion coefficient to determine the particle temperature Tp (excluding the temperature discontinuity at the particles surface from the Kapitza resistance[54]). An alternative CBM temperature analysis using a semi-phenomenological expression for DCBM that approximately accounts for higher order terms in ΔT yields consistent results, indicating that these higher order corrections are negligible, for our purposes. For the experiments reported here, the VF viscosity parameters were fit to experimental data and are as follows:

D_2O, η_{∞}=3.456 x 10^{-5} Pa · s

A = 478.6 K

T_{VF} = 160 K,

and

DI water, PBS, DMEM

η_∞=2.664 x 10^{-5} Pa · s

A = 536.5 K

TVF = 145.5 K. VFT viscosity parameters for DI water, PBS (0.01 M, pH 7.4;

Sigma P5368), and DMEM (1X, high glucose, pyruvate; Life Technologies Cat. 11995-065) were assumed to be equivalent since it has been reported that water viscosity can be used for purposes of modeling particle transport in non-serum containing media.[55]

4.2.3 Temperature extraction error analysis

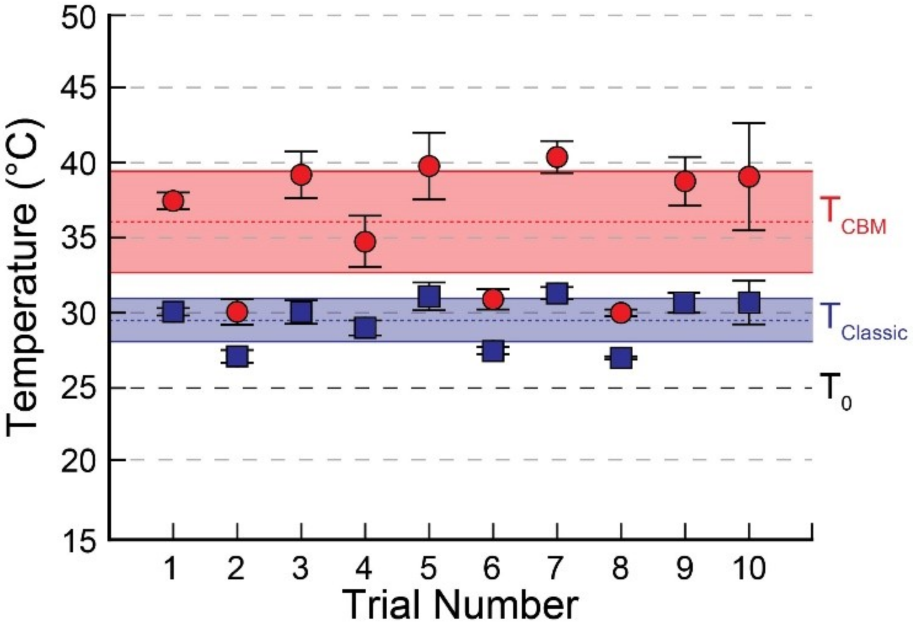

Figure 4.3: Laser trap temperature extraction error analysis. A 1.01 μm diameter silica sphere trapped in D_2O using a trapping wavelength of 975 nm in a temperature controlled chamber held at $T_0 = 25$ ^{o}C. QPD data was acquired 10 consecutive times at an irradiance of 5.9 MW/cm^2 and the temperature of the sphere was determined using (red circles, TCBM) the cold/hot Brownian temperature extraction method detailed in section A, and (blue squares, TClassic) the classical isothermal assumption method. The error bars represent the standard deviation.[3]

In order to determine the accuracy of the temperature extraction method presented here, silica beads (SS04N/9857, Bangs Laboratories) are used for their monodisperse size distribution (1010 nm diameter) and their known capacity to heat minimally when trapped with a near-infrared (NIR) laser trap.[56] The same experiment that was performed on YLF particles in this study was performed on the silica beads in D_2O using a trapping wavelength of 975 nm and an irradiance of 5.9 MW/cm^2. For this experiment, a temperature controlled chamber was used (RC-31, Warner Instruments), with the chamber held at $T_0 = 25$ ^{o}C while the same bead was trapped and QPD data acquired 10 consecutive times. The cold Brownian analysis above was then applied to the resulting QPD signals, and the temperature results are shown in red circles in Fig.4.3. The average calculated particle temperature (red dashed line) is TCBM = 35.9 ^{o}C with a standard deviation (red shaded area) of ±6.8 ^{o}C. For comparison, the same data was also analyzed with the method assuming isothermal conditions, and the temperature results are shown in blue squares in Fig.4.3. The average calculated particle temperature (blue dashed line) is $T_{\text{Classic}} = 29.5$ ^{o}C with a standard deviation (blue shaded area) of ±2.8 ^{o}C. The result suggests that the temperature calculated by cold Brownian analysis is obviously different than the classic analysis.

4.3 Laser cooling of $LiYF_4$ nanocrystals

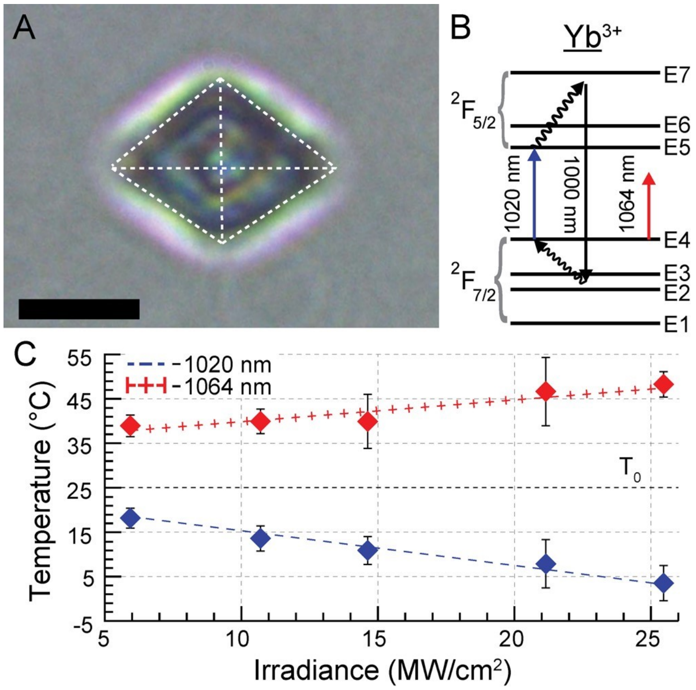

Figure 4.4: Laser refrigeration of optically trapped YLF microcrystals. (A) Optical micrograph of an optically trapped YLF crystal; scale bar = 3 μm. (B) Crystal field energy level configuration of Yb^{3+} dopant ions and employed cooling scheme. (C) Extracted temperature (Tp) of optically trapped particles in D_2O as determined using the outlined CBM analysis. Yb^{3+}-doped YLF particles are shown to cool when trapping wavelength is resonant with the E4-E5 transition (= 1020 nm) but heat when the trapping wavelength is below the transition (= 1064 nm).[3]

Trapping data was acquired using a diode-pumped solid state Yb^{3+}:YAG thin-disk tunable laser (VersaDisk 1030-10, Sahajanand Laser Technologies) at a wavelength of 1020 nm, a 975 nm pigtailed Fiber Bragg Grating (FBG) stabilized single-mode laser diode (PL980P330J, Thorlabs), as well as a solid-state Nd^{3+}:YAG 1064 nm (BL-106C, Spectra-Physics) at different irradiances at MW/cm^2. Magnitudes of cold Brownian temperature changes presented were determined using methods outlined in reference.[49] Silica beads (SS04N/9857, Bangs Laboratories) were used for their monodisperse size distribution (1010 nm diameter), and they have shown to minimally heat when trapped with a laser tweezer at NIR wavelengths.[56] Electromagnetic simulations of the interaction of the trapping laser with a YLF TTB were also performed to predict the stable trapping configurations of optically trapped YLF particles. Each YLF cooling data point in Fig.4.4 in the manuscript represents an average of 6 individual particles with an average radius of 764 nm with a standard deviation of 293 nm. Discrete Dipole Approximation software DDSCAT 7.367 was used to simulate laser trap interactions with ideal (nontruncated) YLF tetragonal bipyramids in water. For a bipyramid of length of 7.6 μm and base of 3.9 μm (Fig.4.5B), a dipole density of 2267 dipoles/μm^3 (85,901 dipoles/octahedron) was used. At 1020 nm, refractive indices of YLF and water are 1.44831 and 1.327, respectively. Although YLF is a birefringent crystal, this has been ignored in the simulation based on the small birefringence (0.02), which will only be reduced by the lattice mismatch of the many domains within a single octahedron. Also, the approximation of a laser trap by a plane wave becomes less appropriate as the size of the particle relative to the beam spot gets large. By varying , , and β (see Fig.4.5A) and calculating the radiation pressure and torque we are able to predict the optimal orientation for trapped particles since we assume the particle will orient so as to minimize these forces and maximize the trapping potential. One intriguing result of the simulations is the particle size dependence of orientation. For example, a tetragonal bipyramid with a length of 7.6 μm is expected to align with the long axis perpendicular to both k and E, or θ=90^o, ϕ=90^o, and β=0^o (Fig.4.5C/D), whereas a similar particle with a length of 200 nm is predicted to align its long axis to be parallel with the direction of propagation (Fig.4.5E/F). It is also notable that the particle is able to generate significant internal and near fields as demonstrated in Fig.4.5B.

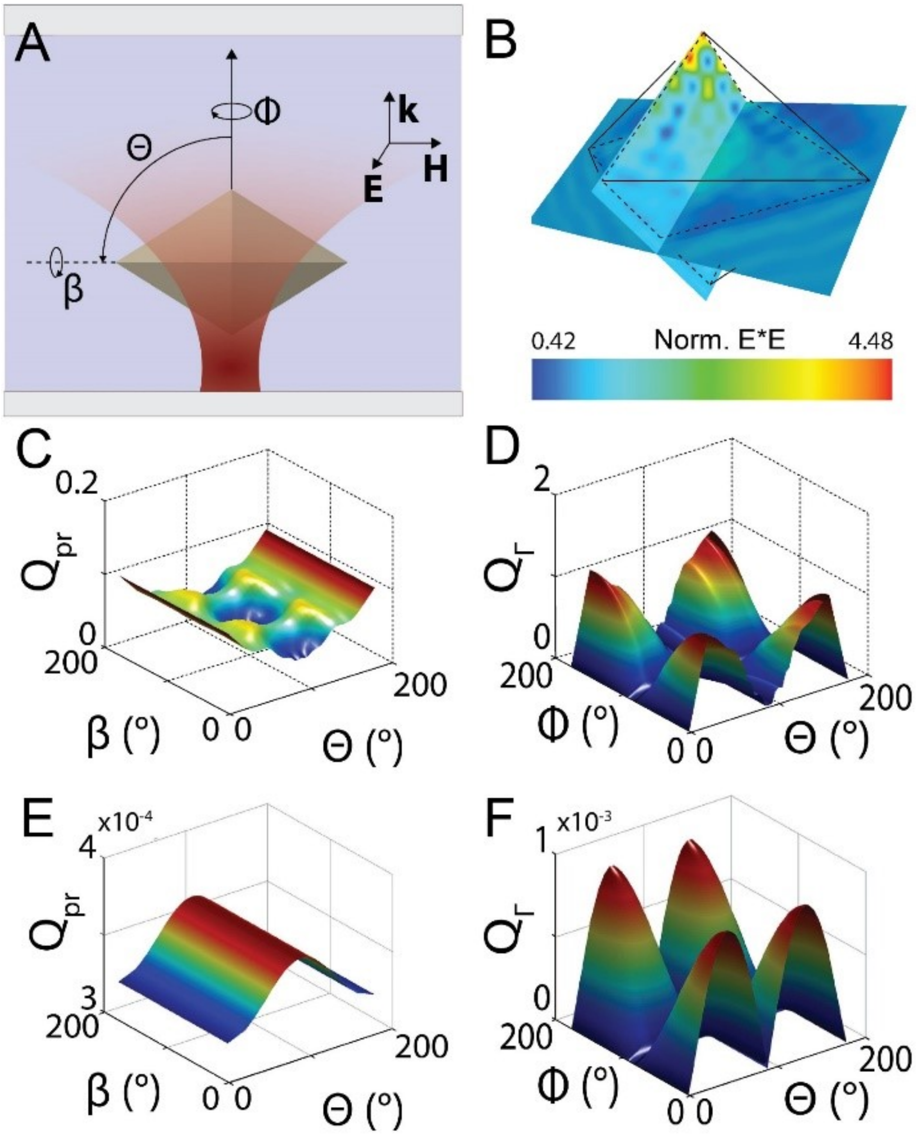

Figure 4.5: Stable trapping configuration simulations. (A) Optically-trapped YLF particle in an aqueous fluid chamber. Angles are used to describe numerical discrete dipole approximation calculations in panels C-F. (B) Cross sectional plot of the internal electric field magnitude within a YLF particle with dimensions 7.6 μm and 3.9 μm at a trapping wavelength of 1020 nm. (C) Radiation pressure on a YLF particle shown in B. (D) Torque calculations as a function of angular coordinates for the YLF particle shown in B. (E) Radiation pressure on a 200 nm long YLF. (F) Torque calculations as a function of angular coordinates for a 200 nm long YLF particle.[3]

4.4 Laser cooling of $NaYF_4$ nanocrystals

Two NIR laser sources (λ = 975 nm and 1,064 nm) were integrated within the laser trapping instrument in order to determine how the optical traps NIR wavelength influences the temperature of β-$NaYF_4$ NWs. The dependence of heating on the Yb^{3+}-dopant concentration and pumping wavelength is shown in Fig. 4.6e, where β-$NaYF_4$ NWs are irradiated by two different pumping lasers (975 nm and 1,064 nm). The average temperature of ten NWs is observed to rise from 33^oC to 46^oC when the Yb^{3+} dopant-concentration changes from 0% to 10%, respectively, using an optical trap with a fixed laser wavelength of $\lambda = 975$ nm and a constant irradiance of 6 MW/cm^2. Laser heating is observed to depend on the concentration of Yb^{3+} dopants, with an increase in local heating with elevated Yb^{3+} doping concentration. When λ = 975 nm the photon energy (1.27 eV) is sufficient to excite electrons from the E1 crystal-field state to E5 state followed by both radiative and non-radiative relaxation, leading to an increase in local solvent heating with increasing Yb^{3+} concentration. The same β-$NaYF_4$ NWs (with 0% and 10% Yb^{3+} doping) were used for control Brownian-thermometry experiments using a wavelength of λ = 1,064 nm. In these controls, the temperature for each both 0% and 10% doping was observed to remain at a temperature of 42^oC at an irradiance of 25 MW/cm^2. In contrast to experiments with λ = 975 nm, when λ = 1064 nm the photon energy (1.16 eV) is energetically insufficient to pump the E4 to E5 resonance and heating is not observed to depend on the concentration of Yb^{3+} dopant ions.

Single-particle laser-trapping experiments are also able to provide information on local mass-transport processes occurring at the solid / electrolyte interface. Recently, cation-exchange reactions have been shown to occur reversibly in ionic nanostructures at room temperature, which can be used to create complex shapes and compositions of nanocrystals.[57, 58]

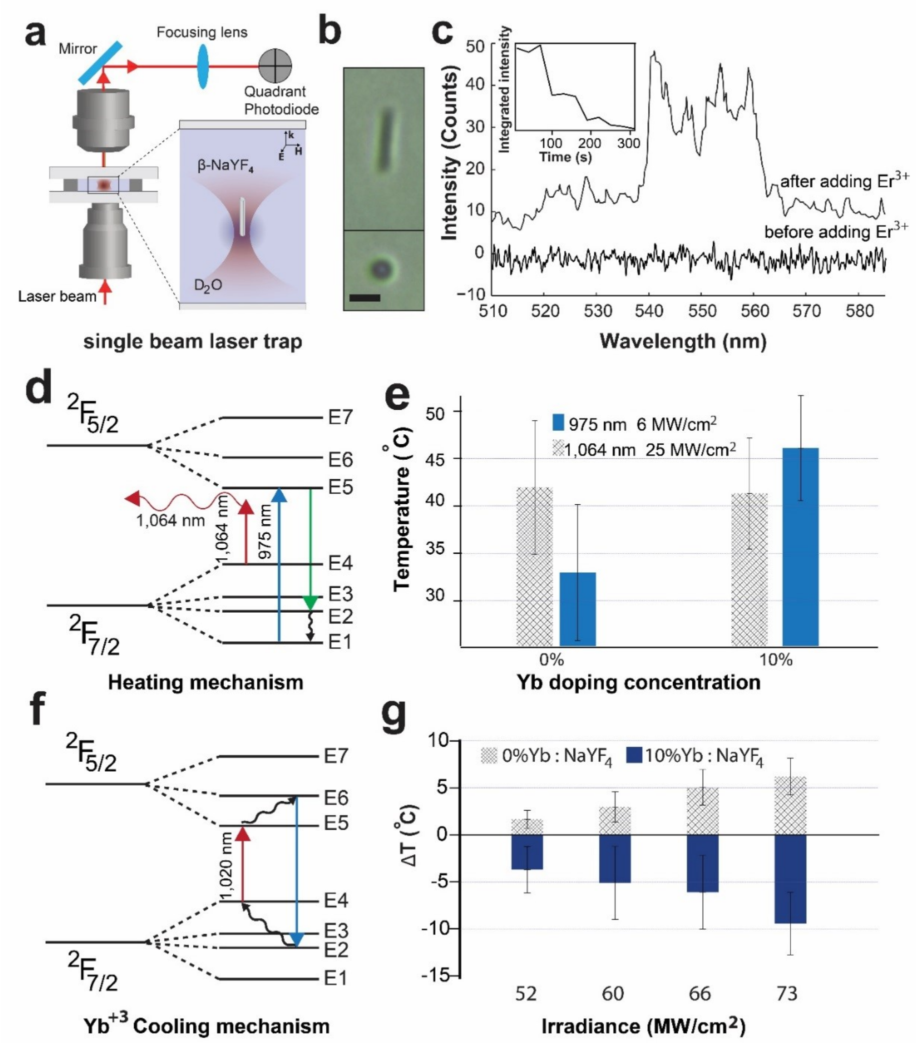

Figure 4.6: Laser heating/cooling of single β-NaYF$_4$ nanowire in D$_2$O. (a) Optically-trapped β-NaYF$_4$ nanowire in an aqueous fluid chamber. (b) Top: Optical micrograph of single β-NaYF$_4$ nanowire before trapping. Bottom: Single β-NaYF$_4$ nanowire trapped in D$_2$O, scale bar = 1 μm. (c) Photoluminescence from single trapped β-NaYF$_4$: 10%Yb nanowire in D$_2$O before and after doping Er^{3+} ions showing cation exchange, inset: integrated PL intensity versus time plot from a trapped Er^{3+} doped β-NaYF$_4$ nanowires shows a decreasing trend. (d) Crystal field energy level configuration of Yb^{3+} dopant ions in β-NaYF$_4$ hexagonal structure which shows the heating mechanism with different laser wavelengths. (e) Temperature of single trapped β-NaYF$_4$ nanowire with different Yb^{3+} dopant concentrations under both 975 nm and 1,064 nm laser irradiance (f) Diagram of the anti-Stokes laser refrigeration process. (g) Temperature change of individually trapped β-NaYF$_4$ nanowires with different Yb^{3+} dopant concentrations under increasing 1,020 nm laser irradiance. Error bars are based on standard deviation of ten samples.[10]

In addition, the Er^{3+} fluorescence can be used as a sensitive probe of surface states where excited ions may relax non-radiatively and cause heating.

In Fig.4.6c the photoluminescence of Er^{3+} ions is tracked to monitor ion-exchange between the surface of β-$NaYF_4$ NWs and the surrounding electrolyte solution. First, β-$NaYF_4$: 10%Yb_{3+} NWs were suspended in Er^{3+} nitrate solution for 24 hours to let Er^{3+} ions exchange and diffuse into the surface of individual NWs. The particles were then washed to remove excess Er^{3+} ions and resuspended in D_2O. The loss of Er^{3+} cations through diffusion at the solid-liquid interface was observed by measuring the gradual decay of visible photoluminescence from a single β-$NaYF_4$: 10%Yb^{3+} NW irradiated with a 975 nm laser (Fig.4.6c, inset). In comparison, β-$NaYF_4$:10% Yb^{3+} NWs showed no photoluminescence when trapped at the same conditions described above (Fig.4.6c). Photoluminescence lifetime measurements of β-$NaYF_4$:10% Yb^{3+} / 1% Er^{3+} NWs in vacuum were made using the experimental configuration shown Fig.5.2. The lifetime of the Er^{3+} $^4S_{3/2}$ state is measured to be (221 ± 6) μs at 300 K using a laser wavelength of 975 nm and an irradiance of 5.3 W/cm^2 which matches recently reported literature values.[59]

The same instrument was used to conduct laser cooling experiments with β-$NaYF_4$: 10%Yb^{3+} NWs. These NWs were observed to refrigerate by 9C below ambient temperatures when trapped at a wavelength of 1,020 nm, resonant with Yb^{3+} ions, at an irradiance of 73 MW/cm^2. The low-entropy laser excites electrons within Yb^{3+} ions from their E4 crystal-field level to their E5 level. The long (ms) excited-state lifetimes of Yb^{3+} excited states allow them to absorb optical-phonons from the host crystal lattice, followed by spontaneous anti-Stokes fluorescence (with a higher mean photon energy compared to the absorbed photons) that ultimately removes heat from the lattice and cools both the crystal and its immediate surroundings. As a control, β-$NaYF_4$: 0%Yb^{3+} NWs trapped under identical conditions (73

MW/cm^2 with λ = 1,020 nm) show heating by 6 ^{o}C above the ambient temperature (Fig. 4.6g). Without the Yb^{3+} ions, defects and impurities (including hydroxyl ions, capping ligands, etc.) can participate as non-radiative channels during multi-phonon relaxation processes that ultimately act to increase the surrounding fluids temperature. Large laser irradiance values are required to enable the optical trapping and photothermal characterization of single nanowires. The laser irradiance used here is above the saturation irradiance (127 kW/cm^2) recently reported for Yb^{3+} ions in bulk yttrium-lithium-fluoride single crystals,[60] and may reduce the migration of energy through Yb^{3+} ions to non-radiative nanocrystal surface-states.

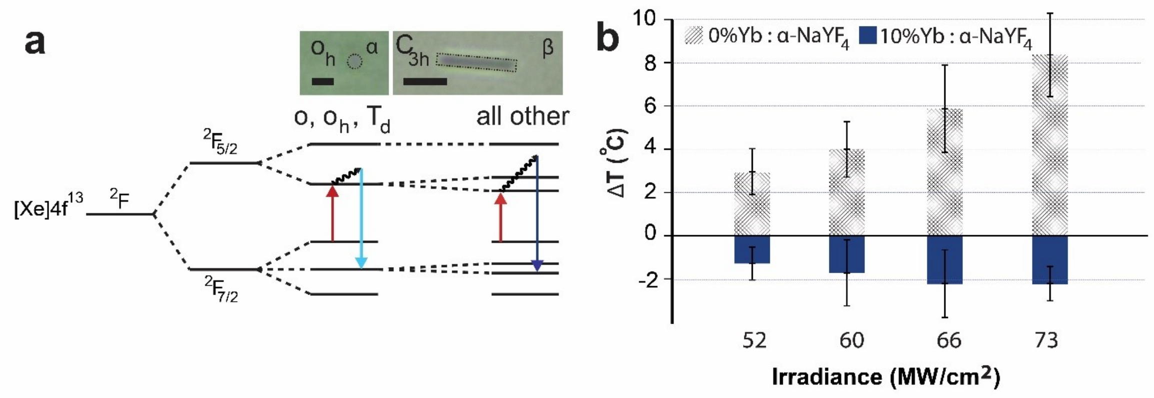

Figure 4.7: Laser refrigeration of cubic α-NaYF$_4$ nanocrystals. (a) Crystal field energy level configuration of Yb^{3+} dopant ions in α-NaYF$_4$ cubic structure and β-NaYF$_4$ hexagonal structure. Inset: optical micrograph of optically trapped α-NaYF$_4$ nanocrystal with Oh cation point group symmetry and β-NaYF^4 NW with C3h cation point-group symmetry. α-NaYF$_4$ scale bar = 300 nm, β-NaYF$_4$ scale bar = 1 μm(b) Temperature change of individually trapped cubic α-NaYF$_4$ nanocrystals with different Yb^{3+} dopant concentrations under increasing 1,020 nm laser irradiance. Error bars are based on standard deviation of ten samples.[10]

Similar experiments have been conducted on cubic α-NaYF$_4$ nanocrystals, where Fig. 2.3 shows their representative crystal structure and morphology observed through

TEM. Relative to hexagonal β-NaYF$_4$ nanowires, the cubic α-NaYF$_4$:10%Yb^{3+} nanocrystal is observed to cool by 2 ^{o}C below ambient conditions (Fig. 4.7b) at an identical laser trapping irradiance. This may be due to a larger crystal field splitting in the high-symmetry cubic α-NaYF$_4$: 10%Yb^{3+} crystal structure relative to the smaller crystal field splitting in the low symmetry hexagonal β-NaYF$_4$: 10%Yb^{3+} structure, which is shown in Fig.4.7a. For the initial state of the pumped transition, a smaller crystal field splitting can provide a higher thermal population, which gives a higher pump absorption coefficient and, consequently, higher laser cooling power.[9] Additionally, the higher surface to volume ratio of α-NaYF$_4$ compared to β-NaYF$_4$ will introduce more surface states, which may cause more nonradiative heat dissipation. Compared to bulk materials, the fluorescence reabsorption in nanocrystals is negligible.[61] The laser heating and cooling effect can be tuned by changing the pumping laser wavelength (Fig. 4.6e,g), with potential applications in single molecule biophysics.[31]

The size of individual nanocrystals has also recently been shown to affect the overall efficiency of their photoluminescence when pumped at a fixed laser wavelength.[62] Modeling the internal optical field distribution within β-NaYF$_4$ NWs is important for understanding how a NWs size affects the absorption of incident electromagnetic radiation. Although numerous studies of light scattering and electromagnetic energy absorption of cylindrical nanostructures have been reported, there have been fewer studies of hexagonal wires.

In Fig. 4.8 we plot results from finite element simulations of the internal optical fields within hexagonal β-NaYF$_4$ NWs using normalized units $((\mathrm{E}_1 \cdot E_1{}^*)/E_0{}^2)$, where E_1 is the internal field, $E_1{}^*$ is its complex conjugate, and E_0 is the electric field amplitude of the incident plane-wave. Morphology dependent resonances (MDRs) are observed to exist within β-NaYF$_4$ NWs for an incident wavelength with λ = 1,020 nm. The localization of resonant modes within the NW can enhance the absorption of laser radiation.[63, 64] Fig.4.8a shows the internal electric field 2D simulation of cross-section of the NW under certain excitation. The average normalized electric field is plotted with different sizes of the edge lengths. With tuning the width the NW's cross-section, the internal electric field can be tuned to maximize, which suggests maximization of the absorption of excitation. Similarly, in Fig.4.8c, with fixing the edge length of cross-section of the NW at 255 nm, the maximum internal electric field of the 3D NW is plotted with different lengths of the NW. Fig.4.8b shows the 3D electric field plot of the NW with edge length of 255 nm and height of 2,000 nm.

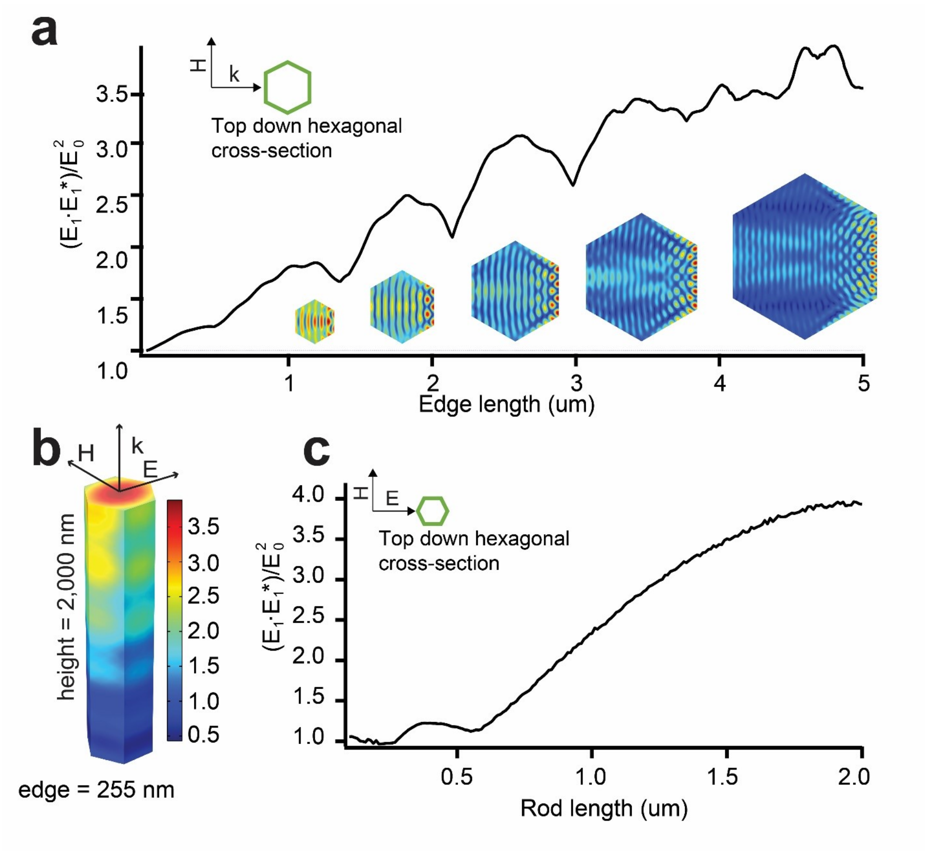

Figure 4.8: Comparison of calculated values for the normalized electromagnetic source term $(\mathrm{E}_1 \cdot E_1{}^*)/E_0{}^2$ for β-NaYF$_4$ nanowires in water with 1,020 nm laser wavelength. (a) Plot of the calculated maximum source term values for β-NaYF$_4$ nanowires with laser incidence perpendicular to the edge as a function of the hexagonal edge length ranging from 10 nm to 5,000 nm. (b) Example 3D plot of β-NaYF$_4$ nanowire electric field. Color bar shows the amplitude of the normalized electric field. (c) Plot of the calculated maximum source term values for a β-NaYF$_4$ nanowire with the laser incident on the bottom facet as a function of the wire length ranging from 100 nm to 2,000 nm. The edge length of the nanowire is kept constant at 255 nm.[10]

This field enhancement may compensate for the drawback of small optical interaction lengths in nanocrystalline materials, assuming the external radiative quantum efficiency of anti-Stokes cooling photons is not reduced. In the future, hydrothermal synthesis can be used to synthesize β-NaYF$_4$ NWs with different sizes and shapes in order to achieve a higher cooling efficiency by matching the pumping laser wavelength to an internal cavity resonance within the NW. Therefore, the cooling efficiency can be adjusted by changing not only the crystalline host matrix for rare-earth ions but also the nanostructures size and morphology.

Chapter 5

UPCONVERSION FLUORESCENCE THERMOMETRY

5.1 Introduction

Rare-earth-doped upconversion nanoparticles are widely suited to a range of applications including displays,[65, 66, 67] solar cells,[68, 69, 70, 71] bio-imaging,[72, 73, 74, 75, 76] bio-labeling,[77, 39] biosensing,[78, 79, 80] drug delivery,[81, 82, 83] theranostics,[84] nano-thermometry,[85, 28, 86, 87] photodynamic therapy,[88, 89, 90, 91] and others.[92, 93] These nanoparticles can be excited with near-infrared (NIR) radiation, which is transparent window for biological tissue, and emit bright, visible fluorescence.[94, 87, 91, 95, 96] As a major challenge in conventional fluorescence imaging and labeling, UV or visible excitation can cause autofluorescence, which can be solved by upconversion with NIR excitation. Among upconversion nanoparticles, $NaYF_4$ nanocrystals have been intensely studied as the most efficient upconversion nanocrystals with biocompatibility, low-toxicity, and non-blinking, photostable properties.[95, 96, 97, 98] They are bright enough to use confocal microscopy to observe a single nanocrystal with size of 12.9 nm for super-resolution imaging.[99] In addition to a good upconversion host material, $NaYF_4$ has been theoretically proven to be an efficient host material for laser cooling with anti-Stokes fluorescence emission, which is also demonstrated experimentally in optical tweezers.[10, 3] To improve upconversion performance, significant effort has been devoted to improve the quantum efficiency

$$\eta = \frac{k_r}{k_r + k_{nr}} \tag{5.1}$$

where k_r is the radiative decay rate, k_{nr} is the nonradiative decay rate. There are various approaches to modify the radiative and nonradiative decay rate. As the size of a UCNP decreases, the lifetime shortens due to the nonradiative decay caused by surface defects.[100, 101, 102] Surface modification with changing ligand and/or coating inorganic shell can help reduce the surface defects and isolate them from emission quencher to increase the luminescence.[103, 104, 105, 106, 107] Changing the host material's crystal lattice with different point group symmetry can change the dopant ions' local crystal field, which affects the PL.[108, 109] Tuning the dopant level in a UCNP can prevent from concentration quenching as well as tune PL wavelengths.[110, 111, 112, 113, 114] In addition to the intrinsic factors, environmental factors including electric field,[115, 116, 117, 118] magnetic field,[119, 120, 121, 122, 123] pressure,[124] temperature,[94, 87, 125, 86] solvent solution,[126, 127, 128] and others can also affect the radiative and nonradiative decay rate. To characterize the UCNP optical properties, one common way is to prepare the sample on a glass substrate.[127, 96, 92, 129, 130, 131] Recently we found that the total decay rate of Er^{3+} $^4S_{3/2}$ state of single β-$NaYF_4$:20%Yb^{3+}/2%Er^{3+} nanowires on a substrate is much higher relative to the decay rate of the same NW far away from substrate. The total decay rate is the inverse of the lifetime, which can be achieved by fitting the fluorescence intensity decay profile. It has been reported that the lifetime of nanodiamond nitrogen vacancy (NV) centers in silica aerogel has a significant increase compared with the NV centers on the plane substrate, where the radiative decay rate is influenced by electromagnetic local density of states (LDOS).[132, 133] Both semi-analytical theory and finite-difference time-domain (FDTD) results have been predicted that emission rate for radiating dipoles increases with reaching to a plane interface between two dielectrics, especially in the sub-100nm distance range.[132, 133, 134] Similar experimental and simulation studies have been reported on single ions,[135, 136] single dye molecules,[137, 138] thin films,[139, 140] and rare-earth-doped glass near a substrate.[141] To further investigate the substrate effect on the lifetime of the single NW level, we utilize optical tweezers to manipulate and position the same β-NaYF$_4$:20%Yb^{3+}/2%Er^{3+} NW at different distances from the substrate without changing the local environment. Under such condition, all the variables for affecting the Er^{3+} ^{4}S$_{3/2}$ state lifetime can be ruled out,[142, 143] except the trapping distance. The Er^{3+} ^{4}S$_{3/2}$ state lifetime is increasing by a factor of 1.62±0.01 as trapping distance increased from ∼0nm to a distance where is considered as no substrate effect. The Er^{3+} ^{4}S$_{3/2}$ state lifetime of a single β-NaYF$_4$:20%Yb^{3+}/2%Er^{3+} NW has also been studied as a function of temperature. We can manipulate individual β-NaYF$_4$:20%Yb^{3+}/2%Er^{3+} NW with optical tweezers and locally probe temperature field in the nanoscale range. In addition to the fundamental interest of physics, this work provides a realistic avenue for the development of UCNP probes to measure LDOS and temperature in complex nano/microstructured system, which can be potentially applied for sensing chemical and biological process, and developing a range of photonic devices. Besides single NW study, we have made β-NaYF$_4$:20%Yb^{3+}/2%Er^{3+} embedded polydimenthylsiloxane(PDMS) composite for potential microfluidic chamber with temperature probe and control functions.

5.2 Single nanoparticle thermometry

5.2.1 Synthesis and lifetime measurement

A low cost, scalable hydrothermal synthesis approach is used to prepare β-NaYF$_4$ NWs that exhibit a hexagonal crystal structure as shown in Fig.5.1a. Scanning electron microscopy (SEM) was used to measure the size and morphology of the as synthesized NWs which are shown in Fig.5.1b. Dark field transmission electron microscopy (TEM) was used to measure single NW's diameter and size. The phase composition of the NWs has been confirmed by X-ray diffraction (XRD). All the XRD peaks are matching with standard β-NaYF$_4$ phase peaks.

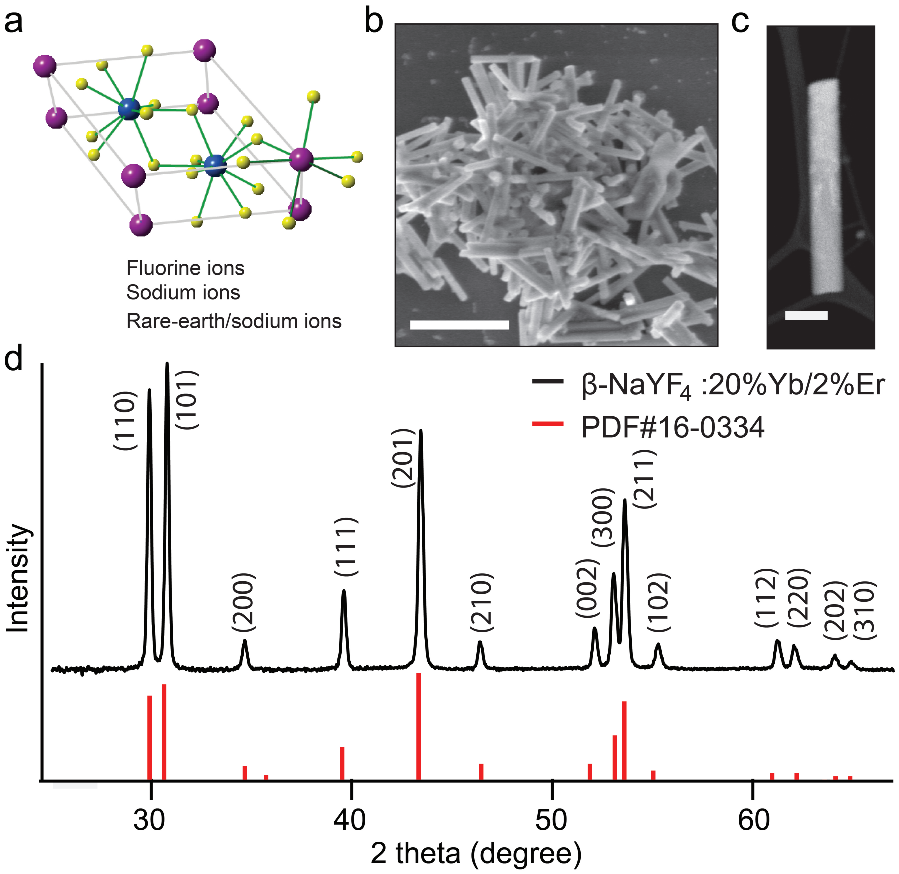

Figure 5.1: Synthesis and characterization of NaYF$_4$ nanowires. a) Schematic of hexagonal crystal structure of β-NaYF$_4$ with P6$_3$/m group symmetry. b)SEM image of β-NaYF$_4$:20%Yb^{3+}/2%Er^{3+} nanowires; scale bar = 2 μm. c) Dark field TEM image of β-NaYF$_4$:20%Yb^{3+}/2%Er^{3+} nanowires; scale bar = 200 nm d) X-ray diffraction of ensemble β-NaYF$_4$:20%Yb^{3+}/2%Er^{3+} nanowires confirming the hexagonal phase structure.

A home-built single-beam NIR optical trapping instrument, as shown in Fig.5.2a, is used to perform single NW optical trapping experiments. A schematic graph for a characteristic, optically-trapped NW is shown in Fig.5.2a inset. A 975 nm diode

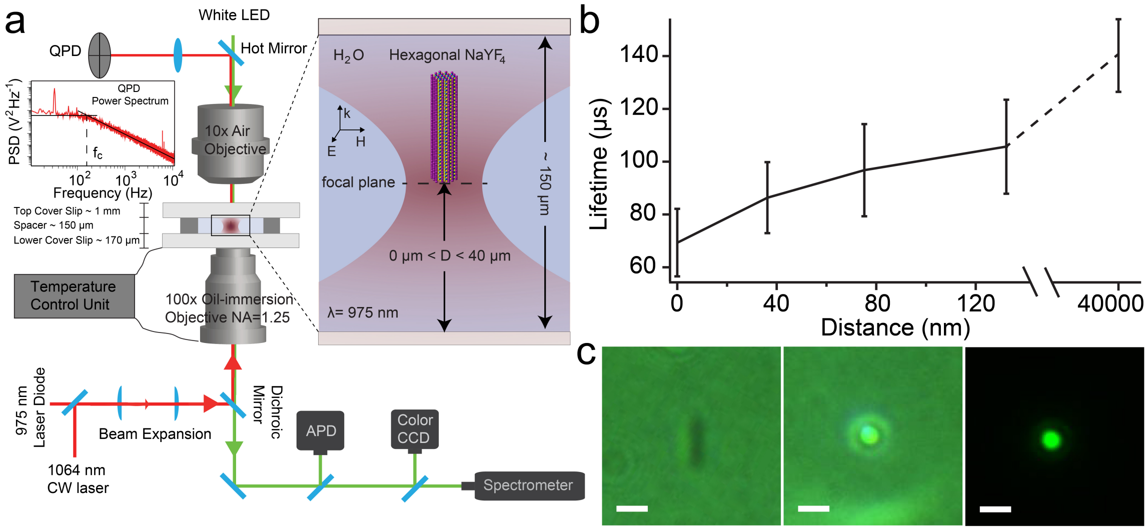

Figure 5.2: Schematic of laser trapping instrument with single particle lifetime and fluorescence measurement capabilities. (a) An optically trapped β-NaYF$_4$:20%Yb^{3+}/2%Er^{3+} NW in aqueous fluid chamber. (b) Er^{3+} $^4S_{3/2}$ state lifetime of an optically-trapped β-NaYF$_4$:20%Yb^{3+}/2%Er^{3+} NW in water at various distances from quartz surface. (c) Left: bright field image of β-NaYF$_4$:20%Yb^{3+}/2%Er^{3+} NW in Brownian motion, scale bar = 1 μm; Middle: Bright field image of optically-trapped β-NaYF$_4$:20%Yb^{3+}/2%Er^{3+} NW with 975 nm laser; Right: Image of optically-trapped β-NaYF$_4$:20%Yb^{3+}/2%Er^{3+} NW without illumination source showing strong green emission.

laser is focused by a 100x oil-immersion objective lens down to a diffraction limit with spot size of 1.1 μm. The gradient optical force can trap a single NW in the focus spot, which enables three-dimensional manipulation of single NW by a piezo translation stage. The PL of a single NW is collected by the same oil-immersion objective lens and passes through 750 nm shortpass filter focusing on either APD or liquid nitrogen cooled spectrometer via flip mirrors. A 550nm bandpass filter is placed before the APD to collect Er^{3+} $^4S_{3/2}$ state lifetime. The lifetime collection is described in the methods session. A color CCD is used to monitor the in-situ optical trapping process, which is shown in Fig. 5.2c. The left figure in Fig.5.2c shows the bright field image of a β-NaYF$_4$:20%Yb^{3+}/2%Er^{3+} NW under Brownian motion in water. The NW shows strong upconversion emission in an optical-trap under 975 nm excitation, which exhibits in the middle and right figures of Fig.5.2c. Forward-scattered laser radiation from optically-trapped single NW creates a dynamic interference pattern within the microscope's back-focal-plane that is detected with a high-speed silicon QPD. The time-dependent photovoltage signal from the QPD is then Fourier-transformed in order to compute the resulting power spectral density (PSD). A computer-controlled piezo-stage can be driven at a known frequency and amplitude to convert the units of the PSD from V^2/Hz to m^2/Hz in order to probe the diffusion coefficient of the trapped NW in solution.

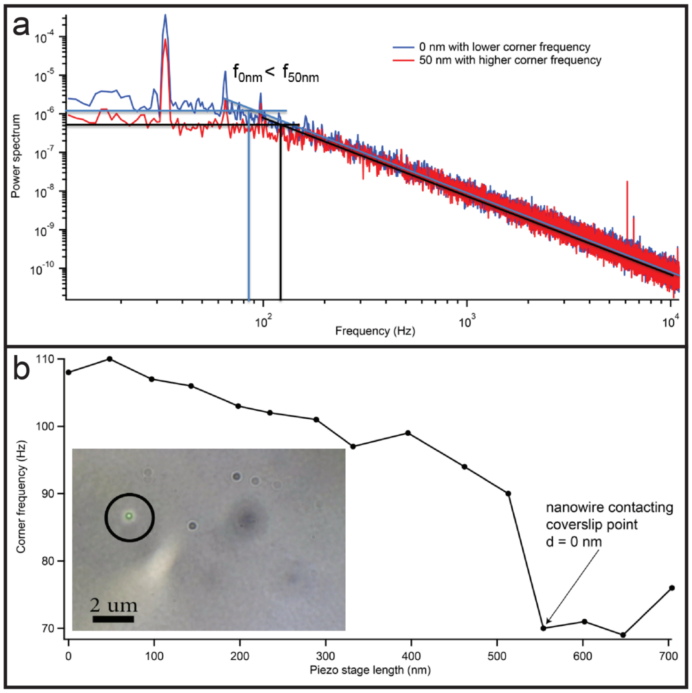

Figure 5.3: Measurement of optically trapped nanowire's distance from quartz surface substrate. (a) Power spectra comparison of nanowire at different distances from substrate. (b) Corner frequency comparison of nanowire at different distances from substrate.

As the distance of trapped NW close to the surface of quartz, the diffusion coefficient gradually decreases due to the wall-drag effect.[144] For the same NW under the same trapping condition, the diffusion coefficient of the NW can be represented by corner frequency obtained from the power spectrum, as shown in Fig.5.3a. The corner frequency changes as a function of trapping distance between the NW and the substrate, which is shown in Fig.5.3b. The drastic change indicates friction between NW and quartz surface when contact, which define d = 0 nm point. With changing the voltage of piezo-stage, the distance between trapped NW and quartz surface can increase up to 150 nm.

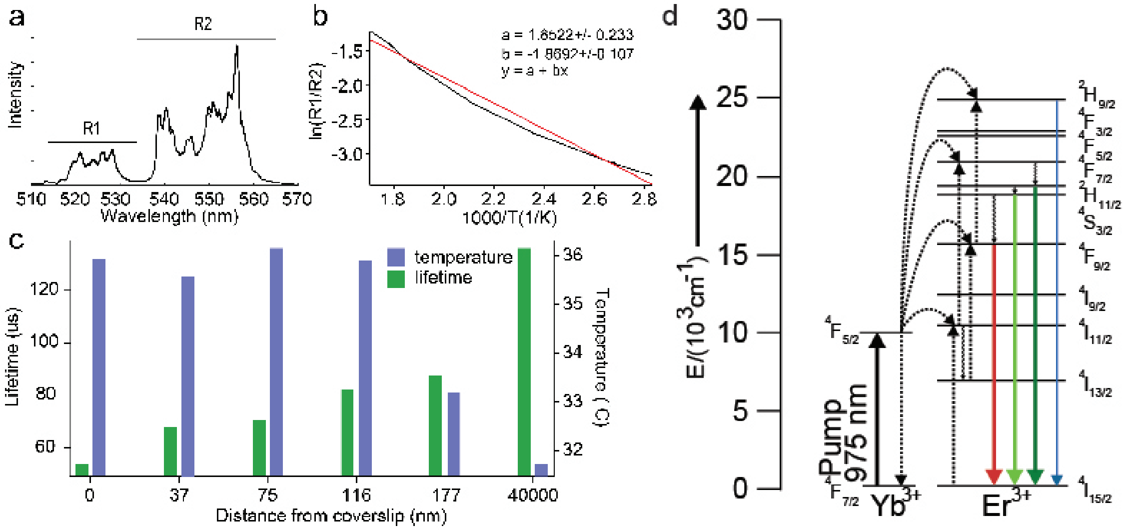

Figure 5.4: Raiometric thermometry of optically trapped β-NaYF$_4$:20%Yb^{3+}/2%Er^{3+} NW close to substrate. (a) Spectrum of β-NaYF$_4$:20%Yb^{3+}/2%Er^{3+} NW under 975 nm laser excitation. (b) Temperature calibration of β-NaYF$_4$:20%Yb^{3+}/2%Er^{3+} NW ratiometric therometry. (c) Temperature measurement of β-NaYF$_4$:20%Yb^{3+}/2%Er^{3+} NW at different distances from quartz substrate with ratiometric thermometry. (d) Yb^{3+}/Er^{3+} energy transfer diagram.

As the trapping distance between NW and substrate increases, the Er^{3+} $^4S_{3/2}$

state average lifetime increases from 69 μs to 139 μs, which is shown in fig.5.2b. The PL lifetime is the reverse of the sum of the radiative and nonradiative decay rate. Under the condition of same laser power and same trapped NW, the only variable is trapping distance. To diminish laser heating effect on substrate, quartz silica substrate is used to decrease 975 nm trapping laser absorption,[145] which shows a no obvious temperature change from ratiometric thermometry in Fig.5.4c.

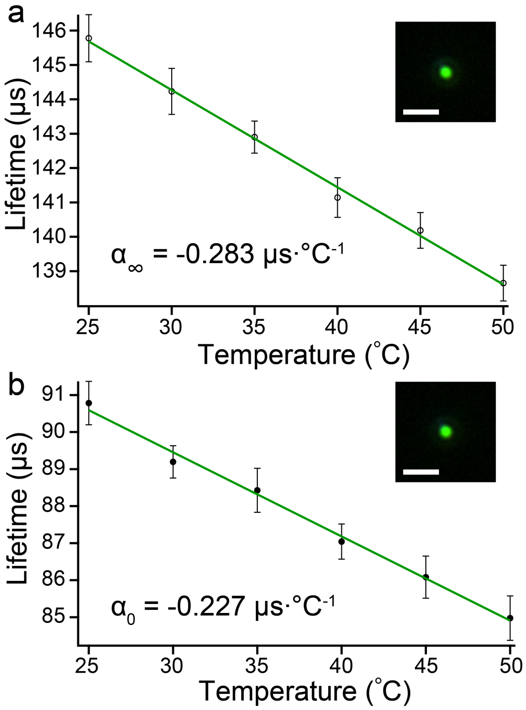

Figure 5.5: Temperature dependent Er^{3+} $^4S_{3/2}$ state temperature dependent lifetime study of single optically-trapped β-$NaYF_4$:20%Yb^{3+}/2%Er^{3+} NW in water. a) β-$NaYF_4$:20%Yb^{3+}/2%Er^{3+} NW trapped 40 μm away from quartz surface. Inset: photoluminescence from the trapped NW; scale = 2 μm. b) β-$NaYF_4$:20%Yb^{3+}/2%Er^{3+} NW trapped on quartz surface. Inset: photoluminescence from the trapped NW; scale = 2 μm.

The Er^{3+} ions have two close energy levels, $^4S_{3/2}$ and $^2H_{11/2}$, as shown in Fig.5.4d.

The energy difference between the two states are kT, which can be affected by surrounding temperature to cause phonon absorption or emission. The spectrum of the β-NaYF$_4$:20%Yb^{3+}/2%Er^{3+} emission shown in Fig.5.4a can be used for spectral thermometry. The R1 and R2 regions stand for ^{2}H$_{11/2}$ and ^{4}S$_{3/2}$ states. With calibrating the ratio of the integrated R1 over R2 versus the temperature, a temperature dependent trend can be achieved as shown in Fig.5.4b. Based on the ratiometric method, the optically trapped β-NaYF$_4$:20%Yb^{3+}/2%Er^{3+} NW shows no obvious temperature change.

Therefore, the temperature dependent nonradiative decay rate should be consistent at different trapping distances. The only explanation for this drastic lifetime change is the interference between NW and plane substrate.[132, 133] The radiative decay rate can be affected by the proximity of the emitting dipole to the interface. When dipole radiating near an plane interface, the rate is governed by the interference between the directly emitted waves and those reflected from the surface. Therefore the radiative decay rate is sensitive to the dipole polarization and distance relative to the interface, which results in PL lifetime changes. In our experiments, we use optical trapping to keep the same single NW's polarization with only tune the separation of NW and interface. The distribution in lifetimes at the same distance is attributed to the differences between individual NWs, including dopant concentration fluctuation, morphology, crystallinity, and others.[96, 93] To further investigate the substrate effect on single β-NaYF$_4$:20%Yb^{3+}/2%Er^{3+} NW's radiative decay, a lifetime thermal coefficient parameter α is applied to estimate relative radiative decay rate of single optically-trapped NW at different trapping distances. Fig.5.5a shows the temperature dependent trend of optically-trapped β-NaYF$_4$:20%Yb^{3+}/2%Er^{3+} 40um away from substrate, which we can consider as no interference effect from the substrate. The temperature of solution is controlled by perfusion chamber with a resolution of

0.1°C. With increasing the temperature of solution, the Er^{3+} $^4\mathrm{S}_{3/2}$ state lifetime of the single NW is decreasing due to the temperature dependent nonradiative decay rate. In this short temperature range, linear algebra is applied to fit this trend to achieve a 0.283 μs per degree C change, which provides a high R^2 value. Similar experiments have been conducted with the same β-$\mathrm{NaYF_4}$:20%Yb^{3+}/2%Er^{3+} NW at trapping distance is 0 nm from the substrate. The lifetime of the same NW shows a decreasing trend of 0.227 μs per degree C. The derivative of lifetime with respect to temperature is a defined as the lifetime thermal coefficient

$$\alpha = \frac{d\tau}{dT} = \frac{d(k_r + k_{nr})^{-1}}{dT} = -(k_r + k_{nr})^{-2}\frac{dk_{nr}}{dT} \tag{5.2}$$

where $\mathrm{k_r}$ is temperature independent radiative decay rate and $\mathrm{k_{nr}}$ is the temperature dependent nonradiative decay rate. The lifetime thermal coefficient ratio of the same optically-trapped NW at different distances is

$$\frac{\alpha_\infty}{\alpha_0} = (\frac{k_0 + k_{nr}}{k_\infty + k_{nr}})^2 \tag{5.3}$$

From the experimental data achieved in Fig.5.5, we achieve the values $\alpha_\infty = 0.283$ μs $°C$ and $\alpha_0 = 0.227$ μs s$°C$. Then we get the ratio $\frac{\alpha_\infty}{\alpha_0} = 1.147$. To get a boundary condition for minimum substrate effect on the radiative decay rate change of a single optically-trapped NW, we assume there is no nonradiative decay, in which $\mathrm{k_{nr}}$ is 0. Then we get

$$\frac{k_0}{k_\infty} = \sqrt{\frac{\alpha_\infty}{\alpha_0}} = \sqrt{\frac{0.283}{0.227}} = 1.117 \tag{5.4}$$

Since the nonradiative decay is not affected by the substrate LDOS, the minimum relative change of radiative decay rate is 1.117 times higher when the single NW getting close to the substrate. Since the nonradiative decay is a crucial factor, then its value is more than 0, which result in the relative change of radiative decay rate is higher than 1.117.

5.2.2 Lifetime thermometry application

In addition to quantify the radiative decay rate change, the temperature dependent Er^{3+} $^4S_{3/2}$ state lifetime of single β-$NaYF_4$:20%Yb^{3+}/2%Er^{3+} NW can also be used for non-contact fluorescence nanothermometry. Compared to conventional thermometry, fluorescence nanothermometry is able to make measurements with spatial resolution below the Rayleigh limit,[146, 99] which can be applied in various fields, such as microoptics, microelectronics, photonics, microfluidics, and others. The accurate precise temperature measurement of living cells enables investigation of temperature sensitive biological processes, such as gene expression, metabolic activity, cell division, and others.[147, 91, 148, 149] Nanothermometry of cancer cells that have higher temperature compared to normal tissues due to stronger metabolic activity can help understand their pathology and physiology, which leads to the improvement of diagnosis and therapeutic processes. A series of nanomaterials with their temperature sensitive optical properties including emission band shape, peak position, intensity or lifetimes have been utilized in nanothermometry, such as quantum dots, upconversion nanocrystals, carbon nanotubes, noble metal nanoparticles, fluorescence dyes, nanodiamond, nanogel, and other complex structure materials.[85, 28, 150, 151] As one of the most efficient upconversion materials, RE-doped-$NaYF_4$ nanoparticles exhibit strong visible emission under NIR excitation, which provides simultaneous functions of imaging, temperature sensing, heating, and thermaldynamic therapy with composition and surface modification. The Yb^{3+} and Er^{3+} codoped $NaYF_4$ nanocrystals have been extensively studied for nanothermometry in the range of biological temperature, due to the existence of thermally coupled $^2H_{11/2}$ and $^4S_{3/2}$ energy levels. For single particle thermometry, it usually requires an expensive spectrometer with complex post data processing to achieve temperature at nanoscale. We have developed a lifetime thermometry only requires a cheap and compact avalanche photodiode with live data extraction and process in LabVIEW, which can accurately and quickly probe the local temperature. In addition, optical trapping of nanoparticles with laser tweezers for nanothermometry can provide a precise temperature sensing at different locations in nanoscale.[152]. With the capability of 3D manipulation, optical tweezers can determination of the extension of the thermal gradient created in the surrounding of a plasmonic-mediated photo thermal treated HeLa cancer cell. [153]. It has been reported to measure the temperature of vapor nucleation in water.[154]. The NIR laser can be applied to study the heating effect on cell viability.[155] A precise calibration of temperature dependent lifetime change shown in fig.5.5 shows the capability of thermal mapping with single UCNP in the temperature range of biological processes. Additional substrate effect is also discussed earlier to improve the nanothermometry accuracy.

5.3 Ensemble nanoparticles thermometry

To further demonstrate the application of NW lifetime thermometry, we have embedded β-NaYF$_4$:20%Yb^{3+}/2%Er^{3+} NW in optical transparent PDMS composite, which is shown in the fig.5.6a. We use pulse 975 nm laser as temperature probing laser and 1064 nm for heating laser, since the 1064 nm is energy insufficient to pump Yb^{3+} transition, which will minimize the upconversion process. From the 3D reconstruction of confocal image of the composite, we can observe the uniformity and size distribution of NWs inside of the PDMS. We put the composite on a temperature control stage and calibrate its lifetime at different temperatures. It shows a thermal coefficient of lifetime -0.475 us°C. With co-aligning a 1064 nm laser on the 975 nm laser spot, we can increase the 1064 nm power to heat up composite and the temperature can be measured with 975 nm laser. With increasing the irradiance of 1064 nm laser to 495 kW/cm^2, the local temperature of PDMS composite can be tune from 300 K up to 336 K, which is in the temperature range of most biological processes. This dual laser beam system can be potentially applied in microfluidic system for non-contact local temperature control and probe.

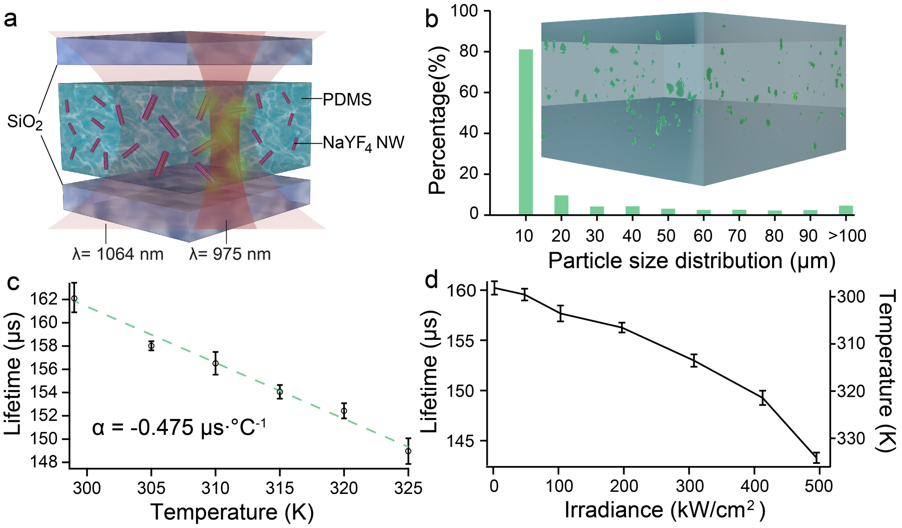

Figure 5.6: Er^{3+} $^4S_{3/2}$ state lifetime study of ensemble β-NaYF$_4$:20%Yb^{3+}/2%Er^{3+} NWs embedded in PDMS.a) Schematic of ensemble β-NaYF$_4$:20%Yb^{3+}/2%Er^{3+} embedded in PDMS structure. b) Temperature calibration of ensemble β-NaYF$_4$:20%Yb^{3+}/2%Er^{3+} NWs in vacuum. c) Temperature calibration of ensemble β-NaYF$_4$:20%Yb^{3+}/2%Er^{3+} NWs embedded in PDMS. d) Irradiance dependent study of ensemble β-NaYF$_4$:20%Yb^{3+}/2%Er^{3+} NWs embedded in PDMS.

β-NaYF$_4$:20%Yb^{3+}/2%Er^{3+} embedded in PDMS: 40 mg β-NaYF$_4$:20%Yb^{3+}/2%Er^{3+} were vigorously mixed with 50 mL SYLGARD 184 silicone elastomer base for 10 minutes and then the mixture were sonicated for 20 minutes. Take 5 mL in 10 mL tube and drop 0.5 mL SYLGARD 184 silicone elastomer curing agent to form final mixture. Then put the mixture in vacuum desiccator connected with house vacuum (-30 inHg) for 20 minutes to remove any gas bubble inside of the mixture. 0.5 mL of the clear mixture was drop casted on 1 inch No.1 thickness glass coverslip. 100 rpm was used to spin coat 2 minutes and then speed was increased to 500 rpm for another 2 minutes. The spin coated coverslip was then heat in an oven at 70 C for 12 hours to achieve the final β-NaYF$_4$:20%Yb^{3+}/2%Er^{3+} embedded PDMS.

To get time domain lifetime measurement, a Tectronix function generator is used to modulate Thorlab LDC 220 laser diode voltage controller. A 200 Hz and 1 ms width condition is applied to the laser diode. To get power stability of the laser during lifetime collection, the laser diode output signal and APD voltage signal are both collected through DAQ card to a computer and analyzed through a home-built LabVIEW code. The energy of each laser pulse is considered as the integration area of each pulse signal. The starting point for fitting lifetime decay curve is chosen as the 99.99% diminished laser energy. For collecting data only from Er^{3+} ^{4}S$_{3/2}$ state emission, a 550 ± 10 nm band-pass filter was used in place of 750 nm short-pass filter. The APD intensity signal has been fitted with double-exponential terms to get lifetime value.

5.4 Ratiometric thermometry

5.4.1 Ratiometric thermometry mechanism

RE^{3+} ions doped NaYF$_4$ nanocrystals have been used in bioimaging/labeling study for a long time due to its strong upconversion, narrow spectral transition and long lifetime.[156, 157, 158] The Er^{3+}, Yb^{3+} codoped NaYF$_4$ (Er^{3+}, Yb^{3+}:NaYF$_4$)nanocrystals can upconvert NIR light (920-1030 nm) to green and red light with two photon process via energy transfer from excited Yb^{3+} ions to fluorescent Er^{3+} ions.[17] The strong emission from a single optically trapped Er^{3+}, Yb^{3+}:NaYF$_4$ nanocrystals can be seen with unaided eyes. This unique property can be used in flat panel displays, light emitting diodes, security ink, biolabels and so on.[159, 160, 161, 162, 163] Recently, the emission band shape, peak position or lifetime have been found that can be affected by temperature significantly.[164, 165] Fig. 5.4d presents the two photon process affected by the temperature change. The Yb^{3+} ions excited by the NIR photon to $^2F_{5/2}$ state which is easily transferred to the resonant $^4I_{11/2}$ state of Er^{3+}. With two transfers of energy from Yb^{3+}, the Er^{3+} is excited from ground state $^4I_{15/2}$ to intermediate state $^4I_{11/2}$ and finally excited state $^4F_{7/2}$. The green emission from $^2H_{11/2}$ and $^4S_{3/2}$ excited states relates to two different emission bands of 515 nm-535 nm and 535 nm-570 nm. Since the two excited states are so close that have only few hundreds wavenumber difference. The intensity of the emission bands may be used to infer temperature changes through ratiometric thermometry by analysis of Boltzmann thermal populations,[165, 166] which is given by the equation:

$$\frac{I_2}{I_1} \propto exp(\frac{-(E_2 - E_1)}{k_b T}) \tag{5.5}$$

I_1 and I_2 are the integrated emission bands which relate to the transition between energy states E_2 and E_1 from the ground state. The temperature change of Er^{3+}, Yb^{3+}:$NaYF_4$ nanocrystals can lead to a thermalized Boltzmann distribution between the E_2 ($^2H_{11/2}$) and E_1 ($^4S_{3/2}$) manifolds of Er^{3+} and an intense green upconversion emission.

5.4.2 Ratiometric thermometry of carbon aerogel precursors

The Er^{3+}, Yb^{3+}:$NaYF_4$ nanocrystals were incorporated in the RF (resorcinol - formaldehyde) gels reaction system to investigate their thermometry ability. To study the temperature change of RF gel during formation with different electric field, Er^{3+}, Yb^{3+}:$NaYF_4$ nanocrystals were mixed with gel precursors including Na_2CO_3, resorcinol, formaldehyde and water. The mixture were put in a glass chamber with indium tin oxide (ITO) coated on the surface to apply alternative electric field. The chamber was placed in the laser tweezers setup with defocused 980 nm laser beam at 10 mW power output, which is shown in Fig.5.7a. The photoluminescence was collected with a Princeton liquid-nitrogen cooled Si detector.

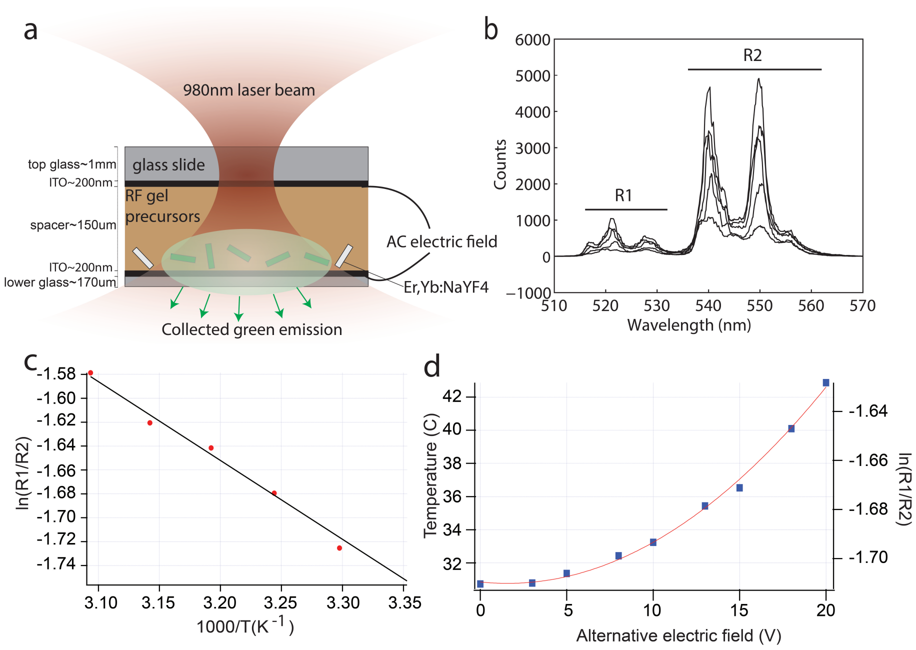

Figure 5.7: Ratiometric thermometry measurement of RF gel synthesis. (a) The experiment setup to measure dual emission photoluminescence from β-NaYF$_4$:20%Yb^{3+}/2%Er^{3+} nanocrystals in RF gel precursors. (b) Photoluminescence spectra showing the integration regions I_2 and I_1, representing emission from Er^{3+} energy states E_2 ($^2H_{11/2}$) and E_1 ($^4S_{3/2}$) to the ground state level ($^4I_{15/2}$), respectively. (c) Natural logarithm of the ratio I_2/I_1 showing a linear decrease with temperature change under 980 nm laser at 10 mW. (d) Temperature determined by the photoluminescence from β-NaYF$_4$:20%Yb^{3+}/2%Er^{3+} nanocrystals as a function of the applied voltage.

To calibrate the temperature of certain integrated bands ratio, a separate temperature controlled chamber was used to collect photoluminescence. At the same laser conditions, the temperature was precisely controlled from 30 ^{o}C to 50 ^{o}C, in which $\ln(R_1/R_2)$ corresponds to 1000/T with a linear trend shown in Fig.5.7c. With the linear temperature calibration, the temperature of RF precursors at different electric field was calculated. The observed quadratic dependence in Fig.5.7d is reasonable since the Joule dissipated energy various with the square of the applied voltage. Therefore we are able to study the gel formation as a result of external heating with temperature affected photoluminescence changes. Potential applications for Er^{3+}, Yb^{3+}:$NaYF_4$ nanocrystals include triggering and probing fundamental temperature-controlled biological processes due to the biocompatible property of $NaYF_4$ which has minimal interaction with cellular constituents to affect the temperature related processes.

Chapter 6

CLOSING REMARKS AND CONCLUSIONS

6.1 Conclusions

6.1.1 Summary of results

For the last five years in the Pauzauskie lab, I have been focusing on development and characterization of RE doped fluoride nanocrystals for laser cooling with a home-built laser tweezers setup. A low-cost, scalable, and environmentally friendly hydrothermal method has been investigated extensively to yield a final recipe for synthesizing high quality (low impurity and high crystallinity) fluoride nanocrystals in different phases, sizes, morphologies, and dopant concentrations. The hydrothermal growth mechanism has also been revealed in the thesis, which can help obtain complex structures of fluoride nanocrystals to meet requirements for future laser cooling or upconversion applications. The laser cooling occurs by Yb^{3+} ions inside the crystal absorbing laser photons and emitting a mean higher energy fluorescence to extract heat from the crystal lattice. Using a temperature extraction technique based on cold Brownian motion analysis, laser cooling of Yb^{3+} doped YLF nanocrystals in a condensed phase has been achieved for the first time. Furthermore, $NaYF_4$ nanocrystal, which has been predicted to be a good host structure for laser cooling, has also been proved for laser cooling in aqueous medium for the first time. The ability to optically generate local refrigeration fields around individual nanocrystals holds promises for applications in localized optoelectronic device cooling and physiological laser refrigeration. In addition to laser cooling, RE doped fluoride nanocrystals are demonstrated for nanoscale thermometry with spectroscopy methods, including lifetime of excited states, and spectra intensity ratios, which enables precise temperature control and sensing at the nanoscale.

6.1.2 Future directions

The laser cooling efficiency of nanocrystals can be further enhanced by several ways. First, one can minimize the surface quenching to improve the cooling efficiency. Multiphonon relaxation not only can happen through interaction with phonons in the host lattice, but also through interaction with molecular groups that attached on the surface of the host materials.[8] The energy migration between different active ions may transport excited state energy to the surface which causes heating of the surface. In order to minimize the energy transfer between internal active ions to surface active ions, the RE ion doped nanocrystal can be coated with non-dopant host materials. This will insulate the internal active ions transport energy outside. Second, one can change the laser cooling host material. Liu et al. have made an orthorhombic crystal structure upconversion nanocrystals KYb_2F_7, in which the RE ions are distributed in a tetrad clusters.[167] This special structure can effectively minimize the energy migration from tetrad clusters to defects and other clusters, which can make the Yb^{3+} concentration as high as 98%. Their research shows that the Er^{3+} doped KYb_2F_7 has 8 times higher intensity than previous reported. This super-enhanced upconversion may also bring significant laser cooling effects, which may freeze liquid water using only a near-infrared laser beam.

The laser cooling of solid-state materials is mostly focused on bulk crystals, which needs extreme synthetic conditions and expensive hardware to achieve high purity and minimal defects to increase the cooling efficiency. In contrast, hydrothermal synthesis can make large amounts of high purity and quality nanocrystal materials inexpensively and safely. Cooling a nanocrystal composite will be a major step forward for the future cryo-industry, as it can be easily shaped and fabricated. KBr and PDMS will be first tried as a composite matrix to suspend nanoparticles due to their low absorption and high transparency around the pumping laser wavelength of 1020 nm. Macroscopically, a thermal camera may be used to detect temperature of the composite illuminated with laser.[168] Microscopically, quantum dots may be used as a temperature sensor due to their luminescence variance at different temperature.[150, 165] The investigation of composite laser refrigeration proposed here could have far reaching impacts on a range of fields as well as unforeseen broader impacts in a range of other physical science applications.

BIBLIOGRAPHY

[1] Ri Epstein, Mi Buchwald, Bc Edwards, Tr Gosnell, and Ce Mungan. Observation of laser-induced fluorescent cooling of a solid. *Nature*, 377(6549):500–503, 1995.

[2] Seth D. Melgaard, Alexander R. Albrecht, Markus P. Hehlen, and Mansoor Sheik-Bahae. Solid-state optical refrigeration to sub-100 kelvin regime. *Sci. Rep.*, 6:20380, 2016.

[3] Paden B. Roder, Bennett E. Smith, Xuezhe Zhou, Matthew J. Crane, and Peter J. Pauzauskie. Laser refrigeration of hydrothermal nanocrystals in physiological media. *Proc. Natl. Acad. Sci.*, 112(49):15024–15029, 2015.

[4] Peter Pringsheim. Two observations about the difference between luminescence and thermal radiation. *Z. Phys.*, 57(11):739–746, 1929.

[5] L. Landau. On the thermodynamics of photoluminescence. *J. Phys.(Moscow)*, 10:503–506, 1946.

[6] Galina Nemova and Raman Kashyap. Laser cooling of solids. *Rep. Prog. Phys.*, 73(8):086501, 2010.

[7] Ikuji Tsujikawa and Tsuyoshi Murao. Possibility of optical cooling of ruby. *J. Phys. Soc. Jpn.*, 18(4):503–510, 1963.

[8] Richard I Epstein and Mansoor Sheik-Bahae. *Optical refrigeration science and applications of laser cooling of solids*. Wiley-VCH, 2009.

[9] Markus Hehlen. Crystal-field effects in fluoride crystals for optical refrigeration. *Proc of SPIE*, 7614, 2010.

[10] Xuezhe Zhou, Bennett E. Smith, Paden B. Roder, and Peter J. Pauzauskie. Laser refrigeration of ytterbium-doped sodiumyttriumfluoride nanowires. *Adv. Mater.*, 28(39):8658–8662, 2016.

[11] Onofrio M. Marag, Philip H. Jones, Pietro G. Gucciardi, Giovanni Volpe, and Andrea C. Ferrari. Optical trapping and manipulation of nanostructures. *Nat Nano*, 8(11):807–819, 2013.

[12] ML LEVIN and MA MILLer. Maxwell a treatise on electricity and magnetism. *Uspekhi Fizicheskikh Nauk*, 135(3):425–440, 1981.

[13] Arthur Ashkin. *Optical trapping and manipulation of neutral particles using lasers: a reprint volume with commentaries.* World Scientific, 2006.

[14] Chunhua Lu, Wenjuan Huang, Yaru Ni, and Zhongzi Xu. Hydrothermal synthesis and luminescence properties of octahedral $LiYbF_4$: Er^{3+} microcrystals. *Mater.Res.Bull*, 46(2):216–221, 2011.

[15] James J. De Yoreo, Pupa U. P. A. Gilbert, Nico A. J. M. Sommerdijk, R. Lee Penn, Stephen Whitelam, Derk Joester, Hengzhong Zhang, Jeffrey D. Rimer, Alexandra Navrotsky, Jillian F. Banfield, Adam F. Wallace, F. Marc Michel, Fiona C. Meldrum, Helmut Clfen, and Patricia M. Dove. Crystallization by particle attachment in synthetic, biogenic, and geologic environments. *Science*, 349(6247):aaa6760, 2015.

[16] Kezhi Zheng, Weiping Qin, Guofeng Wang, Guodong Wei, Daisheng Zhang, Lili Wang, Ryonginjin Kim, Ning Liu, Fuheng Ding, Xiaojie Xue, Tao Jiang, and Renyuan Yang. Upconversion luminescence properties of Yb^{3+}, Gd^{3+}, and Tm^{3+} co-doped $NaYF_4$ microcrystals synthesized by the hydrothermal method. *J. Nanosci. Nanonotechnol.*, 10(3):1920–1923, 2010.

[17] X. Liang, X. Wang, J. Zhuang, Q. Peng, and Y. Li. Synthesis of $NaYF_4$ nanocrystals with predictable phase and shape. *Adv. Funct. Mater.*, 17(15):2757–2765, 2007.

[18] Qiang Zhang and Bing Yan. Phase control of upconversion nanocrystals and new rare earth fluorides though a diffusion-controlled strategy in a hydrothermal system. *Chem. Comm.*, 47(20):5867–5869, 2011.

[19] Margarita Sanchez-Dominguez, Carolina Aubery, and Conxita Solans. New trends on the synthesis of inorganic nanoparticles using microemulsions as confined reaction media. 2012.

[20] Frances M. Ross. Opportunities and challenges in liquid cell electron microscopy. *Science*, 350(6267):aaa9886, 2015.

[21] A. V. Feshchenko, J. V. Koski, and J. P. Pekola. Experimental realization of a coulomb blockade refrigerator. *Phys. Rev. B*, 90(20):201407, 2014.

[22] Ihtesham Chowdhury, Ravi Prasher, Kelly Lofgreen, Gregory Chrysler, Sridhar Narasimhan, Ravi Mahajan, David Koester, Randall Alley, and Rama Venkatasubramanian. On-chip cooling by superlattice-based thin-film thermoelectrics. *Nat Nano*, 4(4):235–238, 2009.

[23] J. Flipse, F. L. Bakker, A. Slachter, F. K. Dejene, and B. J. van Wees. Direct observation of the spin-dependent peltier effect. *Nat Nano*, 7(3):166–168, 2012.

[24] W. Bogaerts, M. Fiers, and P. Dumon. Design challenges in silicon photonics. *IEEE Journal of Selected Topics in Quantum Electronics*, 20(4):1–8, 2014.

[25] C. Vicario, B. Monoszlai, Cs. Lombosi, A. Mareczko, A. Courjaud, J. A. Flp, and C. P. Hauri. Pump pulse width and temperature effects in lithium niobate for efficient THz generation. *Opt. Lett*, 38(24):5373, 2013.

[26] Elena M. Lucchetta, Ji Hwan Lee, Lydia A. Fu, Nipam H. Patel, and Rustem F. Ismagilov. Dynamics of drosophila embryonic patterning network perturbed in space and time using microfluidics. *Nature*, 434(7037):1134–1138, 2005.

[27] Jeong Hwan Lee, Hak-Seung Ryu, Kyung Sook Chung, David Pos, Soonkap Kim, Markus Schmid, and Ji Hoon Ahn. Regulation of temperature-responsive flowering by MADS-box transcription factor repressors. *Science*, 342(6158):628–632, 2013.

[28] G. Kucsko, P. C. Maurer, N. Y. Yao, M. Kubo, H. J. Noh, P. K. Lo, H. Park, and M. D. Lukin. Nanometre-scale thermometry in a living cell. *Nature*, 500(7460):54–58, 2013.

[29] Heng Huang, Savas Delikanli, Hao Zeng, Denise M. Ferkey, and Arnd Pralle. Remote control of ion channels and neurons through magnetic-field heating of nanoparticles. *Nat Nano*, 5(8):602–606, 2010.

[30] Jose H. Hodak, Julie L. Fiore, David J. Nesbitt, Christopher D. Downey, and Arthur Pardi. Docking kinetics and equilibrium of a GAAA tetraloop-receptor

motif probed by single-molecule FRET. *Proc. Natl. Acad. Sci.*, 102(30):10505–10510, 2005.

[31] Mitsuhiro Iwaki, Atsuko H. Iwane, Keigo Ikezaki, and Toshio Yanagida. Local heat activation of single myosins based on optical trapping of gold nanoparticles. *Nano Lett.*, 15(4):2456–2461, 2015.

[32] C. Loo, A. Lowery, N. J. Halas, J. West, and R. Drezek. Immunotargeted nanoshells for integrated cancer imaging and therapy. *Nano Lett.*, 5(4):709–711, 2005.

[33] S. M. Moghimi, A. C. Hunter, and J. C. Murray. Nanomedicine: current status and future prospects. *Faseb J.*, 19(3):311–330, 2005.

[34] L. Zhang, F. X. Gu, J. M. Chan, A. Z. Wang, R. S. Langer, and O. C. Farokhzad. Nanoparticles in medicine: Therapeutic applications and developments. *Clin. Pharmacol. Ther.*, 83(5):761–769, 2008.

[35] C. Loo, A. Lin, L. Hirsch, M. H. Lee, J. Barton, N. J. Halas, J. West, and R. Drezek. Nanoshell-enabled photonics-based imaging and therapy of cancer. *Technol. Cancer Res. Treat.*, 3(1):33–40, 2004.

[36] Dev K. Chatterjee and Zhang Yong. Upconverting nanoparticles as nanotransducers for photodynamic therapy in cancer cells. *Nanomedicine*, 3(1):73–82, 2008.

[37] Dejgj Dolmans, D. Fukumura, and R. K. Jain. Photodynamic therapy for cancer. *Nat. Rev. Cancer*, 3(5):380–387, 2003.

[38] T. J. Dougherty, C. J. Gomer, B. W. Henderson, G. Jori, D. Kessel, M. Korbelik, J. Moan, and Q. Peng. Photodynamic therapy. *J. Natl. Cancer Inst.*, 90(12):889–905, 1998.

[39] Feng Wang, Debapriya Banerjee, Yongsheng Liu, Xueyuan Chen, and Xiaogang Liu. Upconversion nanoparticles in biological labeling, imaging, and therapy. *Analyst*, 135(8):1839–1854, 2010.

[40] Fan Zhang, Qihui Shi, Yichi Zhang, Yifeng Shi, Kunlun Ding, Dongyuan Zhao, and Galen D. Stucky. Fluorescence upconversion microbarcodes for multiplexed biological detection: Nucleic acid encoding. *Adv. Mater*, 23(33):3775–3779, 2011.

[41] Przemek M. Krawczyk, Berina Eppink, Jeroen Essers, Jan Stap, Hans Rodermond, Hanny Odijk, Alex Zelensky, Chris van Bree, Lukas J. Stalpers, Marrije R. Buist, Thomas Soulli, Joost Rens, Hence J. M. Verhagen, Mark J. O'Connor, Nicolaas A. P. Franken, Timo L. M. ten Hagen, Roland Kanaar, and Jacob A. Aten. Mild hyperthermia inhibits homologous recombination, induces BRCA2 degradation, and sensitizes cancer cells to poly (ADP-ribose) polymerase-1 inhibition. *Proc. Natl. Acad. Sci.*, 108(24):9851–9856, 2011.

[42] D. M. Clarke, A. T. Robilotto, R. G. VanBuskirk, J. G. Baust, A. A. Gage, and J. M. Baust. Targeted induction of apoptosis via TRAIL and cryoablation: a novel strategy for the treatment of prostate cancer. *Prostate Cancer Prostatic Dis*, 10(2):175–184, 2007.

[43] Shinji Osada, Kazuhiro Yoshida, and Shigetoyo Saji. A novel strategy by cryoablation for advanced hepatoma. *Anticancer Res.*, 29(12):5203–5209, 2009.

[44] Shinji Osada, Hisashi Imai, Hiroyuki Tomita, Yasuharu Tokuyama, Naoki Okumura, Nobuhisa Matsuhashi, Fumio Sakashita, and Kenichi Nonaka. Serum cytokine levels in response to hepatic cryoablation. *J. Surg. Oncol.*, 95(6):491–498, 2007.

[45] Michael S. Sabel. Cryo-immunology: A review of the literature and proposed mechanisms for stimulatory versus suppressive immune responses. *Cryobiology*, 58(1):1–11, 2009.

[46] Majid Ebrahimzadeh. Mid-infrared ultrafast and continuous- wave optical parametric oscillators. In Dr Irina T. Sorokina and Dr Konstantin L. Vodopyanov, editors, *Solid-State Mid-Infrared Laser Sources*, number 89, pages 184–224. Springer Berlin Heidelberg, 2003.

[47] Denis V. Seletskiy, Seth D. Melgaard, Richard I. Epstein, Alberto Di Lieto, Mauro Tonelli, and Mansoor Sheik-Bahae. Precise determination of minimum achievable temperature for solid-state optical refrigeration. *J. Lumines.*, 133:5–9, 2013.

[48] Markus P. Hehlen, Mansoor Sheik-Bahae, Richard I. Epstein, Seth D. Melgaard, and Denis V. Seletskiy. Materials for optical cryocoolers. *J. Mater. Chem. C*, 1(45):7471–7478, 2013.

[49] Paden B. Roder, Sandeep Manandhar, Bennett E. Smith, Xuezhe Zhou, Vaithiyalingam S. Shutthanandan, and Peter J. Pauzauskie. Photothermal superheating of water with ion-implanted silicon nanowires. *Adv. Opt. Mater*, 3(10):1362–1367, 2015.

[50] Simon F. Toli-Nrrelykke, Erik Schffer, Jonathon Howard, Francesco S. Pavone, Frank Jlicher, and Henrik Flyvbjerg. Calibration of optical tweezers with positional detection in the back focal plane. *Rev. Sci. Instrum*, 77(10):103101, 2006.

[51] Kirstine Berg-Srensen and Henrik Flyvbjerg. Power spectrum analysis for optical tweezers. *Rev. Sci. Instrum*, 75(3):594–612, 2004.

[52] D. Chakraborty, M. V. Gnann, D. Rings, J. Glaser, F. Otto, F. Cichos, and K. Kroy. Generalised einstein relation for hot brownian motion. *EPL (Europhysics Letters)*, 96(6):60009, 2011.

[53] Daniel Rings, Markus Selmke, Frank Cichos, and Klaus Kroy. Theory of hot brownian motion. *Soft Matter*, 7(7):3441–3452, 2011.

[54] David G. Cahill, Wayne K. Ford, Kenneth E. Goodson, Gerald D. Mahan, Arun Majumdar, Humphrey J. Maris, Roberto Merlin, and Simon R. Phillpot. Nanoscale thermal transport. *J. Appl. Phys*, 93(2):793–818, 2003.

[55] Paul M. Hinderliter, Kevin R. Minard, Galya Orr, William B. Chrisler, Brian D. Thrall, Joel G. Pounds, and Justin G. Teeguarden. ISDD: A computational model of particle sedimentation, diffusion and target cell dosimetry for in vitro toxicity studies. *Part Fibre Toxicol*, 7(1):1–20, 2010.

[56] Erwin J. G. Peterman, Frederick Gittes, and Christoph F. Schmidt. Laser-induced heating in optical traps. *Biophys J*, 84(2):1308–1316, 2003.

[57] Dong Hee Son, Steven M. Hughes, Yadong Yin, and A. Paul Alivisatos. Cation exchange reactions in ionic nanocrystals. *Science*, 306(5698):1009–1012, 2004.

[58] Jothirmayanantham Pichaandi, John-Christopher Boyer, Kerry R. Delaney, and Frank C. J. M. van Veggel. Two-photon upconversion laser (scanning and wide-field) microscopy using Ln^{3+}-doped $NaYF_4$ upconverting nanocrystals: A critical evaluation of their performance and potential in bioimaging. *J. Phys. Chem. C*, 115(39):19054–19064, 2011.

[59] J. F. Suyver, J. Grimm, M. K. van Veen, D. Biner, K. W. Kramer, and H. U. Gudel. Upconversion spectroscopy and properties of $NaYF_4$ doped with Er^{3+}, Tm^{3+} and/or Yb^{3+}. *J. Lumin*, 117(1):1–12, 2006.

[60] Denis V. Seletskiy, Seth D. Melgaard, Stefano Bigotta, Alberto Di Lieto, Mauro Tonelli, and Mansoor Sheik-Bahae. Laser cooling of solids to cryogenic temperatures. *Nat Photon*, 4(3):161–164, 2010.

[61] X. L. Ruan and M. Kaviany. Enhanced laser cooling of rare-earth-ion-doped nanocrystalline powders. *Phys. Rev. B*, 73(15):155422, 2006.

[62] Flavio M. Mor, Andrzej Sienkiewicz, Laszlo Forro, and Sylvia Jeney. Upconversion particle as a local luminescent brownian probe: A photonic force microscopy study. *ACS Photonics*, 1(12):1251–1257, 2014.

[63] Paden B. Roder, Peter J. Pauzauskie, and E. James Davis. Nanowire heating by optical electromagnetic irradiation. *Langmuir*, 28(46):16177–16185, 2012.

[64] Sun-Kyung Kim, Kyung-Deok Song, Thomas J. Kempa, Robert W. Day, Charles M. Lieber, and Hong-Gyu Park. Design of nanowire optical cavities as efficient photon absorbers. *ACS Nano*, 8(4):3707–3714, 2014.

[65] Bong Je Park, A.-Ra Hong, Suntak Park, Ki-Uk Kyung, Kwangyeol Lee, and Ho Seong Jang. Flexible transparent displays based on core/shell upconversion nanophosphor-incorporated polymer waveguides. *Sci Rep*, 7:45659, 2017.

[66] Min Xu, Daqin Chen, Ping Huang, Zhongyi Wan, Yang Zhou, and Zhenguo Ji. A dual-functional upconversion core-shell nanostructure for white-light-emission and temperature sensing. *J. Mater. Chem. C*, 4(27):6516, 2016.

[67] Feng Wang and Xiaogang Liu. Upconversion multicolor fine-tuning: Visible to near-infrared emission from lanthanide-doped $NaYF_4$ nanoparticles. *J. Am. Chem. Soc*, 130(17):5642–5643, 2008.

[68] Priyam Singh, Praveen Kumar Shahi, Sunil Kumar Singh, Akhilesh Kumar Singh, Manish Kumar Singh, Rajiv Prakash, and Shyam Bahadur Rai. Lanthanide doped ultrafine hybrid nanostructures: multicolour luminescence, upconversion based energy transfer and luminescent solar collector applications. *Nanoscale*, 9(2):696–705, 2017.

[69] Xu Chen, Wen Xu, Hongwei Song, Cong Chen, Haiping Xia, Yongsheng Zhu, Donglei Zhou, Shaobo Cui, Qilin Dai, and Jiazhong Zhang. Highly efficient $LiYF_4$:Yb^{3+}, Er^{3+} upconversion single crystal under solar cell spectrum excitation and photovoltaic application. *ACS Appl. Mater. Interfaces*, 8(14):9071–9079, 2016.

[70] Xiaoyong Huang, Sanyang Han, Wei Huang, and Xiaogang Liu. Enhancing solar cell efficiency: the search for luminescent materials as spectral converters. *Chem. Soc. Rev.*, 42(1):173–201, 2013.

[71] Bryan M. van der Ende, Linda Aarts, and Andries Meijerink. Lanthanide ions as spectral converters for solar cells. *Phys. Chem. Chem. Phys.*, 11(47):11081–11095, 2009.

[72] Sanyang Han, Animesh Samanta, Xiaoji Xie, Ling Huang, Juanjuan Peng, Sung Jin Park, Daniel Boon Loong Teh, YonGdoo Choi, Young-Tae Chang, Angelo Homayoun All, Yanmei Yang, Bengang Xing, and Xiaogang Liu. Gold and hairpin DNA functionalization of upconversion nanocrystals for imaging and in vivo drug delivery. *Adv. Mater.*, 29(18):1700244, 2017.

[73] Yanan Huang, Qingbo Xiao, Huishan Hu, Kunchi Zhang, Yamin Feng, Fujin Li, Jian Wang, Xianguang Ding, Jiang Jiang, Yanfang Li, Liyi Shi, and Hongzhen Lin. 915 nm light-triggered photodynamic therapy and MR/CT dual-modal imaging of tumor based on the nonstoichiometric $Na_{0.52}YbF_{3.52}$:Er upconversion nanoprobes. *Small*, 12(31):4200–4210, 2016.

[74] Yong Il Park, Kang Taek Lee, Yung Doug Suh, and Taeghwan Hyeon. Upconverting nanoparticles: a versatile platform for wide-field two-photon microscopy and multi-modal in vivo imaging. *Chem. Soc. Rev.*, 44(6):1302–1317, 2015.

[75] Guanying Chen, Jie Shen, Tymish Y. Ohulchanskyy, Nayan J. Patel, Artem Kutikov, Zhipeng Li, Jie Song, Ravindra K. Pandey, Hans Agren, Paras N. Prasad, and Gang Han. (alpha-$NaYbF_4$:Tm^{3+})/CaF_2 core/shell nanoparticles with efficient near-infrared to near-infrared upconversion for high-contrast deep tissue bioimaging. *ACS Nano*, 6(9):8280–8287, 2012.

[76] Dev K. Chatteriee, Abdul J. Rufalhah, and Yong Zhang. Upconversion fluorescence imaging of cells and small animals using lanthanide doped nanocrystals. *Biomaterials*, 29(7):937–943, 2008.

[77] Zhuo Chen, Wei Zheng, Ping Huang, Datao Tu, Shanyong Zhou, MinGdong Huang, and Xueyuan Chen. Lanthanide-doped luminescent nano-bioprobes for the detection of tumor markers. *Nanoscale*, 7(10):4274–4290, 2015.

[78] Xiangzhao Ai, Linna Lyu, Yang Zhang, Yanxia Tang, Jing Mu, Fang Liu, Yixi Zhou, Zhenghong Zuo, Gang Liu, and Bengang Xing. Remote regulation of membrane channel activity by site-specific localization of lanthanide-doped upconversion nanocrystals. *Angew. Chem.-Int. Edit.*, 56(11):3031–3035, 2017.

[79] Christoph Drees, Athira Naduviledathu Raj, Rainer Kurre, Karin B. Busch, Markus Haase, and Jacob Piehler. Engineered upconversion nanoparticles for resolving protein interactions inside living cells. *Angew. Chem.-Int. Edit.*, 55(38):11668–11672, 2016.

[80] Guang-Rong Tan, Menghan Wang, Chin-Ying Hsu, Nanguang Chen, and Yong Zhang. Small upconverting fluorescent nanoparticles for biosensing and bioimaging. *Adv. Opt. Mater.*, 4(7):984–997, 2016.

[81] Ghulam Jalani, Rafik Naccache, Derek H. Rosenzweig, Lisbet Haglund, Fiorenzo Vetrone, and Marta Cerruti. Photocleavable hydrogel-coated upconverting nanoparticles: A multifunctional theranostic platform for NIR imaging and on-demand macromolecular delivery. *J. Am. Chem. Soc.*, 138(3):1078–1083, 2016.

[82] Ali Bagheri, Hamidreza Arandiyan, Cyrille Boyer, and May Lim. Lanthanide-doped upconversion nanoparticles: Emerging intelligent light-activated drug delivery systems. *Adv. Sci.*, 3(7):1500437, 2016.

[83] Dongmei Yang, Ping'an Ma, Zhiyou Hou, Ziyong Cheng, Chunxia Li, and Jun Lin. Current advances in lanthanide ion Ln^{3+}-based upconversion nanomaterials for drug delivery. *Chem. Soc. Rev*, 44(6):1416–1448, 2015.

[84] Guanying Chen, Hailong Qju, Paras N. Prasad, and Xiaoyuan Chen. Upconversion nanoparticles: Design, nanochemistry, and applications in theranostics. *Chem. Rev.*, 114(10):5161–5214, 2014.

[85] A. Assy, Hung-Ju Lin, M. Schoenauer-Sebag, P. Gredin, M. Mortier, L. Billot, Z. Chen, and L. Aigouy. Nanoscale thermometry with fluorescent yttrium-based Er/Yb-doped fluoride nanocrystals. *Sens. Actuator A-Phys.*, 250:71–77, 2016.

[86] Wei Yu, Wen Xu, Hongwei Song, and Shuang Zhang. Temperature-dependent upconversion luminescence and dynamics of $NaYF_4$:Yb^{3+}/Er^{3+} nanocrystals: influence of particle size and crystalline phase. *Dalton Trans.*, 43(16):6139–6147, 2014.

[87] Ol. A. Savchuk, J. J. Carvajal, M. C. Pujol, J. Massons, P. Haro-Gonzlez, O. Martnez, J. Jimnez, M. Aguil, and F. Daz. New strategies invonving upconverting nanoparticles for determining moderate temperatures by luminescence thermometry. *J. Lumin*, 169, Part B:711–716, 2016.

[88] Dan Wang, Lin Zhu, Jian-Feng Chen, and Liming Dai. Liquid marbles based on magnetic upconversion nanoparticles as magnetically and optically responsive miniature reactors for photocatalysis and photodynamic therapy. *Angew. Chem.-Int. Edit.*, 55(36):10795–10799, 2016.

[89] Feng Lu, Lin Yang, Yujie Ding, and Jun-Jie Zhu. Highly emissive Nd^{3+}-sensitized multilayered upconversion nanoparticles for efficient 795 nm operated photodynamic therapy. *Adv. Funct. Mater.*, 26(26):4778–4785, 2016.

[90] Yong Il Park, Hyung Min Kim, Jeong Hyun Kim, Kyung Chul Moon, Byeongjun Yoo, Kang Taek Lee, Nohyun Lee, Yoonseok Choi, Wooram Park, Daishun Ling, Kun Na, Woo Kyung Moon, Seung Hong Choi, Hong Seok Park, Soo-Young Yoon, Yung Doug Suh, Sung Ho Lee, and Taeghwan Hyeon. Theranostic probe based on lanthanide-doped nanoparticles for simultaneous in vivo dual-modal imaging and photodynamic therapy. *Adv. Mater*, 24(42):5755–5761, 2012.

[91] Yang Li, Jinglong Tang, Dong-Xu Pan, Ling-Dong Sun, Chunying Chen, Ying Liu, Ye-Fu Wang, Shuo Shi, and Chun-Hua Yan. A versatile imaging and therapeutic platform based on dual-band luminescent lanthanide nanoparticles toward tumor metastasis inhibition. *ACS Nano*, 10(2):2766–2773, 2016.

[92] Bo Zhou, Bingyang Shi, Dayong Jin, and Xiaogang Liu. Controlling upconversion nanocrystals for emerging applications. *Nat Nano*, 10(11):924–936, 2015.

[93] Wei Zheng, Ping Huang, Datao Tu, En Ma, Haomiao Zhu, and Xueyuan Chen. Lanthanide-doped upconversion nano-bioprobes: electronic structures, optical properties, and biodetection. *Chem. Soc. Rev.*, 44(6):1379–1415, 2015.

[94] A. Sia, P. Haro-Gonzlez, K. Horchani-Naifer, and M. Frid. La_2O_3: Tm, Yb, Er upconverting nano-oxides for sub-tissue lifetime thermal sensing. *Sensors and Actuators B: Chemical*, 234:541–548, 2016.

[95] Xingjun Zhu, Qianqian Su, Wei Feng, and Fuyou Li. Anti-stokes shift luminescent materials for bio-applications. *Chem. Soc. Rev.*, 46(4):1025–1039, 2017.

[96] Jing Zhou, Qian Liu, Wei Feng, Yun Sun, and Fuyou Li. Upconversion luminescent materials: Advances and applications. *Chem. Rev.*, 115(1):395–465, 2015.

[97] Yun Sun, Wei Feng, Pengyuan Yang, Chunhui Huang, and Fuyou Li. The biosafety of lanthanide upconversion nanomaterials. *Chem. Soc. Rev.*, 44(6):1509–1525, 2015.

[98] Zhanjun Gu, Liang Yan, Gan Tian, Shoujian Li, Zhifang Chai, and Yuliang Zhao. Recent advances in design and fabrication of upconversion nanoparticles and their safe theranostic applications. *Adv. Mater.*, 25(28):3758–3779, 2013.

[99] Yujia Liu, Yiqing Lu, Xusan Yang, Xianlin Zheng, Shihui Wen, Fan Wang, Xavier Vidal, Jiangbo Zhao, Deming Liu, Zhiguang Zhou, Chenshuo Ma, Jiajia Zhou, James A. Piper, Peng Xi, and Dayong Jin. Amplified stimulated emission in upconversion nanoparticles for super-resolution nanoscopy. *Nature*, 543(7644):229–233, 2017.

[100] Jiangbo Zhao, Zhenda Lu, Yadong Yin, Christopher McRae, James A. Piper, Judith M. Dawes, Dayong Jin, and Ewa M. Goldys. Upconversion luminescence with tunable lifetime in $NaYF_4$:Yb,Er nanocrystals: role of nanocrystal size. *Nanoscale*, 5(3):944–952, 2013.

[101] Yi Qin, Zhengwen Yang, Yong Yang, Dacheng Zhou, and Jianbei Qiu. Multicolor tunable luminescence in Yb^{3+}, Er^{3+} codoped $NaYF_4$ nanocrystals based on size-dependent. *Sci. Adv. Mater.*, 9(3):668–672, 2017.

[102] Xu Chen, Yongsheng Zhu, Donglei Zhou, Wen Xu, Jinyang Zhu, Gencai Pan, Ze Yin, He Wang, Shaobo Cui, and Hongwei Song. Size-dependent downconversion near-infrared emission of $NaYF_4$:Yb^{3+},Er^{3+} nanoparticles. *J. Mater. Chem. C*, 5(9):2451–2458, 2017.

[103] Mengyun Wang, Yun Tian, Fangyu Zhao, Renfu Li, Wenwu You, Zhenlan Fang, Xueyuan Chen, Wei Huang, and Qiang Ju. Alleviating the emitter concentration effect on upconversion nanoparticles via an inert shell. *J. Mater. Chem. C*, 5(6):1537–1543, 2017.

[104] Tianying Sun, Ronghua Ma, Xvsheng Qiao, Xianping Fan, and Feng Wang. Shielding upconversion by surface coating: A study of the emission enhancement factor. *Chem. Phys. Chem*, 17(5):766–770, 2016.

[105] Stefan Fischer, Noah D. Bronstein, Joseph K. Swabeck, Emory M. Chan, and A. Paul Alivisatos. Precise tuning of surface quenching for luminescence enhancement in core-shell lanthanide-doped nanocrystals. *Nano Lett.*, 16(11):7241–7247, 2016.

[106] Andreas Sedlmeier and Hans H. Gorris. Surface modification and characterization of photon-upconverting nanoparticles for bioanalytical applications. *Chem. Soc. Rev.*, 44(6):1526–1560, 2015.

[107] Feng Wang, Renren Deng, Juan Wang, Qingxiao Wang, Yu Han, Haomiao Zhu, Xueyuan Chen, and Xiaogang Liu. Tuning upconversion through energy migration in core-shell nanoparticles. *Nat. Mater*, 10(12):968–973, 2011.

[108] Michael D. Wisser, Stefan Fischer, Peter C. Maurer, Noah D. Bronstein, Steven Chu, A. Paul Alivisatos, Alberto Salleo, and Jennifer A. Dionne. Enhancing quantum yield via local symmetry distortion in lanthanide-based upconverting nanoparticles. *ACS Photonics*, 3(8):1523–1530, 2016.

[109] Feng Wang, Yu Han, Chin Seong Lim, Yunhao Lu, Juan Wang, Jun Xu, Hongyu Chen, Chun Zhang, Minghui Hong, and Xiaogang Liu. Simultaneous phase and size control of upconversion nanocrystals through lanthanide doping. *Nature*, 463(7284):1061–1065, 2010.

[110] Bin Shen, Shengming Cheng, Yuyang Gu, Danrui Ni, Yilin Gao, Qianqian Su, Wei Feng, and Fuyou Li. Revisiting the optimized doping ratio in core/shell nanostructured upconversion particles. *Nanoscale*, 9(5):1964–1971, 2017.

[111] Noah J. J. Johnson, Sha He, Shuo Diao, Emory M. Chan, Hongjie Dai, and Adah Almutairi. Direct evidence for coupled surface and concentration quenching dynamics in lanthanide-doped nanocrystals. *J. Am. Chem. Soc.*, 139(8):3275–3282, 2017.

[112] Dangli Gao, Xiangyu Zhang, Bo Chong, Guoqing Xiao, and Dongping Tian. Simultaneous spectra and dynamics processes tuning of a single upconversion microtube through Yb^{3+} doping concentration and excitation power. *Phys. Chem. Chem. Phys.*, 19(6):4288–4296, 2017.

[113] Wei Wei, Guanying Chen, Alexander Baev, Guang S. He, Wei Shao, Jossana Damasco, and Paras N. Prasad. Alleviating luminescence concentration quenching in upconversion nanoparticles through organic dye sensitization. *J. Am. Chem. Soc.*, 138(46):15130–15133, 2016.

[114] F. Vetrone, J. C. Boyer, J. A. Capobianco, A. Speghini, and M. Bettinelli. Significance of Yb^{3+} concentration on the upconversion mechanisms in codoped $Y_2O_3 : Er^{3+}$, Yb^{3+} nanocrystals. *J. Appl. Phys.*, 96(1):661–667, 2004.

[115] Zhang Liang, Enwei Sun, Ziyi Liu, Zhiguo Zhang, Jiangtao Zeng, Wei Ruan, Guorong Li, and Wenwu Cao. Electric field induced upconversion fluorescence enhancement and its mechanism in Er^{3+} doped 0.75Pb(Mg1/3Nb2/3)O3-0.25PbTiO3 transparent ceramic. *Appl. Phys. Lett.*, 109(13):132904, 2016.

[116] Xiao-Yu Geng, Ji Zhang, Xue-Yi Zhu, Bin Hu, Bin-Bin Zhang, Zhi-Peng Gao, Tao Zeng, Bin Yang, and Shan-Tao Zhang. Unusually enhanced upconversion photoluminescence in ferroelectric composite Er:0.94Bi(0.5)Na(0.5)TiO3-0.06BaTiO3/xZnO (x=0-0.4). *Appl. Phys. Lett.*, 109(12):122901, 2016.

[117] Jianhua Hao, Yang Zhang, and Xianhua Wei. Electric-induced enhancement and modulation of upconversion photoluminescence in epitaxial $BaTiO_3$:Yb/Er thin films. *Angew. Chem. Int. Ed.*, 50(30):6876–6880, 2011.

[118] Tung-Ching Huang and Wen-Feng Hsieh. er-yb codoped ferroelectrics for controlling visible upconversion emissions. *J Fluoresc*, 19(3):511–516, 2009.

[119] Ming-Kiu Tsang, Gongxun Bai, and Jianhua Hao. Stimuli responsive upconversion luminescence nanomaterials and films for various applications. *Chem. Soc. Rev.*, 44(6):1585–1607, 2015.

[120] Gongxun Bai, Ming-Kiu Tsang, and Jianhua Hao. Tuning the luminescence of phosphors: Beyond conventional chemical method. *Adv. Opt. Mater.*, 3(4):431–462, 2015.

[121] Yunxin Liu, Dingsheng Wang, Jianxin Shi, Qing Peng, and Yadong Li. Magnetic tuning of upconversion luminescence in lanthanide-doped bifunctional nanocrystals. *Angew. Chem. Int. Ed.*, 52(16):4366–4369, 2013.

[122] M. V. Yakushev, Y. Feofanov, R. W. Martin, R. D. Tomlinson, and A. V. Mudryi. Magneto-photoluminescence study of radiative recombination in $CuInSe_2$ single crystals. *J. Phys. Chem. Solids*, 64(9):2011–2016, 2003.

[123] A. Polimeni, S. T. Stoddart, M. Henini, L. Eaves, P. C. Main, K. Uchida, R. K. Hayden, and N. Miura. Magneto-photoluminescence and electroluminescence spectroscopy of self-assembled InGaAs quantum dots on high index planes. *Physica E: Low-dimensional Systems and Nanostructures*, 2(1):662–666, 1998.

[124] Michael D. Wisser, Maverick Chea, Yu Lin, Di M. Wu, Wendy L. Mao, Alberto Salleo, and Jennifer A. Dionne. Strain-induced modification of optical selection rules in lanthanide-based upconverting nanoparticles. *Nano Lett.*, 15(3):1891–1897, 2015.

[125] Shuhong Zheng, Weibo Chen, Dezhi Tan, Jiajia Zhou, Qiangbing Guo, Wei Jiang, Cheng Xu, Xiaofeng Liu, and Jianrong Qiu. Lanthanide-doped $NaGdF_4$ coreshell nanoparticles for non-contact self-referencing temperature sensors. *Nanoscale*, 6(11):5675–5679, 2014.

[126] C. Wuerth, M. Kaiser, S. Wilhelm, B. Grauel, T. Hirsch, and U. Resch-Genger. Excitation power dependent population pathways and absolute quantum yields of upconversion nanoparticles in different solvents. *Nanoscale*, 9(12):4283–4294, 2017.

[127] Mara Gonzlez-Bjar and Julia Prez-Prieto. Upconversion luminescent nanoparticles in physical sensing and in monitoring physical processes in biological samples. *Methods Appl. Fluoresc.*, 3(4):042002, 2015.

[128] Glauco S. Maciel, Marcio A. R. C. Alencar, Cid B. de Araujo, and Amitava Patra. Upconversion emission of $BaTiO_3$:Er^{3+} nanocrystals: Influence of temperature and surrounding medium. *J. Nanosci. Nanonotechnol.*, 10(3):2143–2148, 2010.

[129] Xiaomin Li, Fan Zhang, and Dongyuan Zhao. Lab on upconversion nanoparticles: optical properties and applications engineering via designed nanostructure. *Chem. Soc. Rev.*, 44(6):1346–1378, 2015.

[130] Xian Chen, Denfeng Peng, Qiang Ju, and Feng Wang. Photon upconversion in core-shell nanoparticles. *Chem. Soc. Rev.*, 44(6):1318–1330, 2015.

[131] Guofeng Wang, Qing Peng, and Yadong Li. Lanthanide-doped nanocrystals: Synthesis, optical-magnetic properties, and applications. *Accounts Chem. Res.*, 44(5):322–332, 2011.

[132] Faraz A. Inam, Michael D. W. Grogan, Mathew Rollings, Torsten Gaebel, Jana M. Say, Carlo Bradac, Tim A. Birks, William J. Wadsworth, Stefania Castelletto, James R. Rabeau, and Michael. J. Steel. Emission and nonradiative decay of nanodiamond NV centers in a low refractive index environment. *ACS Nano*, 7(5):3833–3843, 2013.

[133] F. A. Inam, T. Gaebel, C. Bradac, L. Stewart, M. J. Withford, J. M. Dawes, J. R. Rabeau, and M. J. Steel. Modification of spontaneous emission from nanodiamond colour centres on a structured surface. *New J. Phys.*, 13(7):073012, 2011.

[134] W. Lukosz and R. E. Kunz. Light emission by magnetic and electric dipoles close to a plane interface. i. total radiated power. *J. Opt. Soc. Am.*, 67(12):1607–1615, 1977.

[135] Andrea Pomozzi, Mi-Kyoung Park, and Maximilian Kreiter. Ensemble measurement of the orientation-dependent variations in chromophore lifetimes near a dielectric interface. *Phys. Rev. B*, 79(16):165435, 2009.

[136] R. M. Amos and W. L. Barnes. Modification of the spontaneous emission rate of Er^{3+} ions close to a thin metal mirror. *Phys. Rev. B*, 55(11):7249–7254, 1997.

[137] R. Valle, N. Tomczak, H. Gersen, E. M. H. P. van Dijk, M. F. Garca-Paraj, G. J. Vancso, and N. F. van Hulst. On the role of electromagnetic boundary conditions in single molecule fluorescence lifetime studies of dyes embedded in thin films. *Chem. Phys. Lett*, 348(3):161–167, 2001.

[138] J. J. Macklin, J. K. TrauTman, T. D. Harris, and L. E. Brus. Imaging and time-resolved spectroscopy of single molecules at an interface. *Science*, 272(5259):255–258, 1996.

[139] J. C. Ribierre, A. Ruseckas, P. E. Shaw, H. S. Barcena, P. L. Burn, and I. D. W. Samuel. Thickness dependence of the fluorescence lifetime in films of bisfluorene-cored dendrimers. *J. Phys. Chem. C*, 112(51):20463–20468, 2008.

[140] T. Tsutsui, C. Adachi, S. Saito, M. Watanabe, and M. Koishi. Effect of confined radiation-field on spontaneous-emission lifetime in vacuum-deposited fluorescent dye films. *Chem. Phys. Lett.*, 182(2):143–146, 1991.

[141] E. Snoeks, A. Lagendijk, and A. Polman. Measuring and modifying the spontaneous emission rate of erbium near an interface. *Phys. Rev. Lett.*, 74(13):2459–2462, 1995.

[142] G. S. Agarwal. Coherence in spontaneous emission in the presence of a dielectric. *Phys. Rev. Lett.*, 32(13):703–706, 1974.

[143] M. Kreiter, M. Prummer, B. Hecht, and U. P. Wild. Orientation dependence of fluorescence lifetimes near an interface. *The J. Chem. Phys*, 117(20):9430–9433, 2002.

[144] Erik Schaeffer, Simon F. Norrelykke, and Jonathon Howard. Surface forces and drag coefficients of microspheres near a plane surface measured with optical tweezers. *Langmuir*, 23(7):3654–3665, 2007.

[145] P. Haro-Gonzalez, B. del Rosal, L. M. Maestro, E. Martin Rodriguez, R. Naccache, J. A. Capobianco, K. Dholakia, J. Garcia Sole, and D. Jaque. Optical trapping of $NaYF_4$:Er^{3+},Yb^{3+} upconverting fluorescent nanoparticles. *Nanoscale*, 5(24):12192–12199, 2013.

[146] Yoshihiro Taguchi, Takumi Oka, Toshiharu Saiki, and Yuji Ngasaka. Development of near-field fluorescence lifetime thermometry. *Nanosc Microsc Therm.*, 13(2):77–87, 2009.

[147] Xiang Wu, Yuanwei Zhang, Kendra Takle, Osman Bilsel, Zhanjun Li, Hyungseok Lee, Zijiao Zhang, Dongsheng Li, Wei Fan, Chunying Duan, Emory M. Chan, Carlos Lois, Yang Xiang, and Gang Han. Dye-sensitized core/active shell upconversion nanoparticles for optogenetics and bioimaging applications. *ACS Nano*, 10(1):1060–1066, 2016.

[148] Ol A. Savchuk, P. Haro-Gonzlez, J. J. Carvajal, D. Jaque, J. Massons, M. Aguil, and F. Daz. Er:Yb:NaY_2F_5 up-converting nanoparticles for sub-tissue fluorescence lifetime thermal sensing. *Nanoscale*, 6(16):9727–9733, 2014.

[149] Kohki Okabe, Noriko Inada, Chie Gota, Yoshie Harada, Takashi Funatsu, and Seiichi Uchiyama. Intracellular temperature mapping with a fluorescent polymeric thermometer and fluorescence lifetime imaging microscopy. *Nat. Commun.*, 3:705, 2012.

[150] Fiorenzo Vetrone, Rafik Naccache, Alicia Zamarrn, Angeles Juarranz de la Fuente, Francisco Sanz-Rodrguez, Laura Martinez Maestro, Emma Martn Rodriguez, Daniel Jaque, Jos Garca Sol, and John A. Capobianco. Temperature sensing using fluorescent nanothermometers. *ACS Nano*, 4(6):3254–3258, 2010.

[151] Carlos D. S. Brites, Patricia P. Lima, Nuno J. O. Silva, Angel Millan, Vitor S. Amaral, Fernando Palacio, and Luis D. Carlos. Ratiometric highly sensitive luminescent nanothermometers working in the room temperature range. applications to heat propagation in nanofluids. *Nanoscale*, 5(16):7572–7580, 2013.

[152] Susil Baral, Samuel C. Johnson, Arwa A. Alaulamie, and Hugh H. Richardson. Nanothermometry using optically trapped erbium oxide nanoparticle. *Appl. Phys. A-Mater. Sci. Process.*, 122(4):340, 2016.

[153] Paloma Rodriguez-Sevilla, Yuhai Zhang, Patricia Haro-Gonzalez, Francisco Sanz-Rodriguez, Francisco Jaque, Jose Garca Sole, Xiaogang Liu, and Daniel Jaque. Thermal scanning at the cellular level by an optically trapped upconverting fluorescent particle. *Adv. Mater.*, 28(12):2421–2426, 2016.

[154] Arwa A. Alaulamie, Susil Baral, Samuel C. Johnson, and Hugh H. Richardson. Targeted nanoparticle thermometry: A method to measure local temperature at the nanoscale point where water vapor nucleation occurs. *Small*, 13(1):1601989, 2017.

[155] Franziska Wetzel, Susanne Roenicke, Karla Mueller, Markus Gyger, Daniel Rose, Mareike Zink, and Josef Kaes. Single cell viability and impact of heating by laser absorption. *Eur. Biophys. J. Biophys. Lett.*, 40(9):1109–1114, 2011.

[156] Fan Zhang, Ying Wan, Ting Yu, Fuqiang Zhang, Yifeng Shi, Songhai Xie, Yigang Li, Lei Xu, Bo Tu, and Dongyuan Zhao. Uniform nanostructured arrays of sodium rare-earth fluorides for highly efficient multicolor upconversion luminescence. *Angewandte Chemie*, 119(42):8122–8125, 2007.

[157] Datao Tu, Yongsheng Liu, Haomiao Zhu, Renfu Li, Liqin Liu, and Xueyuan Chen. Breakdown of crystallographic site symmetry in lanthanide-doped $NaYF_4$ crystals. *Angew. Chem.*, 125(4):1166–1171, 2013.

[158] Junwei Zhao, Yajuan Sun, Xianggui Kong, Lijin Tian, Yu Wang, Langping Tu, Jialong Zhao, and Hong Zhang. Controlled synthesis, formation mechanism, and great enhancement of red upconversion luminescence of $NaYF_4$:Yb^{3+},

Er^{3+} nanocrystals/submicroplates at low doping level. *J. Phys. Chem. B*, 112(49):15666–15672, 2008.

[159] Peter Lodahl, A. Floris van Driel, Ivan S. Nikolaev, Arie Irman, Karin Overgaag, Danil Vanmaekelbergh, and Willem L. Vos. Controlling the dynamics of spontaneous emission from quantum dots by photonic crystals. *Nature*, 430(7000):654–657, 2004.

[160] Pavel Cheben, Francisco del Monte, Dennis J. Worsfold, Dave J. Carlsson, Chander P. Grover, and John D. Mackenzie. A photorefractive organically modified silica glass with high optical gain. *Nature*, 408(6808):64–67, 2000.

[161] F. van De Rijke, H. Zijlmans, S. Li, T. Vail, A. K. Raap, R. S. Niedbala, and H. J. Tanke. Up-converting phosphor reporters for nucleic acid microarrays. *Nat. Biotechnol.*, 19(3):273–276, 2001.

[162] Garry Rumbles. Solid-state optics: A laser that turns down the heat. *Nature*, 409(6820):572–573, 2001.

[163] Mark Stockman. Light-emitting devices: From nano-optics to street lights. *Nat. Mater*, 3(7):423–424, 2004.

[164] Fiorenzo Vetrone, Rafik Naccache, Angeles Juarranz de la Fuente, Francisco Sanz-Rodriguez, Alfonso Blazquez-Castro, Emma Martin Rodriguez, Daniel Jaque, Jose Garcia Sole, and John A. Capobianco. Intracellular imaging of HeLa cells by non-functionalized $NaYF_4 : Er^{3+}, Yb^{3+}$ upconverting nanoparticles. *Nanoscale*, 2(4):495–498, 2010.

[165] Lorenz H. Fischer, Gregory S. Harms, and Otto S. Wolfbeis. Upconverting nanoparticles for nanoscale thermometry. *Angew. Chem.-Int. Edit.*, 50(20):4546–4551, 2011.

[166] Emily J. McLaurin, Liam R. Bradshaw, and Daniel R. Gamelin. Dual-emitting nanoscale temperature sensors. *Chem. Mater.*, 25(8):1283–1292, 2013.

[167] Juan Wang, Renren Deng, Mark A. MacDonald, Bolei Chen, Jikang Yuan, Feng Wang, Dongzhi Chi, Tzi Sum Andy Hor, Peng Zhang, Guokui Liu, Yu Han, and Xiaogang Liu. Enhancing multiphoton upconversion through energy clustering at sublattice level. *Nat. Mater*, 13(2):157–162, 2014.

[168] M. Moeller, V. Alchanatis, Y. Cohen, M. Meron, J. Tsipris, A. Naor, V. Ostrovsky, M. Sprintsin, and S. Cohen. Use of thermal and visible imagery for estimating crop water status of irrigated grapevine. *J. Exp. Bot.*, 58(4):827–838, 2007.

Appendix A

PUBLICATIONS

Journal Publications

1. Crane, M.J., Lim, M.B., **Zhou, X.**, Pauzauskie, P.J., Rapid synthesis of transition metal dichalcogenide aerogels for supercapacitor electrodes. (2017) (accepted by Nature Microsyst. Nanoeng)

2. Smith, B.E., **Zhou, X.**, Davis, E.J., Pauzauskie, P.J., Photothermal heating ofnanoribbons. (2017), Opt.Eng. 56, 011111-011111.

3. Wang, H., Mu, Q., Revia, R., Wang, K., **Zhou, X.**, Pauzauskie, P.J., Zhou, S., Zhang, M., Chitosan-Gated Magnetic-Responsive Nanocarrier for Dual-modal Optical Imaging, Switchable Drug Release and Synergistic Therapy. (2017), Adv. Healthc. Mater. 6(6), 1601080.

4. **Zhou, X.**, Roder, P.B, Smith, B.E., Pauzauskie, P.J., Laser Refrigeration of Ytterbium Doped Sodium Yttrium Fluoride Nanowires. (2016), Adv. Mater. 28(39), 8658-8662

5. Smith, B. E., **Zhou, X.**, Davis, E. J., Pauzauskie, P. J., Analytical predictions of the temperature profile within semiconductor nanostructures for solid-state laser refrigeration. (2016), SPIE. 9765, 97650G-97650G-6.

6. Smith, B.E., **Zhou, X.**, Roder, P.B., Abramson, E.H., Pauzauskie, P.J., Recovery of Si-IV nanowires from extreme pressure. (2016), J.Appl. Phys. 119(18), 185902.

7. Roder, P.B.*, Smith, B.E.*, **Zhou, X.***, Crane, M.J., Pauzauskie, P.J., Laser refrigeration of optically-trapped hydrothermal nanocrystals in physiological media.

(2015), Proc. Natl. Acad. Sci. 112, 15024-15029.*. Authors contribute equally.

8. Roder, P. B., Smith, B., **Zhou, X.**, Crane, M. J., Pauzauskie, P. J., Laser-refrigeration of rare-earth-doped nanocrystals in water. (2015), SPIE. 9380, 938007-938007-9.

9. Smith, B.E., Roder, P.B., **Zhou, X.**, Pauzauskie, P.J., Hot Brownian thermometry and cavity-enhanced harmonic generation with nonlinear optical nanowires. (2015), Chem. Phys. Lets. 639, 310-314. (invited feature article)

10. Smith, B. E., Roder, P. B., **Zhou, X.**, Pauzauskie, P. J., Nanoscale materials for hyperthermal theranostics. (2015), Nanoscale 7, 7115-7126.

11. Roder, P.B., Manandhar, S., Smith, B.E., **Zhou, X.**, Shutthanandan, V., Pauzauskie, P.J. Photothermal superheating of water with ion-implanted silicon nanowires. (2015), Adv. Opt. Mater. 3(10), 1362-1367.

12. Jin, H., Dong, J., Uchaker, E., Zhang, Q., **Zhou, X.**, Hou, S., Li, J. & Cao, G. Three dimensional architecture of carbon wrapped multilayer Na3V2O2(PO4)2F nanocubes embedded in graphene for improved sodium ion batteries. (2015), J Mater Chem A. 3, 17563-17568.

<u>Conference Publications</u>

1. **Zhou, X.**, Pauzauskie, P.J., Laser refrigeration of rare-earth doped sodium yttrium fluoride nanowires with anti-Stokes fluorescence, (2017) Opt. Life Sci. Congr.

2. **Zhou, X.**, Roder, P.B., Smith, B.E., Pauzauskie, P.J., Laser refrigeration of rare-earth doped sodium-yttrium-fluoride nanowires. (2017), Proc. SPIE 10121, Optical and Electronic Cooling of Solids II, 1012103